Investigation of an integrated optical detection system for fluorescence and absorption spectroscopy

Lidija Malic

Department of Electrical and Computer Engineering
McGill University
Montreal, Quebec, Canada
October 2005

A thesis submitted to the Faculty of Graduate Studies and Research in partial fulfillment of the requirements of the degree of Master of Engineering

Your file Votre référence
ISBN: 978-0-494-22655-1
Our file Notre référence
ISBN: 978-0-494-22655-1

Abstract

This thesis examines the design and fabrication of a miniaturized optical detection system for sensing in microchannels, based on integrated optical waveguide technology, which allows the implementation of both absorption and fluorescence measurement schemes and which can be potentially integrated into a Lab-on-a-chip system. An array of optical waveguides were fabricated in spin-on polymer technology on a silicon substrate and monolithically integrated with the microfluidic channel and V-groove fibre alignment scheme. Two different versions of the device were designed and fabricated at McGill microfabrication facility. The designs were adapted to achieve minimum optical losses under the imposed fabrication constraints. Total system losses with water filled microchannel were experimentally determined to be 10.45dB and 17.9dB for the two different devices. Both fluorescence and absorption detection capabilities of the fabricated devices were demonstrated using Alexa Fluor 633 dye, and the corresponding detection limits were found to be 10nM and 1μM respectively. Several areas of improvements in the device design and fabrication have been identified for future works towards better integration for Lab-on-a-chip system.

Sommaire

Cette thèse examine la conception et la fabrication d'un système optique miniaturisé d'analyse chimique basé sur la technologie des guides d'ondes planaires. Ce système permet la détection de l'absorption et de la fluorescence dans des capillaires et pourrait potentiellement être intégré dans un micro-laboratoire (Laboratoire-sur-puce). Il consiste en une rangée de guides d'ondes optiques fabriquée avec une technologie basée sur des polymères déposés sur un substrat de silicium et intégrée de façon monolithique avec un capillaire et avec un arrangement de carrelures en V permettant l'alignement passif des fibres optiques. Deux versions différentes du dispositif ont été conçues et fabriquées dans le laboratoire de micro-fabrication de McGill. Les systèmes ont été optimisés pour minimiser les pertes optiques tout en respectant les contraintes imposées par les outils de fabrication. Les pertes totales des systèmes avec le capillaire rempli d'eau ont été mesurées expérimentalement à 10.45dB pour le premier et à 17.9dB pour le deuxième système. Les capacités de détection de la fluorescence et d'absorption des dispositifs fabriqués ont été démontrées en utilisant le colorant Alexa Fluor 633, et les limites de détection se sont avérées de 10nM et 1mM, respectivement. Plusieurs possibilités d'amélioration dans la conception et dans la fabrication des dispositifs sont identifiées comme futurs travaux de recherche afin de perfectionner l'intégration des systèmes de micro-laboratoire.

Acknowledgements

First and foremost, I would like to thank my supervisor Associate Professor Andrew G. Kirk for his guidance and support throughout the entire project. Without his advices, teaching and supervision this project would have not been possible. Furthermore, I would like to acknowledge the members of the MEMS team: Xuyen Dai Hoa, Cristina Marinescu, Aju Jugessur and Colin Alleyne for their assistance provided over the past two years. Additional thanks go to the many members of the Photonic Systems Group who have helped me with this work and made these two years most enjoyable – professors Lawrence Chen and David Plant, and my fellow students – Mike, Po, Julien, Aref, Eric, Chris, Nicolas, Alan, Dominik, Véronique, Poulomi and many others. I would especially like to thank Michaël Ménard for his advices and expertise in many domains: AutoCAD, Code V, Adobe Illustrator, test setup assembly and French translation of the abstract. His help and his moral support was greatly needed and appreciated. Special thanks also go to Caroline Lei for her enthusiasm and help with several aspects of this project, including the modeling, the fabrication and the testing of the devices.

I would also like to acknowledge the cleanroom staff for always being ready to help and provide qualified information regarding processing issues at McGill Nanotools facility. I would especially like to thank Neal Lemaire for all his help in the yellow room, Donald Berry for his expertise on the RIE and MRC tools and Matthieu Nannini for his technical support. Special thanks also go to Vito Logiudice for his advices on the process flow and many fruitful discussions throughout this project.

Finally, I would like to thank my family and my friends for their continued support and encouragement over the years — especially my parents, Ivica and Slavica Malic, for their love, patience and endless supply of moral support. Thank you.

This work has been completed with financial support from the Postgraduate Scholarship Program of the National Sciences and Engineering Research Council (NSERC) of Canada.

TABLE OF CONTENTS

LIST OF FIGURES

LIST OF TABLES

LIST OF ABBREVIATIONS

LAC – Lab-on-a-chip

CCD – Charged coupled device

PMT – Photomultiplier tube

ICs – Integrated circuits

MEMS – Micro-electro-mechanical-systems

UV – Ultraviolet

SNR – Signal to noise ratio

LOD – Limit of detection

PDMS – Polydimethylsiloxane

μAPDs – Microavalanche photodiodes

LED – Light emitting diode

IOWs – Integrated optical waveguides

FHD – Fame hydrolysis deposition

PECVD – Plasma enhanced chemical vapor deposition

RIE – Reactive ion etching

CMP – Chemical mechanical polishing

MMF – Multimode optical fibre

PMMA – Polymethylmethacrylate

SMF – Single mode fibre

KOH – Potassium Hydroxide

ICP – Inductively coupled plasma

SMW – Single mode waveguide

MMW – Multimode waveguide

PS – Polystyrene

PC – Polycarbonate

DRIE – Deep reactive ion etch

EDP – Ethylene diamine pyrocatehcol

TMAHW – Tetramethyl Ammonium Hydroxide-Water

HF – Hydrofluoric

BPM – Beam Propagation Method

PR – Photoresist

SEM – Scanning electron microscope

DI water – De-ionized water

Tg – Glass transition temperature

PEB – Post exposure bake

PB – Pre exposure bake

PGMEA - Propylene glycol methyl ether acetate

1 Introduction

The miniaturization of analytical instruments utilizing micro and nano-fabrication technologies has been the object of an increasing interest in the past decade. The driving force for the current developments stems from the growing demand in the field of chemistry, biology, medicine and pharmacy, for low-cost analytical tools capable of rapid analysis in small sample volumes with a high level of automation [1,2]. Integrating all the necessary elements to perform specific measurements on one single chip, termed lab-on-chip (LAC), has the advantage of overall improved performance including increased sensitivity and signal to noise ratio, reduction in sample and reagents volume needs, reduction in analysis time, and increase in analysis throughput [3]. These microdevices, by achieving reduction in instrument size are portable, thus enabling highly complex laboratory testing to move from the central laboratory into nonlaboratory setting [3,4]. More importantly, they can be fabricated parallely in multiple copies, at low costs, using enabling MEMS technologies such as bulk or surface machining techniques. To expand functionality, efforts are given in integrating microfluidic channels with sensing, processing and actuation functions [4], thus increasing the effectiveness in applications pertaining to life sciences. Hence, lab-on-a-chip system incorporates three major subsets: the sensing system for analyte interrogation, the detectors for signal acquisition and the fluidic network for sampling and sample delivery (Figure 1.1).

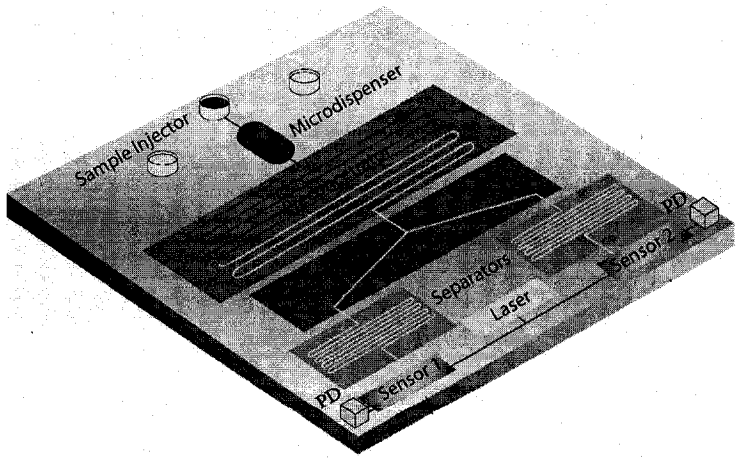

Figure 1.1 Lab-on-a-chip system consisting of fluidic network (sample injector, microdispenser, preconcetrator, multiplexer and separators), sensing system (sensor 1 and 2), detectors (PD)

Much of the effort in this field has been directed towards the design and fabrication of the sensor as a crucial component of the LAC system. Many different sensing strategies,

including microgravimetric, electrochemical and optical detection have been demonstrated [1,5]. Of these, optical detection methods are the most popular and present today's largest group of transducers [5]. They offer several advantages over other detection techniques and are discussed next.

1.1 Motivation and Objective: Optical biochemical sensing

Use of optical methods for sensing in the field of biochemistry and analytical or clinical chemistry offers multiple benefits including nondestructive operation mode, rapid signal generation and reading, capability for remote and multiple sensing, flexibility and ease of miniaturization [5,6]. Physical basis for the optical sensing lies in the information provided by the light's changes as it travels through the sensing medium, including changes in absorption, fluorescence, luminescence, scatter or refractive index [6]. This gave rise to several optical detection methods, such as total internal reflection spectroscopy, surface plasmon resonance, fluorescence or absorption spectroscopy and others. To gain more insight into different optical sensing techniques, the reader is referred to [7]. Among these, absorption and fluorescence detection are the most common tools in modern chemical and biochemical analysis. For achieving the highest possible detection sensitivity, optical detection based on fluorescence spectroscopy is currently considered state of the art [8]. However, this technique requires fluorescent labeling of the target analyte, and in this concept, absorption spectroscopy, as label-free sensing method is more advantageous. The objective of this thesis is to develop a microfluidic optical sensor design adaptable to the absorption and the fluorescence sensing schemes thus encompassing the benefits of both. Brief description of these two sensing methods is provided in the sections below.

1.1.2 Fluorescence

When molecules absorb photons at a given wavelength, they undergo either electronic or both electronic and vibrational excitation. The absorbed energy is normally dissipated in the form of heat; however, some molecules have the ability to re-emit part of this energy as longer wavelength photons, by means of fluorescence. Electronic and vibrational level

transitions involved in fluorescence phenomena can be understood with the aid of a Jablonski energy level diagram (Figure 1.2).

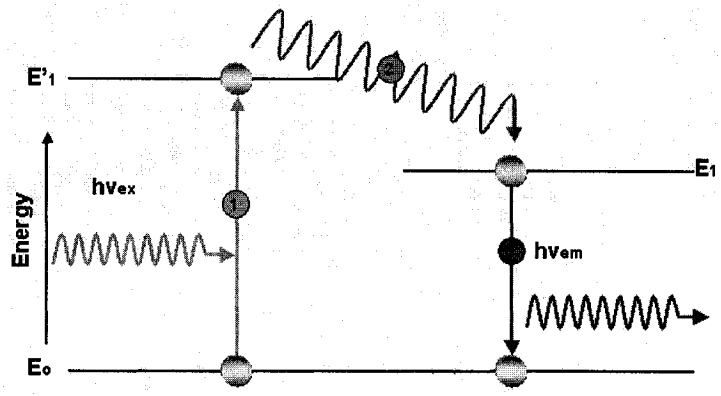

Figure 1.2 Jablonski diagram of fluorescence involved processes

From Figure 1.2, upon absorption of a photon (1), an electron gains enough energy to move from a ground state Eo towards an excited state E_1'. The electron will then lose part of its energy by vibrational relaxation (2) to reach the lowest energy level of the excited state E_1. This is followed by fluorescence (3), where the electron returns to the ground state Eo, by releasing the remaining energy in the form of a photon. Due to the loss of energy during the internal conversion in the excited state, the total energy of the emitted photon is lower than that of the excitation photon, resulting in the difference between the excitation and emission wavelengths, termed Stokes' shift. Through the use of suitable filters, this small shift in wavelength enables the detection of a small number of emitted photons in presence of large excess of excitation photons. Many chemical structures are known to be fluorescent. The spectral characteristics of the fluorescing base structures are sensitive to their chemical environment, thus allowing the fluorescent labeling of different analytes and their successive detection. Almost an infinite variety of chemicals can be characterized using analyte-specific fluorescence dyes: sodium, oxygen, calcium, chlorine, potassium, carbon dioxide, several halides, some toxic chemicals like sulfur dioxide, a number of gases and other chemical reagents [9]. Fluorescence can also be used to characterize proteins, membranes and DNA labeled by fluorescent probes. Moreover, use of fluorescence enables the determination of multiple analytes in parallel [8]. Fluorescence detection can thus be employed for biomedical applications such as reaction process monitoring, or hazardous agent detection. Other target applications

include point-of-care diagnostics, high-throughput screening, forensic tools, food quality control, and any environmental monitoring [10].

1.1.3 Absorption

Compared to fluorescence spectroscopy, absorption is a less sensitive detection method, however, it allows for the detection of target analyte without the use of labels. As mentioned in the previous section, when atoms absorb light within the ultraviolet or visible range, some of their electrons are excited to higher energy levels, corresponding to the excitation wavelength. Each compound has a different absorption spectrum, and can thus be identified [11]. The Beer-Lambert Law is used to measure sample concentration. As such, the intensity I of the light transmitted through a microfluidic channel containing a sample of concentration C, as a function of incident light intensity Io is given by the following expression,

$$I = Io\exp(-\varepsilon CL) \qquad (1)$$

where L is the channel length and ε is the extinction coefficient of a specific sample, and for a certain excitation wavelength. It is important to note, however, that the linearity of the Beer-Lambert law may be jeopardized by sample concentrations higher than 0.01M, induced natural fluorescence, scattering of light by particulates in the sample, and stray light [11]. The applications for absorption are the same as for fluorescence(section 1.1.2).

1.1.3 Fluorescence and absorption detection configuration

System configurations for the detection of fluorescence are often based on trans-illumination or epi-illumination configurations [8]. In trans-illumination configuration, the excitation light source, the sample and the detector are arranged in a straight line. The excitation light is focused onto the sample, and the emitted fluorescent light from the sample is filtered, collected and focused onto the detector, which may be a photodiode or a photomultiplier tube (PMT) without lateral resolution, or a laterally resolving detector like a charge-coupled device (CCD) camera. In an epi-illumination configuration, the detector is placed at 90° with respect to the light source, thus avoiding direct propagation of excitation light in direction towards the detector [8]. This configuration, though advantageous for fluorescence spectroscopy, cannot be used for absorption detection.

Hence, the system that is adaptable to both fluorescence and absorption spectroscopy needs to be arranged in trans-illumination configuration, as shown in Figure 1.3.

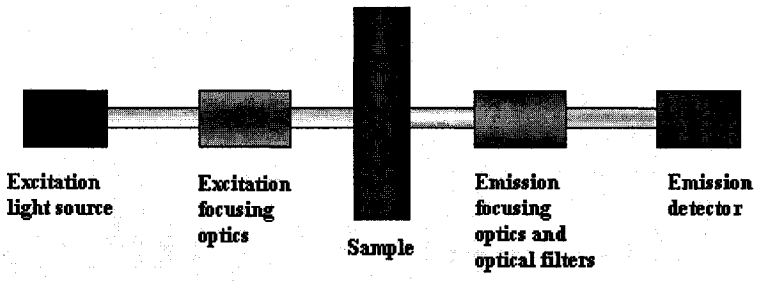

Figure 1.3 Trans-illumination configuration for fluorescence or absorption spectroscopy

Traditionally, bulk optic equipment such as lenses and microscope objectives have been employed in this configuration for detection of fluorescence from samples [8,10,12]. While advances in this technology continue to be made, a major drawback of employing macroscopic optics is associated with the high cost of equipment. Furthermore, the requirement for precise mechanical alignment limits their use to laboratory settings. As already mentioned, this has driven a massive research effort towards the development of an effective miniaturized sensor for fluorescence detection that would alleviate some of these problems. Researchers have demonstrated the use of micro-optics such as microlenses, optical fibers, and integrated waveguides to deliver and collect light between the microscopic samples and the macroscopic outside world [12]. These various systems will be discussed in more details in chapter 2, while the integrated planar waveguide design is briefly explained in the section below.

1.2 Brief system description

As outlined in the previous section, there are several drawbacks associated with the use of bulk optical equipment for fluorescence detection. Integrated optics based on planar waveguides can replace this macroscopic optics and, at the same time, be fabricated to match the microfluidic channels in both technology and size [10]. The objective of this thesis is to explore the integrated planar waveguide technology in the design and fabrication of a microfluidic optical sensor for absorption and/or fluorescence detection. The idea of monolithic integration of optical waveguides with the microfluidic channel is not novel and several research groups have proposed this configuration for biochemical sensing applications [2,10,13-17]. The simplified device layout is shown in Figure 1.4.

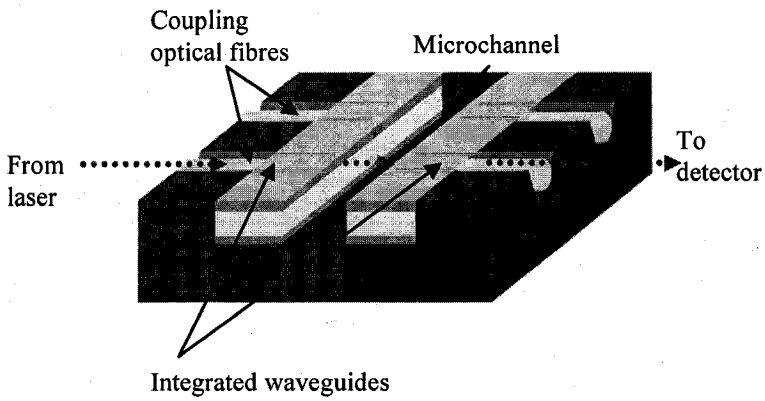

Figure 1.4 Simplified device layout

In Figure 1.4, the embedded waveguides confine the incoming excitement light towards a monolithically integrated microchannel. The emitted light from the microchannel is then transmitted through outgoing embedded waveguides toward the detector. Light coupling to and from the waveguides is usually done using optical fibre, as the waveguides use the same light guiding principle: total internal reflection. As such, light is captured inside the core of the waveguide if the core's refractive index is higher than that of the surrounding cladding's refractive index. The chief advantage of this configuration is the precise alignment of the waveguides to the channel during fabrication, resulting in a stable and robust optical system [15]. However, the main challenge related to this structure is the fabrication process itself. It requires careful selection of the materials and processing, since the properties needed for both photonics and microfluidics are not always compatible [17]. Another challenge for this configuration lies in the efficient coupling method between optical fibers and embedded waveguides, as this will directly affect the measurement accuracy. These challenges can be overcome only through careful design and material and process selection. This will be discussed in more details in Chapter 3.

1.3 Thesis Outline

The design and fabrication method of the microfluidic optical sensor for absorption and fluorescence spectroscopy, as presented in this thesis, is five-fold with each stage conveniently separated into a chapter. The first step, included in chapter 2, consists of a survey of existent optical sensors adaptable to fluorescence and absorption detection schemes, where design lessons and fabrication pointers are drawn from other researchers.

Furthermore, the review will offer a point of comparison for our biosensor design. Stemming from this study, specifications requirements for the optimal sensor design are determined and fabrication materials and processes are identified, as presented in chapter 3. Based on these requirements and selected fabrication materials, detailed design of each system component is presented in chapter 4, including an evaluation of the designed system performance. Next, the fabrication processes are carefully organized into a process flow and the recipe developed for each fabrication step is described in chapter 5. Following the recipe development, chapter 6 is dedicated to the integration of all the fabrication steps for the final device production. Challenges and issues encountered are highlighted as a motivation for the revised device design and fabrication, also included in this chapter. Assessment of performance of the two designs is presented in chapter 7, demonstrating their fluorescence and absorption detection capabilities. Finally, summary of accomplishments along with future works, including the existing device optimization and further system integration towards complete lab-on-a-chip system, are presented in chapter 8.

2 Literature review

"Much the way the invention of telescopes and radio powerfully extended what we can see and hear, the faint but informative presence of trace chemicals may one day be discerned by sensors on bands of small vehicles that cooperatively canvass the countryside [18]."

To take full advantage of the vast amount of information contained in chemical signatures of the world around us, conventional "extract and evaluate" procedures performed by analytical chemists in a laboratory setting need to be replaced by cheaper, faster and more sensitive methods. A promising solution lies in miniaturization and integration of chemical analysis systems onto a single chip. In words of Michael Sailor, an award-winning chemist and molecule explorer from University of California, "The vision is to produce something the size of a cell phone or smaller that can replace an analytical lab the size of a room [19]." Not only would this enable cost reduction and portability, but it would also increase the speed and reliability of chemical analysis [20,21]. Improvement in sensitivity and selectivity could also be achieved through use of multiple parallel separations channels, something only practical in microfabricated devices [18]. This has driven massive interest towards the exploration of a lab-on-a-chip idea, with applications as varied as the biosensing mechanisms employed. For instance, arrays of these biosensor chips could be mounted in airports or near factories to provide chemical inspection, while the same technology might be employed for immediate diagnostic at a patient's bedside [19]. However, the enormous progress made in biosensor technology would be impossible without the advent of micromachining processes. The next section overlooks historical development of micromachining processes that led to current advancements in MEMS and BioMEMS technology.

2.1 Brief history of micromachining and MEMS

While the lithographic process for defining and etching sub-mm features can be traced as early as 1500's, the actual miniaturization trend had started with the development of pure semiconductors, specifically silicon in 1940. As a consequence, invention of the silicon-based transistor in 1947 by W. Brittain and J. Bardeen indicated the beginning of the semiconductor circuit industry [20]. This trend continued with the first integrated circuits

(ICs) in 1958 by Texas Instruments, powered by the invention of the planar-batch fabrication process that allowed for the monolithic integration. Building on the available fabrication technology, the first batch-fabricated MEMS device, the resonant gate transistor, was produced in 1964 by Nathenson at Westinghouse [20]. In the following two decades, more refined microfabrication techniques were introduced, including bulk and surface micromachining, LIGA (acronym for the German words: lithography, electroforming and molding) and others. A variety of MEMS devices for mechanical applications have been developed and commercialized, including accelerometers and pressure sensors employed in the automotive industry. In late 1980's, the acronym MEMS was coined to designate the field of micro-electro-mechanical-systems. Since then MEMS devices have found their applications in almost any field, ranging from telecommunications to life sciences. Today, this term refers to all subminiaturized systems including Si-based mechanical devices, chemical and biological sensors and actuators, and miniature non-silicon structures [22]. More specific terms such as BioMEMS, optical MEMS or MOEMS, radio-frequency MEMS or RF-MEMS and many more have been and continue to be introduced as a testament to this ever-growing field. More recently, with the advancement of fabrication techniques enabling further miniaturization, the term NEMS (nano-electro-mechanical-systems) started to appear, and if this trend continues, very soon quantum limits on size reduction will be reached.

2.2 Survey of optical biosensor technology for fluorescence or absorption spectroscopy

Following this trend toward miniaturization of diagnostic systems as a whole, with the help of micromachining techniques, massive research has been conducted to deliver systems varying both in principle of operation and morphology. Detection modes in these systems range from ultraviolet (UV) absorbance, refractive index measurement, electrochemical detection or fluorescence detection, with the last being the preferred technique on biosensor chips due to its selectivity and high sensitivity. In view of optically based sensors adaptable to florescence or absorption spectroscopy, the main challenge is to design the proper optical detection scheme. That is, find the most effective way to guide light into the reactive channel, and collect it afterwards with the

least possible loss. For this to be done, micro-optical components used must be transparent in the near UV-Visible region. Furthermore, precise alignment of optical components is crucial to minimize optical losses and thus achieve high sensitivity with low power consumption. Both, design and fabrication methods / materials play an important role in the system performance and efficiency. Many design layouts have been proposed in combination with microfluidic channels. From all the propositions, at least three generally different ideas come in competition. One uses microlens arrays for principally fluorescence-based measurements, the second uses encapsulated optical fibers, and the third employs micromachined embedded waveguide structures to deliver and collect light between the microscopic samples and the macroscopic outside world. These three optical arrangements are described and compared in the following section of the chapter, underlying their unique advantages and shortfalls.

2.2.1 Detection system utilizing microlenses

Figure 2.1 describes the detection system based on microlens array developed by the researchers at the University of Neuchatel [23]. The device consists of an array of microlenses microfabricated on top of patterned aperture array, which enclose the microfluidic channels on both sides of the substrate.

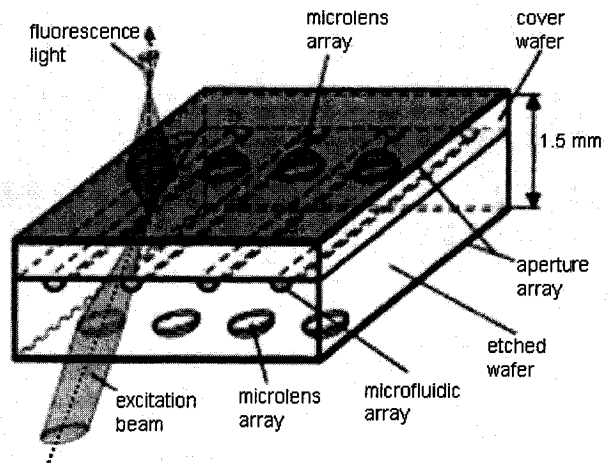

Figure 2.1 Optical sensor with microlens array [23]

The authors only report on successful fluorescence detection, however absorption detection scheme can also be realized with this configuration. Employing microlenses has an important advantage, as a large number of prealigned channels can be easily integrated on one chip, enabling simultaneous multi-analyte detection. The principle of device

operation is straightforward. The exciting light is confined to microfluidic channels by top surface array of micromachined focusing lenses. The entrance aperture layer defined underneath the lenses blocks the unfocused background laser beam, thus improving signal to noise ratio (SNR). On the other side of the chip, the light emitted from microchannels is in turn recaptured by another microlens-aperture array located under the microfluidic channel and focused to the detector.

The device is fabricated using two 100mm Pyrex wafers and five lithographic processes. The microfluidic network is wet-etched in the first wafer, followed by anodic bonding with the second wafer containing fluidic inlet ports. Next, manual sealing of fluidic ports is performed using adhesive tape to prevent channel clogging in the subsequent processing steps. Then chromium apertures are deposited and patterned on both sides of the wafer. Finally, microlens arrays are formed from 30μm thick layer of AZ4562 photoresist aligned with the apertures underneath. The reported limit of detection (LOD) of this configuration, using 633nm illumination from He-Ne laser and photomultiplier tube detection system for Cy5 fluorescent dye is 3.3nM.

Two main drawbacks of the described microlens configuration are related to the fairly complicated fabrication process flow, requiring five or six photolithographic steps, and the alignment challenge of the optical sources and detectors with the fabricated microlenses. Another shortfall is the need for manual sealing of the fluidic interconnects during fabrication, which would impede the mass-fabrication of the device. However, this configuration has an advantage over all the following detection designs; it does not require any source/detector plugging in, since it realizes the excitation and the emission light focusing without any external optical fibre coupling.

2.2.2 Detection system utilizing optical fibres

A second type of optical sensors for fluorescence or absorption detection in microchannels makes use of optical fibres encapsulated in the device layout during fabrication process. A typical device schematic is represented in Figure 2.2.

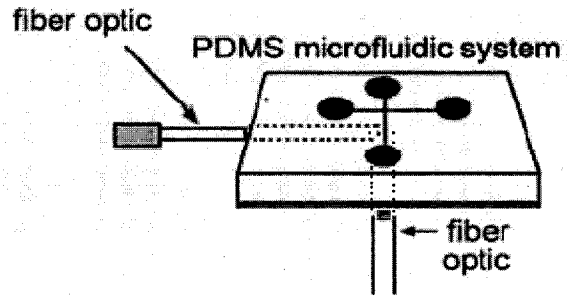

Figure 2.2 Optical sensor based on optical fibre detection arrangement [24-26]

The principle of operation for this arrangement is simple. Excitation light is confined in encapsulated optical fibre cable and delivered to the microchannel. The emitted light from the microchannel is captured by second optical fibre cable that is aligned to the channel excitation volume and arranged perpendicularly to the first cable for fluorescence detection or parallely for absorption detection.

The device is fabricated using replica molding in polydimethylsiloxane (PDMS). Use of PDMS as a structural material for microchannels is cost effective and enables easy encapsulation of optical fiber [24-26]. This is done by clamping an optical fibre near a channel on a master, pouring PDMS prepolymer over the master, and curing the PDMS that conforms to the surface of the fiber, thus alleviating a need for an index matching fluid.

Balberg and al. [24] have reported an impressive detection limit of 0.2fmol for fluorescein and 0.8fmol for rhodamine 590 dye using the above configuration with 488nm Ar-ion laser excitation and USB2000 spectrometer detection. It should be noted however that this detection limit was extracted from number of molecules present in the microchannel excitation volume of 10nL (fibre illuminated part of the channel) and not the actual dye concentration in the solution delivered to the channel. The main drawback of the presented detection scheme is the need for mechanical alignment of the collecting fibre optics with the illumination volume, as integration of this part of the system was not achieved.

Researchers from Harvard University [25,26], on the other hand, have gone a step further in system integration. While using the same principle to couple light to the microchannel, instead of using a second optical fibre to collect the emitted fluorescence, an integrated array of microavalanche photodiodes (μAPDs) encapsulated in PDMS and

bonded to the microchannel chip serves as a detector. A thin colored polymeric filter is sandwiched between the μAPD-array to filter out the background excitation light. The reported detection limit for this arrangement is 25nM for fluorescein using a blue light emitting diode (LED) as a light source.

One of the drawbacks of this system is poor control over the microchannel-fiber distance. Furthermore, direct encapsulation of fibers during PDMS cure causes deformation and bending of the channels which may hinder the sample flow.

2.2.3 Detection system based on integrated optical waveguides

Optical sensors based on integrated optical waveguides (IOWs) present the most popular fluorescence detection method and many different designs have been proposed in this configuration. They can be divided in two categories depending on the sensing technique employed: evanescent wave sensing and propagating mode sensing.

1. **Evanescent wave sensing**

Evanescent wave sensing, as the name suggests, relies upon evanescent interaction of light confined within the waveguide with the sensing layer that is immobilized on the waveguide surface [6,8,27,28] as depicted in Figure 2.3.

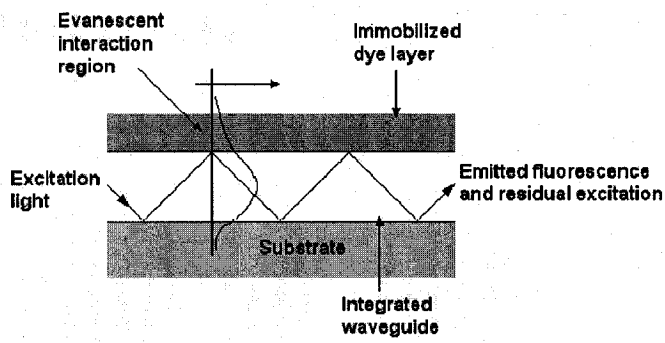

Figure 2.3 Schematic of an evanescent wave-based optical waveguide sensor [27]

When a light wave is guided through a medium of high refractive index (waveguide core) by total internal reflection, a small portion of the associated electromagnetic field will be transmitted through the surrounding lower-index medium (the sensing medium) as an evanescent wave with a penetration depth of a few hundred nm [27]. By measuring the changes in the light properties of this propagating evanescent wave, the changes occurring on the sensing surface can be determined. For this sensing scheme, light coupling into the waveguide can be achieved by front-face coupling using cylindrical lens

[6] or optical fibre [27], prism coupling or grating coupling [8], depending on the waveguide core thickness.

Nabok and al. [6] have reported a planar silicon nitride waveguide on silicon substrate with silicon dioxide superstrate onto which sensing window is etched and coated with analyte sensitive membrane for absorption detection. Light coupling from the 630nm laser diode into the 200nm thick core is achieved with focusing cylindrical lens, where the intensity of outcoming beam is recorded with an optical power meter. The reported detection limit of Imidacloprid pesticide is 10ppb (10μg/L). The main disadvantage of this arrangement is coupling using bulk free space optics. Since coupling into sub-micron core requires very precise alignment that can be achieved only by using precise mechanical alignment stages, the use of this detection system is limited to laboratory settings.

As a solution to this problem, Duveneck and al. [8] suggest use of monolithically integrated grating couplers. However this configuration suffers from high cost associated with the fabrication of nm-scale gratings.

A third approach to coupling has been presented by Burke and al. [28] who employed two refractive optic elements integrated with fabricated polystyrene waveguides for absorption-based sensing. The shortfall of this arrangement is the dependence of the refractive optics design on the sensing medium and on the concentration of the target analyte, making the detection system highly specific. Hence, in view of multianalyte sensing, design and fabrication of these structures would make this device highly impractical.

The most elegant solution to the coupling problem has been reported by researchers from University of Utah [27]. They fabricated the multimode waveguides and the self-aligning fibre coupling structures in SU8 using a single photolithographic step. Oxygen-sensitive dye is spin-coated on the waveguide surface and the chip is bonded with PDMS microfluidic network for fluorescence detection of oxygen. The reported detection limit of this system is 0.8mg/L.

One of the advantages of evanescent-waveguide biosensor that relies upon dye immobilization on the waveguide surface is that washing steps for removing unbound fluorescent molecules in a supplied sample is avoided, thus reducing the number of work

steps in a bioassay [8]. However, as the dye immobilization is often incorporated in the fabrication process of the device, this is also a disadvantage, as the multianalyte detection with the same chip becomes impossible. Another disadvantage of employing evanescent wave sensing lies in the fact that the intensity of light propagating in the form of an evanescent wave is less than 2% of the light confined in the waveguide core. It is thus susceptible to background noise due to scattering, which can easily drown the measured signal if the input light power is not considerably high.

2. Propagating mode sensing

Another detection configuration, briefly presented in chapter 1, employs IOWs for sample interrogation by propagating modes within the waveguide core. A cross-section and top view of the device layout presented in Figure 1.4 are shown below.

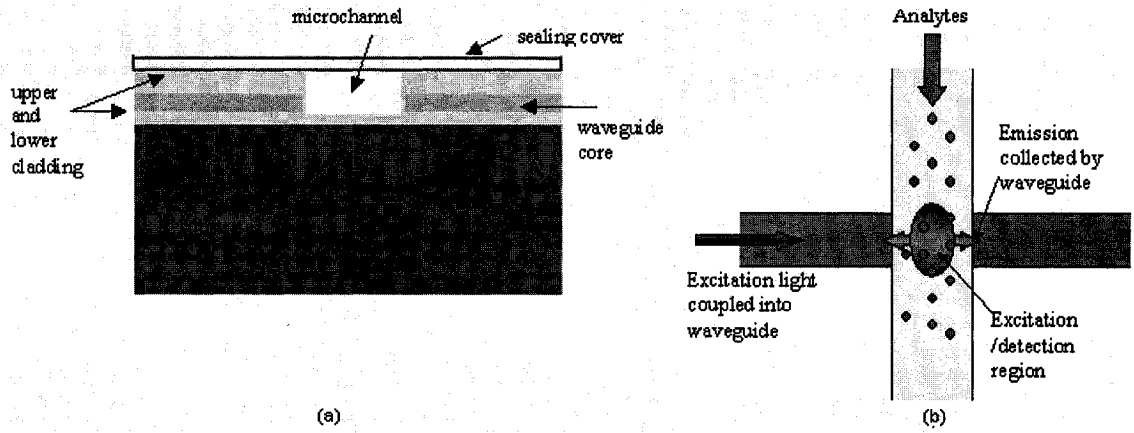

Figure 2.4 Microfluidic optical sensor based on IOWs: (a) Cross-sectional view; (b) Top view

The principle of operation of this configuration is the following. The incoming excitement light is confined by the waveguide core that has a higher refractive index than the surrounding cladding layers, and directed towards a monolithically integrated microchannel for interrogation of the sample. The emitted light from the microchannel is then transmitted through the outgoing embedded waveguides towards the detector. Light coupling to and from the waveguides is usually done using optical fibre, however free space optic coupling has also been reported [16].

Monolithic integration of the optical waveguides with the microfluidic channel allows for precise alignment of the optical components, which is one of the advantages of this arrangement over other configurations employed. The challenge however lies in material selection for fabrication of both waveguides and microfluidic channels, as these

can severely limit the device design and performance in certain applications. The two waveguide-fabrication techniques that are applicable for monolithic integration with microfluidic structures for fluorescence or absorption spectroscopy are silica on silicon and polymer-based waveguide technology.

A. Silica on silicon waveguide technology

Silica on silicon waveguide technology employs either flame hydrolysis deposition (FHD) [16,29,30] or plasma enhanced chemical vapor deposition (PECVD) [10,13,15] to deposit either pure or doped silica glass onto a silicon wafer. Reactive ion etching (RIE) is used to define guiding structures and microfluidic channels in deposited layers. Chemical mechanical polishing (CMP) is needed to planarize the structures prior to bonding.

Ruano and al. [16,29,30] have used a combination of FHD and RIE to define silica waveguides and microfluidic channels with two photolithographic steps. The design consisted of 7-9μm thick waveguide cores positioned perpendicularly to a 40μm deep reaction chamber with tapered profile in order to improve collection/dispersion efficiency at the chamber interface. Fluorescence detection was demonstrated using both, but-coupled multimode optical fibre (MMF) [29] and coupling using free space optics [16,30] to deliver light to and from the fabricated waveguides. The reported detection limits are 30μM and 20pM respectively for Cy5 fluorescent dye using 633nm He-Ne excitation and silicon photodetectors. The main drawback of utilizing FHD silica deposition is that very high temperature of the process (1300°C) might limit the chip integration with electronic parts needed for a complete LAC system [31].

On the other hand, PECVD can be carried out at much lower temperatures (<400°C) [31] which might alleviate some of the problems associated with FHD. Researches from Technical University of Denmark have demonstrated PECVD silica waveguides for both fluorescence [10,15] and absorption detection [13]. Their waveguide design is particularly interesting since it alleviates the need for surface planarization [15]. During mask design, instead of defining only doped silica core layers to be left on the wafer, they define two etch trenches on each side of the waveguide, with the remaining film around the etched trenches serving as the bonding pad. This then allows for hermetic

sealing of the device using anodic bonding, without any intermediate CMP step. They demonstrated the use of 6μm thick nitrogen doped and 4μm thick germanium doped waveguides for absorption [13] and fluorescence [10,15] measurements respectively. Coupling to and from the waveguides is achieved by pigtailing and permanently gluing MMFs to waveguide endfaces. The lowest detection concentration for absorption detection of propanol using deuterium halogen lamp excitation and optical spectrum analyzer was found to be 13μM. For fluorescence detection, excitation from Ar-ion laser was employed to detect 250pM of fluorescein and excitation from red-laser diode was used to detect 100nM of Bodipy dye.

Although use of silica for waveguide and microchannel fabrication has advantages such as high optical transparency in the region of interest, mechanical, thermal and chemical stability, relatively complex and costly fabrication processes limiting the waveguide thickness to few μm have led to employment of less expensive polymer materials with similar optical properties, that can be easily deposited and patterned to the required thickness. These are discussed next.

B. Polymer waveguide technology

Optical waveguides of polymeric materials integrated with microfluidic channels can be made by simple manufacturing procedures including spin coating and photolithography, or replica-molding. Several research groups have presented waveguides made of PDMS, SU8 or polymethylmethacrylate (PMMA).

For instance, Lien and al. [32] have used replica-molding to produce two perpendicular PDMS microchannels, one for fluidic component and the second for waveguides. This was followed by surface treatment of the fluidic channel which would enable insertion of higher refractive index PDMS into perpendicular waveguide channels without causing clogging of the fluidic channel. The higher refractive index PDMS would then distribute evenly to form the waveguide core due to capillary forces after which UV curing was carried out to harden the material. The reported optical loss for the device interfaced with MMFs was found to be as low as 2.71dB for air-filled channel. Potential for fluorescence detection was demonstrated, but the lowest detection limit was not assessed.

A similar approach to waveguide fabrication has been reported by Lin and al [33]. They used photolithography and wet etch to define circular microchannels in two soda-lime glass substrates that were subsequently bonded to seal the structures. As before, capillary forces were used to fill the waveguide channels with thin spin-on-glass (SOG) that served as planarization layer needed to smooth the surface of the etched channels. Next, both MMFs and single mode fibres (SMFs) were inserted into the waveguide channels, followed by channel filling with waveguide core material, SU-8, using vacuum suction to improve filling efficiency. Fluorescence detection has been carried out using 633nm He-Ne laser excitation and PMT optical detection scheme. Results showed that the detection limits for Rhodamine B dye are 100nM using MMFs and 1μM using SMFs.

Although the fabrication of the above devices is very simple, the need for manual filling of the waveguide channels is not practical for batch fabrication.

Two other research groups, one from Georgetown University [17] and another from Technical University of Denmark [34,35] have developed microfluidic devices with integrated optical waveguides in SU8 resist for fluorescence and absorption detection respectively.

The first design by Leeds and al. [17] consisted of a glass slide onto which 100μm thick SU-8 waveguides were placed on each end of 1cm long microfluidic channel defined by bonding structures also in SU-8 material. This arrangement required only a single photolithographic step to define the structures that were sealed with a glass lid using an intermediate adhesive SU-8 layer strategically placed only over regions that would cover the microfluidic channel. This preserved light confinement in waveguide structures with air side cladding and glass top/bottom cladding. The reported fluorescence detection limit of Rhodamine B dye using 543nm He-Ne laser prism coupled to the excitation waveguide and imaged from above using a CCD camera was 64μM. To improve sensitivity, a second device was fabricated with SU-8 waveguides positioned perpendicularly with each other, with detection waveguide tapering to span the entire length of the fluidic channel. This required two selective mettalization steps, both inside the microfluidic channel and along the tapered waveguide to increase the light guiding efficiency. Performance assessment was not performed for this second device, however an increase in signal strength is estimated to be by a factor in the order of 10^5. Although

an improvement in sensitivity is expected with the second design, a major drawback is that the required mettalization layers inside the microchannel might not be biocompatible with the analyte. Furthermore, as detection waveguide spans the entire length of the channel, fabrication of an array of waveguides for multianalyte detection is impossible with the current design.

Mogensen and al. [34,35] have also fabricated an all SU-8 device for absorption detection. The same fabrication method as above was used that resulted in air side cladding and glass top and bottom cladding layers. However, an improvement in device design was made, where an array of 90μm thick waveguides was placed perpendicular to the channel along with tapered fibre-coupling grooves to enable self-alignment of optical fibres to the fabricated waveguides. Three different bonding schemes were investigated, where plasma-activated PDMS bonding resulted in lowest optical transmission losses. Absorption detection limit as measured with a spectrometer of bromothylmol blue dye excited with 633nm He-Ne laser was found to be 15μM. An important advantage of this design is the inclusion of fibre coupling structures during device fabrication which reduces time and cost associated with alignment and enables device portability. Another advantage is fast and inexpensive fabrication, since only a single photolithographic step is employed. A shortfall associated with optical performance of the device is that large geometrical mismatch between the optical fibres (50μm diameter) and the fabricated waveguides (90μm thick, 30μm wide) results in increased coupling losses. Furthermore, as side claddings consist of air, the device is also prone to large scattering losses.

Another interesting configuration utilizing polymer waveguides integrated with microfluidic channels and fibre-coupling grooves has been proposed by researchers at Louisiana Tech University [14]. The device is said to be fabricated on silicon wafer onto which V-grooves are etched perpendicularly to the etched square trench using Potassium Hydroxide (KOH) wet etch and inductively coupled plasma (ICP) etch respectively. Next the lower cladding consisting of epoxy resin is deposited and patterned in the etched trench, onto which 50μm thick PMMA core is spin-coated and ICP etched using thermal evaporated Al as hard mask. Finally the upper cladding is deposited and patterned followed by microchannel formation. The total number of photolithography steps is six. Although the authors have not reported the actual device fabrication and testing, the

advantages of this configuration is the inclusion of fibre self-aligning V-grooves which facilitate fibre-to-waveguide coupling. Furthermore, since V-grooves are defined in silicon substrate, as opposed the core layer described above [34,35], the coupling efficiency between the waveguides and the optical fibre can be increased by tailoring the waveguide thickness to match optimum coupling conditions. A disadvantage however, from a fabrication point of view is the requirement for six photolithographic steps which increases device complexity and the associated fabrication cost. Furthermore, the selection of PMMA for a core layer might pose a problem, as PMMA cannot be spin-coated to a proposed 50μm thickness without causing cracks in the deposited film, as will be seen in chapter 4.

Use of polymer-waveguide technology for fabrication of microfluidic optical sensor for fluorescence or absorption spectroscopy has one important advantage over silica-based waveguide techniques. The relatively simple fabrication techniques along with increased design freedom enable significant reduction in system cost [35] while allowing for an improved performance. The optical sensor presented in this thesis falls within this category of devices. The main issues of this approach as deduced from this review include waveguides, microchannel and optical fibre alignment structures design and fabrication to minimize optical losses and maximize sensitivity while keeping device cost and complexity low.

2.2.4 Evaluation of designs

The operational and performance characteristics of the reviewed optical sensors for fluorescence or absorption detection are quite varied. As their underlying technologies are quite different, sensor designs offer in some cases lower detection limit on the expense of increased fabrication complexity and higher cost. A comparative system evaluation, in terms of sensitivity, fabrication complexity, portability, multianalyte detection capability, batch fabrication possibility and cost is summarized in Table 2.1.

Detection system:		Sensitivity[1] (LOD)	Fabrication[2] complexity	Portability[3]	Multianalyte detection capability[4]	Batch fabrication possibility[5]	Cost[2]
Fluorescence detection							
Microlenses	[23]	3.3nM	HIGH	YES	YES	LIMITED	HIGH
Encapsulated optical fibres	[24]	0.2-0.8fmol	LOW	NO	NO	LIMITED	LOW
	[25] [26]	25nM	LOW	YES	YES	LIMITED	LOW
IOWs: Evanescent wave sensing	[8]	N/A	N/A	YES	YES	YES	HIGH
	[27]	0.8mg/L	LOW	YES	LIMITED	YES	LOW
IOWs: Propagating modes sensing with silica waveguides	[29]	30μM	HIGH	YES	YES	YES	HIGH
	[16] [30]	20pM	HIGH	NO	YES	YES	HIGH
	[10] [15]	250pM and 100nM	HIGH	YES	YES	YES	HIGH
IOWs: Propagating modes sensing with polymer waveguides	[32]	N/A	LOW	YES	YES	LIMITED	LOW
	[33]	1μM	LOW	YES	YES	LIMITED	LOW
	[17]	64μM	LOW	YES	YES	LIMITED	LOW
	[14]	N/A	HIGH	YES	YES	YES	MEDIUM
Absorption detection							
IOWs: Evanescent wave sensing	[6]	10ppb (10μg/L)	MEDIUM	NO	NO	YES	MEDIUM
	[28]	N/A	MEDIUM	YES	LIMITED	LIMITED	MEDIUM
IOWs: Propagating modes sensing with silica waveguides	[13]	13μM	HIGH	YES	YES	YES	HIGH
IOWs: Propagating modes sensing with polymer waveguides	[34] [35]	15μM	LOW	YES	YES	YES	LOW

Table 2.1 Comparison of optical sensor designs

[1]Sensitivity is reported in terms of limit of detection, which is the minimum detectable concentration of the analyte.
[2]Fabrication complexity and cost are related to the number of fabrication steps, materials and processes used in device fabrication.
[3]Portability is evaluated in terms of light coupling scheme used for both excitation and emission.
[4]Multianalyte detection capability related to integration of multiple optical elements for interrogation.
[5]Batch fabrication possibility is evaluation of fabrication process for possibility of its automation.

3 Objectives of the project

As outlined in chapter 1, the objective of this thesis is to design and fabricate a microfluidic optical sensor for absorption and/or fluorescence detection based on intensity modulation, using the integrated planar waveguide technology. To do so effectively, design and fabrication steps need to be tailored to meet the system requirements under the existing fabrication constraints.

3.1 System requirements

In order to succeed among the competing sensing schemes, the proposed integrated optical detection system must exhibit performance characteristics such as high sensitivity, low sample consumption and parallel multianalyte detection capability. Furthermore, the fabrication of the device needs to be as simple as possible and amenable to mass production in order to reduce system costs. Finally, all the necessary components should be included that would allow system portability. A disposable system is also desired.

3.1.1 Design and fabrication requirements

To meet the general sensor requirements listed above, optimization of all parts of the integrated optical waveguide detection system needs to be considered: the waveguide, the waveguide interconnect and the microfluidic channel requirements need to be met.

Waveguides

The first component in the system is the optical waveguide, which is used to channel the light signal in the system. To achieve high sensitivity of the detection system, waveguides should exhibit low optical losses while minimizing chemical sample loss due to leakage. Optical losses to be minimized include coupling losses with the optical fibres that connect the external system components, and the waveguide propagation losses. To minimize the coupling losses, mode of the planar waveguide should match that of the fibre, which can be achieved by tuning the waveguide core dimensions, index contrast or refractive index (n) profile. The waveguide propagation loss can be minimized by ensuring that most of the light is guided by the core layer. This can be done by choosing the appropriate materials for the core and cladding layers with sufficient refractive index difference [38]. Furthermore, the chosen materials need to be transparent and must have

low autofluorescence in the near UV-Visible spectrum since most of the bio-chemicals absorb/fluoresce in this region. Furthermore scattering losses due to surface roughness, material impurities and fabrication imperfections need to be minimized through careful fabrication procedures [39]. To minimize the sample loss due to leakage the deposited core and cladding materials must be void-free. The deposition and etching processes must be controlled to minimize creation of voids. Finally, waveguide design should be relatively simple and its fabrication should be reproducible.

Waveguide Interconnect

The implementation of waveguide-fibre interconnects must be optimized to ensure that coupling losses and alignment complexity are minimized. Coupling losses are mainly due to lateral and vertical misalignments while coupling the planar waveguides to optical fibers that transmit light from the laser and to the detector. To minimize the misalignment related losses and decrease the overall interconnection complexity, the alignment method should be integrated on the wafer during the fabrication of the waveguides.

Microfluidic Channel

The main requirement for the microfluidic channel that needs to be satisfied through proper material selection is biocompatibility and chemical stability. Its width should be chosen to accommodate both fluorescence and absorption measurements. Furthermore, to ensure that sample concentration is minimized and not lost through channel leakage, the material for channel fabrication should be void-free as for the waveguide fabrication. Finally, the device packaging needs to ensure that the microchannel is completely sealed. Requirements for all the system components are summarized in table 3.1.

Waveguides	**Waveguide Interconnects**	**Microchannel**
- Low absorption coefficient in UV/Visible region - $n_{core} > n_{cladding}$ - Void-free - Reproducible and cost effective fabrication	- Minimize interconnect losses (due to misalignment) and their complexity	- Biocompatible materials - Chemically stable - Void-free - Low autofluorescence - Width to accommodate absorption and fluorescence

Table 3.1 System component requirements

3.2 Possible implementations

Based on the above requirements several possible system implementations exist varying in both the design and the fabrication materials and processes. These are compared next.

3.2.1 Design

Waveguides

Current integrated planar waveguide technology relies on either single mode waveguides (SMWs) or multimode waveguides (MMWs). Although both waveguide configurations can be used for fluorescence or absorption detection based on intensity modulation, the MMWs are preferred. It has been found that when used as an integrated part of the sensor system, MMWs achieve sensitivity that is an order of magnitude higher that that of SMWs [33]. This is due to the large core dimensions of MMWs which provides bigger cross-section area for light transmission and collection. With the increased excitation volume in the channel, the accuracy of the measurement is also increased, since signal to noise ratio is higher thus enabling higher sensitivity [14,35]. Another advantage of MMWs is that the alignment tolerances are relaxed, thereby reducing packaging costs. Furthermore, less stringent fabrication precision with enabling low-cost fabrication technologies can considerably reduce the system costs [36,40].

Coupling methods

To couple integrated waveguides with optical fibres, two methods are generally employed; one uses on-chip fibre self-alignment integration, while the other employs bulk alignment equipment for this purpose. The self-alignment coupling method can be achieved by means of etched grooves during the waveguide fabrication process. This technique enables fast and easy fiber coupling without any special equipment which reduces assembling costs substantially [37]. Alternative methods of coupling fibers to the fabricated waveguides could be achieved using bulk alignment and testing equipment that would position the fiber core optimally with respect to the waveguide core such that minimal coupling loss is measured. Once this optimal alignment is achieved, fibers are permanently glued to the waveguide structure using UV-Visible transparent glue. This procedure is both time consuming and costly, which could prohibit the mass production of the sensor. On the contrary, self-alignment of the optical fibers with respect to the waveguides by means of the etched grooves, a scheme used in some commercial systems, is very simple and alleviates the above-mentioned problems, but requires careful design of the waveguides to match the dimensions of the coupling optical fibre.

3.2.2 Fabrication material selection

Structural materials of the waveguide core, cladding and microchannel need to meet all of the functional requirements outlined in the previous section, and their combination must be compatible with the available waveguide fabrication techniques. The majority of advances in the development of materials and their fabrication processes for integrated optical waveguide systems have been driven by telecommunications. However these systems operate in the infrared spectrum which is not typically useful for fluorescence or absorption based sensing as these require transmission in the near-UV/Visible range. From chapter 2, we saw that there are currently two competing technologies satisfying this requirement: silica-on silicon waveguides and polymer waveguides on various substrates. Silica-based waveguides offer many advantages including excellent transmission characteristics and mechanical, chemical and temperature stability. A major drawback of this technology is the difficulty of fabricating a silica core of thickness greater than 5μm [27] which makes the coupling procedure complicated and may not meet the demand for the application in a deeper channel [33]. Furthermore, the fabrication procedures for silica waveguides relying on thin film deposition, using PECVD or FHD, and anisotropic etching are time consuming and costly [33,35]. Polymer optical waveguide technology may provide an expedient solution to this problem. Polymers offer similar optical properties as silica based waveguides, can be deposited in relatively thick layers and are easily patterned using methods such as photopolymerization or micromolding. A disadvantage of polymer materials that may restrict their use in some applications are low thermal resistance and high loss in UV wavelength range due to Rayleigh scattering that is intrinsic to specific polymer and caused mainly by fluctuations in material density. However, due to their suitability for mass production and very low cost of fabrication makes them more advantageous for disposable system development. Typical polymers that can been used for waveguide core fabrication are SU8, poly(methyl methacrylate) (PMMA), poly(styrene) (PS), poly(carbonate) (PC) and poly(siloxane) rubber [41]. One of the most versatile polymers currently is SU8, an Epon-based negative resist that is capable of producing large aspect-ratio structures with very smooth sidewalls, making it attractive material for waveguide core. It has excellent transmission in the near-UV/Visible wavelength range with

refractive index of 1.59 at 633nm thus enabling wide material selection for the waveguide cladding. It is easily deposited and patterned using spin-coating and photolithography and once fully cured it can withstand temperatures above 200°C. The choice of material will strongly depend on the design and fabrication constraints which for our system are discussed next.

3.3 Design and fabrication constraints

3.3.1 Design constraints

The buried channel waveguide detection scheme described relies on the monolithic integration of the optical waveguide components and the microfluidic channel. Therefore, the waveguide dimensions will also outline the critical dimensions of the fabricated microchannel, since all of the light propagating in the core of the waveguide is required to propagate through the section of the channel perpendicular to the waveguide. As such, the waveguide dimensions will put the limit on the microchannel depth, since the microchannel must be etched to reach the entire core section of the waveguide and at least a small portion of the cladding. The exact depth will depend on the sample concentration requirements with the maximum depth set by the waveguide thickness (core with upper and lower cladding). Waveguide dimensions will in turn be influenced by the size of readily available optical fibre used for light coupling due to requirement for wafer integration of the alignment scheme.

3.3.2 Fabrication constraints

The device should be fabricated at McGill microfabrication facility using the available etch and deposition processes (see Table 3.2) [42].

Material	Deposition	Etch
Oxide	Thermal oxidation	Reactive Ion Etch (RIE), HF wet etch
Photoresists	Spin-coating	Solvent development, RIE, Ashing
Silicon	None	RIE, TMAH wet etch
Metals (Al, Ti, Cr)	Sputtering	RIE, wet etch

Table 3.2 Available deposition and etch processes

Additionally, the fabrication should be relatively inexpensive and should allow for the completion of device production and testing during the course of this thesis.

3.4 Objectives

To meet the design and fabrication requirements under the above constraints, the following implementation has been chosen.

3.4.1 Chosen design implementation: waveguides, waveguide interconnects and microchannel

The optical waveguides for the system will be multimode since they enable larger cross-section area for light transmission and collection with relaxed alignment tolerances and less stringent fabrication precision. Since MMWs can have large core dimensions (>30μm), this will allow the fabrication of the inexpensive photolithographic masks using transparencies, thus considerably reducing fabrication costs. The alignment scheme will be implemented directly on the substrate via etched V-grooves. This will provide for simple system assembly alleviating the need for special alignment equipment. This is important since for multianalyte detection an array of waveguides is needed and without the integrated self-alignment scheme, the time needed to couple optical fibres to each individual waveguide would prohibit the mass production of the device. This however requires etching of the central waveguide/microchannel area perpendicular to the V-grooves to accommodate the deposition of the waveguides in line with the etched V-grooves. The microchannel will be defined by the same material as the optical waveguides, thus reducing the number of fabrication steps. The design schematic is shown in Figure 3.1.

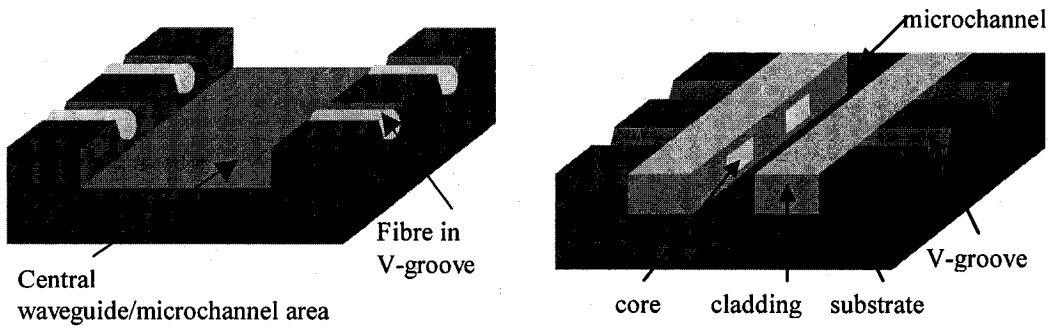

Figure 3.1 Design schematic showing V-grooves and central waveguide/microchannel area (a) Before waveguide deposition and patterning, with fibers inserted in V-grooves (b) After waveguide deposition and patterning

3.4.2 Chosen materials and corresponding fabrication processes

Substrate

A silicon substrate was chosen due to its inherent mechanical properties and readily available fabrication processes needed for integration of an optical fibre alignment scheme via V-grooves. Furthermore, choice of silicon as a substrate offers the opportunity to produce fully integrated structure for complete LAC system. To etch the central waveguide/microchannel area, an anisotropic deep reactive ion etch (DRIE) of the silicon substrate is chosen. The reason for employing DRIE etching is that vertical edges are required not to compromise the alignment features designed as opposed to isotropic etch which is likely to cause a reasonable amount of undercutting. To fabricate V-grooves, anisotropic etchants are used as they create desired structures in crystalline Si by etching much faster in <100> direction than in <111>, resulting in a V-groove geometric shape with groove angle of 54.7°. KOH and ethylene diamine pyrocatehcol (EDP) can be used for this purpose, however both are hazardous and require special handling care. On the other hand, a Tetramethyl Ammonium Hydroxide-Water (TMAHW) [$(CH_3)_4NOH$] solution is non-toxic, not expensive and can be handled easily. It also exhibits excellent selectivity to silicon oxide mask. Finally, it has been readily available in the microfabrication lab with a dedicated wet-etch bench, and thus was the etchant of choice for which thermally grown silicon dioxide was used as the masking layer. RIE was used to pattern the oxide because it enables controlled etch profile unlike wet HF (Hydrofluoric) oxide etch which causes undercut in the patterned structures.

Waveguide core

Due to the advantages of polymer materials over silica for MMW fabrication and also lack of equipment for doped silica deposition, spin-on polymers were chosen for waveguide fabrication. In particular, SU8 resist was chosen for the core material primarily because, unlike many other polymers, SU8 is compatible with standard silicon processing conditions and can be patterned using a standard I-line mask aligner [36,43]. Furthermore, it can be easily deposited to the desired thickness (1-300μm) using single spin-coating procedure. This is important for waveguide core layer, as multiple coatings to achieve requisite thickness lead to added loss due to scattering at the interfaces of the core layers. It has very high optical transparency in the near-UV/Visible range (400-

700nm; 95% transmittance at 633nm) and a low polymer shrinkage rate of 7.5% after curing [44]. During the patterning and post-exposure step, the SU8 is crosslinked and becomes resistant to most organic solvents, which makes it suitable for a variety of microchemical applications for which other polymers may not be candidates [43]. Finally, its refractive index is 1.59 at 633nm, allowing for a wide range of materials for the cladding layer.

Waveguide cladding

PMMA, a high resolution e-beam resist, was chosen for the waveguide cladding because it exhibits excellent optical properties in UV/Visible range and can be deposited in the same manner as the waveguide core. Its refractive index is 1.49 giving the refractive index difference of 0.1 which should allow for excellent light confinement in the core layer. When spun-on and baked, PMMA generates a low stress film that adheres well to silicon substrate. This is important as stress induced in the cladding layers with the additional processing will cause cracks in the film which can result in sample leakage and device failure. A drawback of using PMMA however is that it cannot be patterned using standard photolithography since it is essentially insensitive to wavelengths below 260nm. Deep UV lithography (DUV) can be used to pattern PMMA, however with SU8 as the core layer, this procedure is not recommended as SU8 is extremely absorbent at these wavelengths which would degrade its optical properties and cause deformations in the fabricated patterns. Therefore, RIE in oxygen plasma was a method of choice for PMMA patterning. To pattern PMMA film using RIE etch, a hard mask was required. The two materials that could serve this purpose and that were available in the sputter tool were Cr and Al. Cr is generally preferred over Al as a mask for RIE etch, since Al is known to suffer from micromasking effect, where Al particles get redeposited on the wafer during etching process. However, during fabrication process development, it was found that sputtered Cr adheres poorly to PMMA even under high vacuum conditions producing low quality film. Hence, Al film was chosen for this purpose due to its availability, cost effectiveness and quality of process control.

Microchannel

The microchannel is released in the same step that the waveguide cladding is etched. As such, it is defined by the waveguide boundaries and thus the materials used for the

waveguide core and cladding layers. Both materials are biocompatible and meet the requirements stated in the previous section. The channel width will be chosen to accommodate both fluorescence and absorption detection schemes, without compromising the sensitivity of the system.

3.4.3 Summary of objectives

The objectives of this project are thus to design and fabricate at McGill microfabrication facility a microfluidic optical sensor for absorption and fluorescence detection based on intensity modulation, which employs the multimode polymer waveguide technology with integrated V-grooves. Although both the design and fabrication play an important role in system performance, the accent is given to the fabrication process development as the final product and its characterization was a requirement for the thesis completion. The system requirements and proposed solutions are summarized in Table 3.3.

Waveguides	**Waveguide Interconnects**	**Microchannel**
- Low absorption coefficient in UV/Visible region - $n_{core} > n_{cladding}$ - Void-free - Reproducible and cost effective fabrication at McGill microfabrication facility	- Minimize interconnect losses (due to misalignment) and their complexity	- Biocompatible materials - Chemically stable - Void-free - Low autofluorescence - Width to accommodate absorption and fluorescence
Solution: Spin coating of PMMA cladding and SU-8 core patterned by RIE and photolithography respectively	*Solution:* Implement alignment (V-grooves) directly on the Si wafer during waveguide fabrication using TMAH etch	*Solution:* both PMMA and SU-8 satisfy these requirements

Table 3.3 System component requirements and proposed solution

4 Design of the integrated optical detection system

To meet the project objectives outlined in chapter 3, careful design of each component needed to be made. This included the waveguide interconnections (V-grooves), the waveguides and the microfluidic design layout for the selected fabrication materials. This chapter describes the design of the integrated optical detection system including the evaluation of the system performance.

4.1 V-grooves, waveguides and microfluidic channel design

Due to the nature of the monolithic integration of V-grooves, waveguides and microfluidic channel, it is of paramount importance to ensure that the final structures have the same height thus providing planar surface for final channel sealing (Figure 4.1).

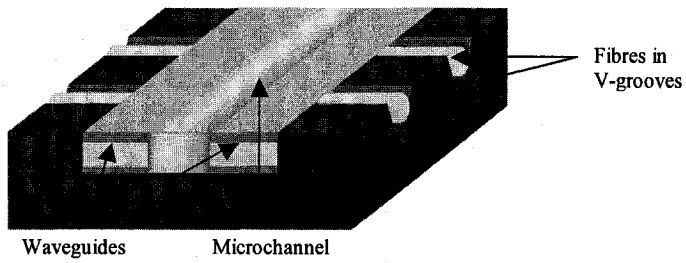

Figure 4.1 Device schematic showing planar surface required for channel sealing

Therefore, optical fibres need to be completely embedded in the fabricated V-grooves. As such, V-groove dimensions need to accommodate the MMFs used for coupling. This will in turn affect the depth of the central waveguide and microchannel trench which should reach the entire fibre core to ensure efficient coupling of both, the excitation and the emission light. This is depicted in figure 4.2.

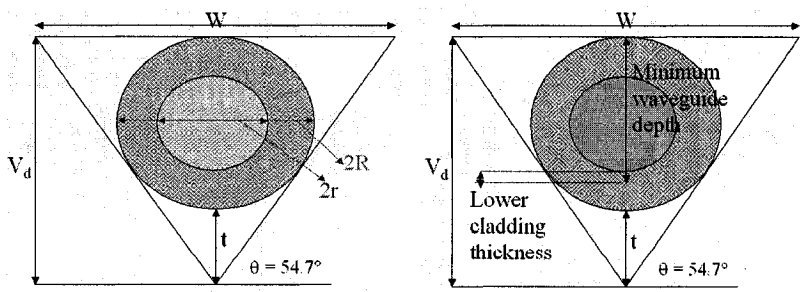

Figure 4.2 Design geometry

The actual thickness of the waveguide core and cladding layers will be limited by the fabrication processes. As will be seen in Chapter 5, the material chosen for the waveguide

cladding (PMMA) cannot be deposited in layers thicker than 5μm without compromising the structural integrity of the device. This means that if a standard MMF with 50μm core and 125μm cladding is to be used for coupling, the required core (SU8) thickness is 82.5μm. A geometry mismatch of this magnitude would result in huge losses of the emitted light from the microchannel during output waveguide to fibre coupling. In order to keep these losses low, a non-standard MMF was ordered from Polymicro [45] which had outer diameter of 65μm with 40μm core. This then required 47μm core thickness. The resultant dimensions have been calculated from the design geometry shown in the figure below.

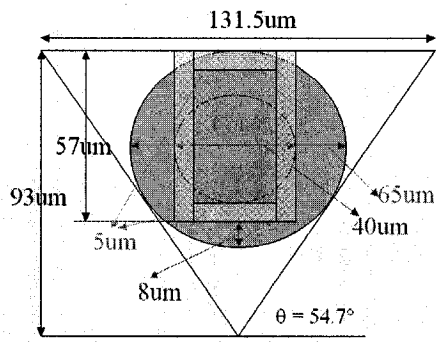

Figure 4.3 Design geometry with computed component dimensions

For the above geometry, core width was determined based on maximum coupling efficiency using BPM (Beam Propagation Method) simulation [46] (Figure 4.4).

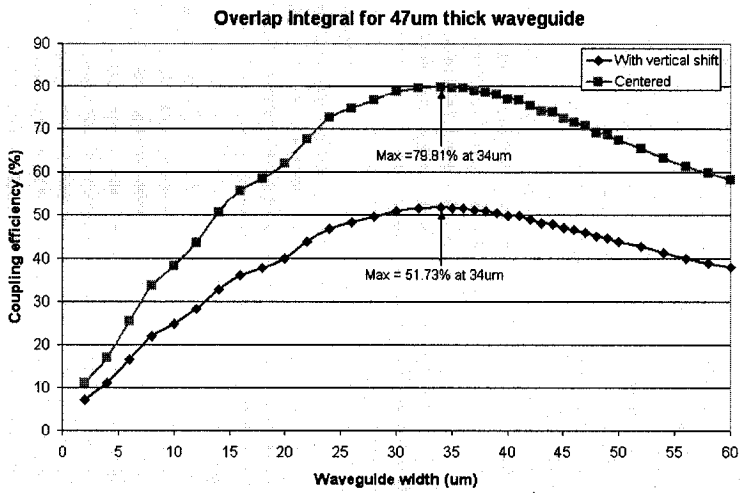

Figure 4.3 Coupling efficiency vs. waveguide core width for 47μm core thickness

This was done by modeling both the waveguide and the fibre fields and computing the resultant overlap integral for the fundamental mode. Overlap integral was computed by

first assuming that the fibre core is axially aligned with the waveguide core, for which 79.81% efficiency was obtained. Next, the vertical misalignment was taken into account for which coupling efficiency decreased to 51.73%. For both cases, the maximum coupling efficiency for 47μm thick core occurred at a width of 34μm. The absolute maximum coupling efficiency obtainable with the fibers used is 97.3% for square core design with 34μm dimensions. However this optimum waveguide design would require 11.5μm thick lower cladding which could not be achieved. It should be noted that rigorous analysis would require computation of an overlap integral for all the modes, however due to the large number of propagating modes in the fibre and the waveguides, this would be impossible to do. The above result was verified using ray optic analysis to obtain the optimum waveguide width for maximum coupling condition [47,48]. The computation was carried out with the assumption that the fibers and the waveguides were composed of the same materials (see Figure 4.4) and the fiber misalignment was neglected.

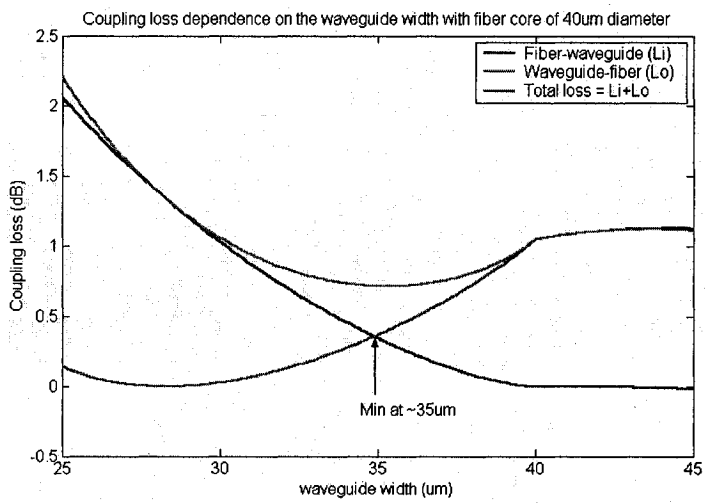

Figure 4.4 Coupling loss vs. waveguide width for 40μm thick core

From figure 4.4, it was found that the minimum coupling loss occurs at the waveguide width of 35μm, which was in close agreement with the BPM simulation (see Appendix A for Matlab code). Hence, the optimum waveguide width was chosen to be 34μm. An array of 10 waveguides was implemented on the mask layout for device fabrication with the varying waveguide width so that theoretical values for optimum waveguide width can be compared to that obtained experimentally. Finally, channel width was chosen to be 500μm which should be sufficient to accommodate both, fluorescence and absorption

measurements by preventing excessive loss of fluorescence emission light during propagation in the channel towards the output waveguide, while at the same time allowing sufficient propagation length in the channel for adequate absorption of the signal respectively.

Now that all the critical dimensions have been determined, the actual layout of the waveguide and the microchannel structures resulting from the fabrication processes was anticipated to ensure that the final device surface is planar as required for channel sealing. Two methods for waveguide fabrication are depicted in Figure 4.5 [15].

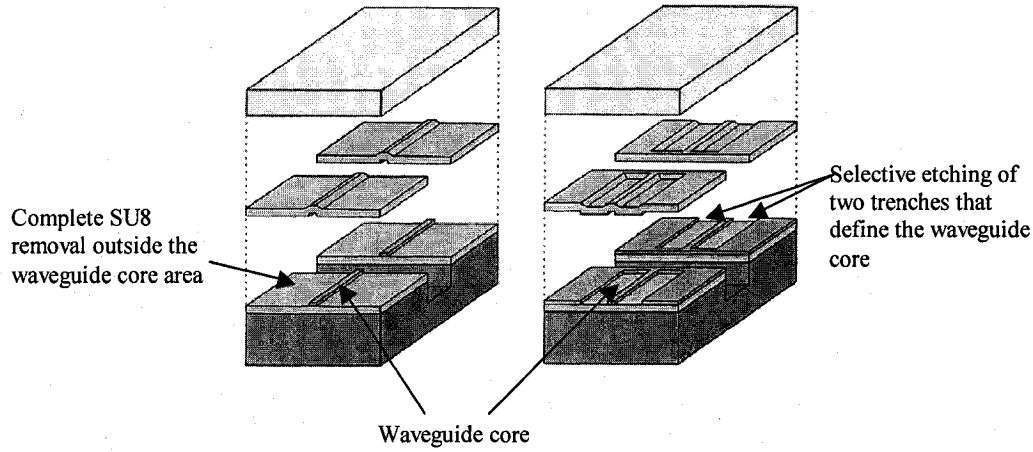

Figure 4.5 Waveguide fabrication methods resulting in (a)Uneven topography making channel sealing difficult; (b) Planar surface required for channel sealing [15]

The first method defines the waveguide core by etching the SU8 film everywhere outside the 34μm wide strip. This results in an uneven topography, as the subsequent PMMA cladding deposition will be inherently thicker at the core strip area. This would make channel sealing difficult if not impossible. The second method solves this problem by selective etching of two trenches that define the waveguide core. Furthermore, a narrow bonding strip (10μm) is left in the SU8 layer between the etched trenches and the microchannel to ensure that no sample leakage occurs in the trenches due to height difference. The final device after core patterning and upper cladding deposition is shown in Figure 4.6 and the dimensions of all components are summarized in Table 4.1.

Parameter	V-grooves	Waveguide core	Microchannel	Device
Length	5mm	100μm	20mm	20mm
Width	131.5μm	34μm	500μm	10.72mm
Depth/Thickness	93μm	47μm	57μm	625μm

Table 4.1 Final device dimensions

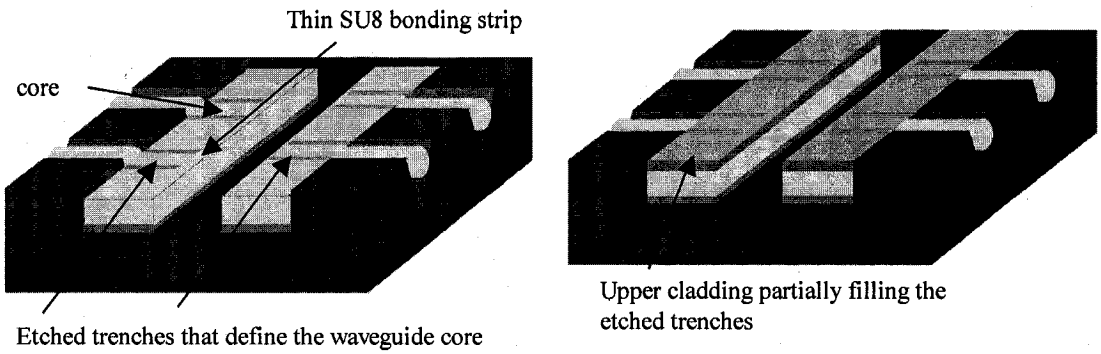

Figure 4.6 Final device after waveguide core patterning and upper cladding deposition

4.2 Performance evaluation

Now that the dimensions of all components have been determined, the device performance is assessed by modeling the above system. Specifically, transmission efficiency and fluorescence collection efficiency are simulated for the above design. It should be noted that this was carried out at the same time as the device fabrication, thus system optimization was not attempted.

4.2.1 Transmission efficiency

Transmission efficiency is computed using BPM power overlap integral for incoming optical fibre mode that enters the input waveguide and propagates through the entire device with the microchannel being modeled as air waveguide. The refractive index distribution is shown in the figure below.

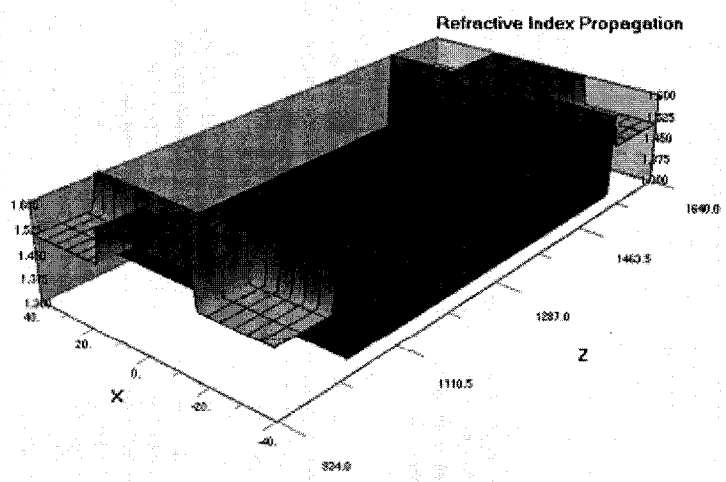

Figure 4.7 Refractive index distribution

The optical field propagation is shown in Figure 4.8 and the power overlap integral is shown in Figure 4.9.

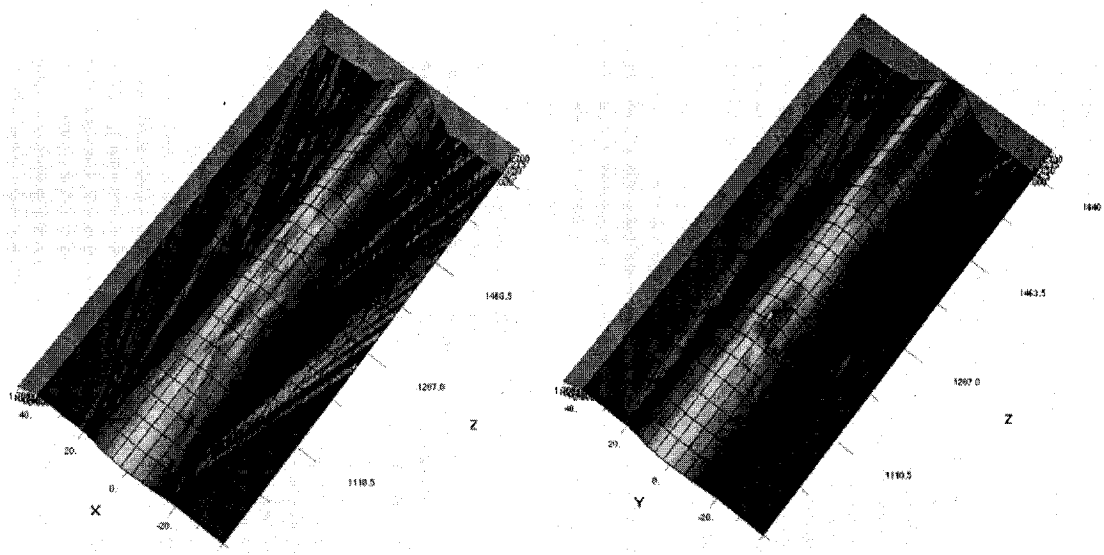

Figure 4.8 Optical field propagation

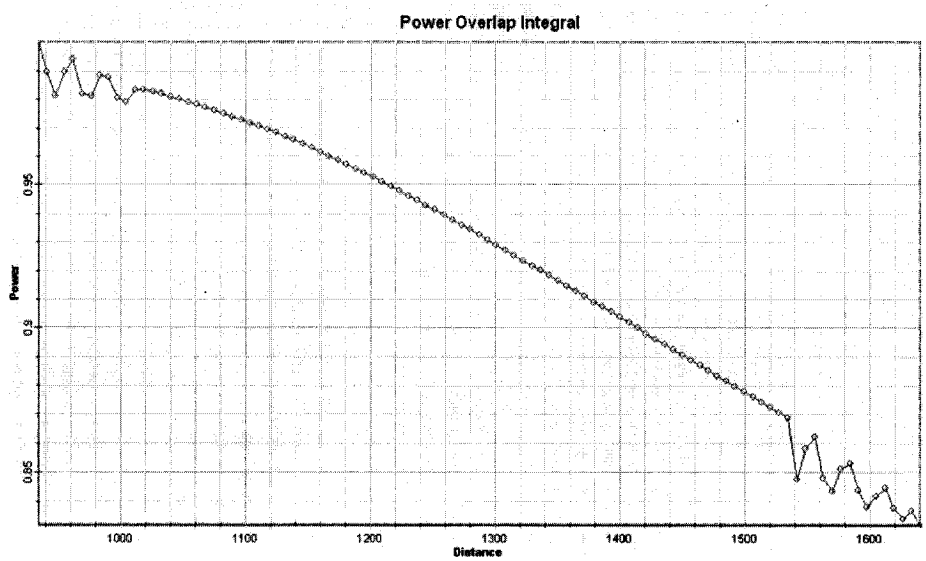

Figure 4.9 Power overlap integral

From Figure 4.9, transmission efficiency is estimated to be 83% (0.8dB loss). This is an overestimation, as for the above propagation, only the fundamental mode was considered. Furthermore, waveguide and fiber cores were assumed to be completely transparent at the propagation wavelength (633nm), which is not the case in practice. Actual absorption coefficient for the SU8 waveguides strongly depends on the fabrication processing parameters and needs to be determined experimentally. Also, fabrication induced

irregularities at the waveguide core layers were not taken into account, while in practice such surface roughness will increase the scattering losses.

4.2.2 Fluorescence collection efficiency

Following the preliminary assessment of the excitation light propagation through the device, the fluorescence light collection efficiency of the output waveguides was also determined using a ray tracing software Code V [49]. Essentially a model of the output waveguide coupled to the optical fibre was implemented in software for which the illumination and the resulting optical power at the detector was evaluated as a function of fluorescent particle displacement inside the 500μm wide microchannel over a 400μm length. This was done by placing a point source inside a microchannel for which 180° emission angle was specified to approximate the emission of a fluorescent particle in the direction of the output waveguide. The configuration is shown in the schematic below.

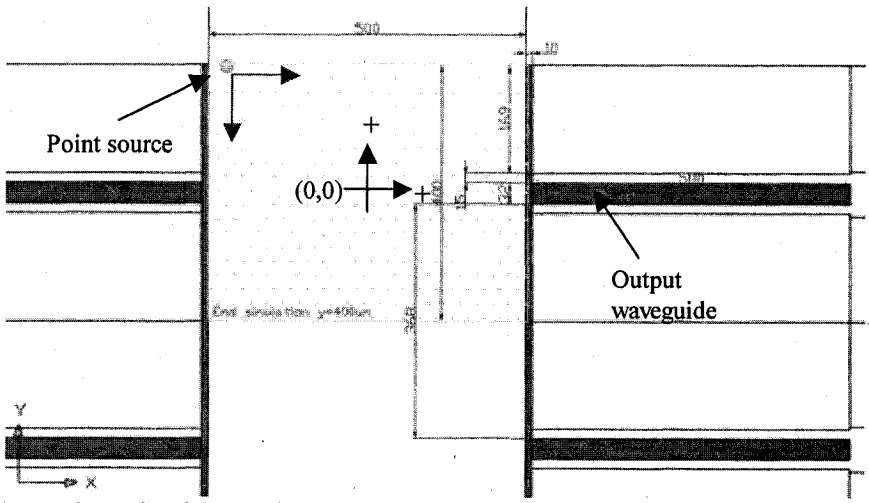

Figure 4.10 Schematic of the configuration used to determine the waveguide collection efficiency

The detector was positioned at the coupling fiber endface and the emission is collected for 99 points corresponding to the particle displacements in 50μm increments in horizontal and vertical directions along the channel. Due to the design symmetry, it was sufficient to implement the above model for one waveguide and the obtained results can be applied for all the subsequent waveguides in the array. The 3D view of the implemented model is shown in the figure below including the rays traced through the waveguide-fiber configuration. For the generated lens file that models the system, please refer to the Appendix B.

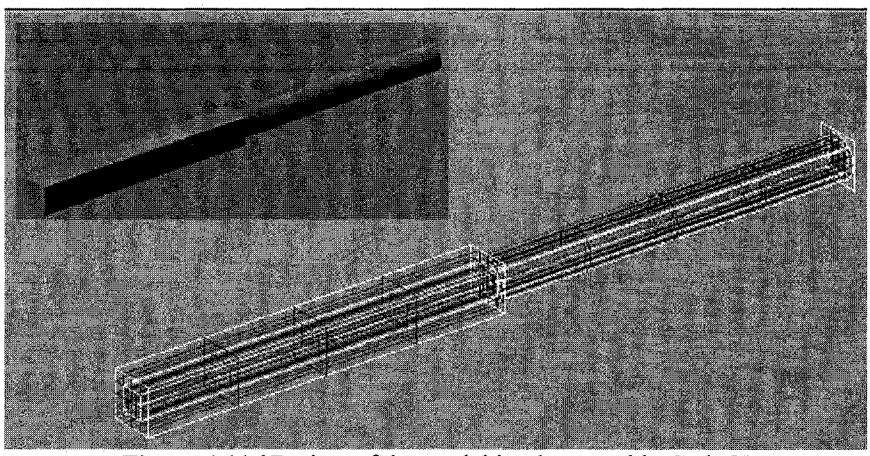

Figure 4.11 3D view of the model implemented in Code V

Figures 4.12 and 4.13 show the illumination maxima at the detector and the corresponding total power for various particle locations at microchannel bound by the area shown in Figure 4.10 for which (0,0) point is located at the center of the channel.

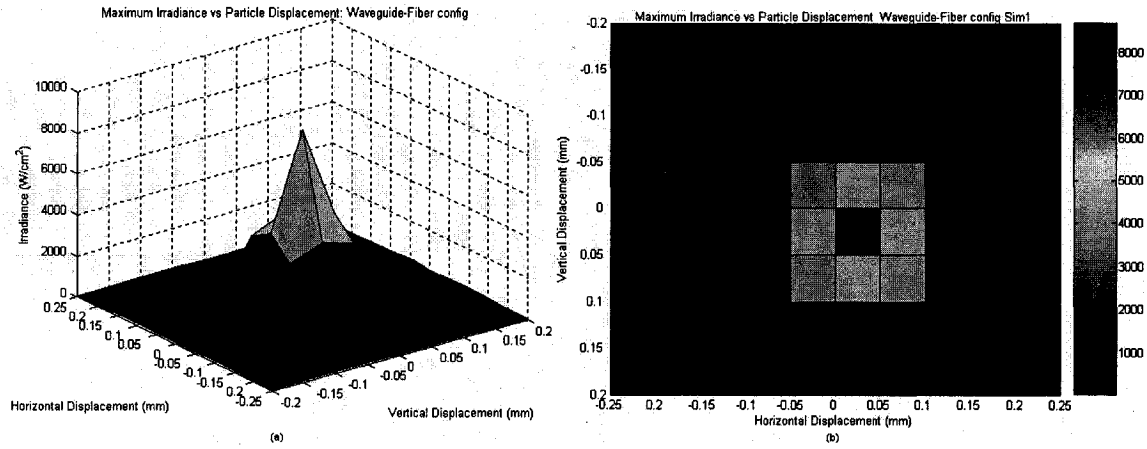

Figure 4.12 Illumination maxima vs. particle displacement as detected by the receiver

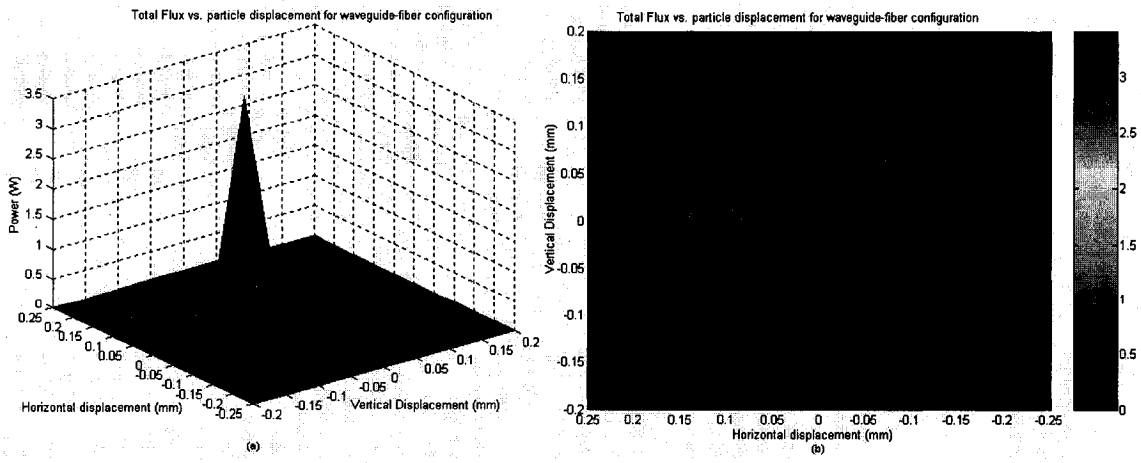

Figure 4.13 Total flux vs. particle displacement as detected by the receiver

In the above figures, positive value for horizontal movement indicated particle approaching the waveguide from the center, and positive values for the vertical movement indicated the points above the channel center (indicated by "+" sign in Figure 4.10). The absolute illumination maximum at the receiver was obtained when the particle was located at a horizontal distance of 200μm from the waveguide. At this location 51% of the rays actually reached the detector. Maximum value of the power, which was the result of illumination integration over the detector area, occurred at a horizontal distance of 100μm from the waveguide. For this particle location, 61.7% of the emitted rays reached the detector, which was the maximum collection efficiency obtained for the system. Relative illuminations at these two points are shown in the figure below.

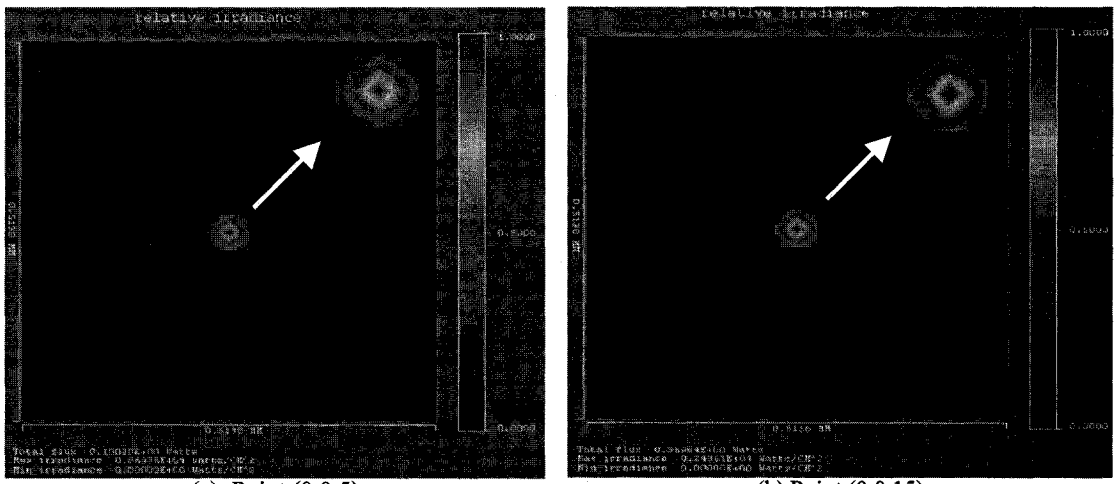

(a): Point (0,0.5) (b) Point (0,0.15)

Figure 4.14 Relative illumination at the detector for the particle location at which (a) Maximum illumination occurs (b) Maximum power is detected

The above simulations, in addition to evaluating the maximum fluorescence collection efficiency can also facilitate analytical measurements. For instance, using the obtained results for the total power received, an analysis of particle displacement in the solution can be performed. During specific fluorescence measurements in which a single labeled cell or a molecule is analyzed, its exact position could be determined by simple power reading. In a different application, this can also serve as an indication of the position at which a chemical reaction occurred. By making use of the velocity profile of the target analyte, the time needed for reaction to occur can be determined.

5 Fabrication: Process flow and recipe development

This chapter describes the process flow developed for the fabrication of microfluidic optical detection system in polymer-on silicon based technology. It first starts with an outline of the steps involved in the device fabrication (section 5.1) that set the stage for the individual development of the fabrication procedures for each of the steps outlined in the fabrication process flow. These are included in sections 5.2 to 5.7.

5.1 Process Flow

The following section outlines the process flow developed for the fabrication of the microfluidic optical detection system. The process flow is divided into four parts: silicon wafer patterning, waveguide fabrication, channel formation, and device packaging. Silicon wafer patterning requires two masks for etching of the central square trench to accommodate the waveguides and the microchannel, and etching of the fiber interconnecting V-grooves. Waveguide fabrication shows deposition and formation of the waveguide core and cladding layers and requires one mask. Channel formation uses one mask for the final release of the microchannel. Finally, device packaging shows the bonding procedure required for channel sealing. The figures for each fabrication segment show only relevant cross sections for simplicity purposes. The simplified device layout with the relevant cross sections referred to in the process flow, is shown in Figure 5.1.

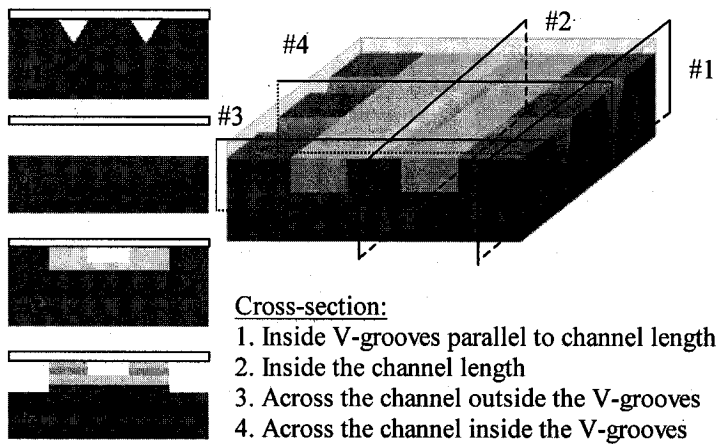

Figure 5.1 Simplified device layout and relevant cross-sections

The major steps of the fabrication process are presented in Figures 5.2-5.5 and briefly explained in the sections below. The detailed process flow with the final recipes used for the device fabrication is provided in Appendix C and the full development of each

process recipe is described in the remaining sections of chapter 5. In the process flow, the sequence of processes has been carefully chosen to accommodate the fabrication to the available resources of McGill microfabrication facility [42] with the exception of a silicon deep reactive ion etching (DRIE), which was carried out at Cornell University. The relevant materials, etching, deposition and equipment used are shown in table 5.1.

Materials:	**Etch:**	**Deposition:**	**Equipment:**
Silicon wafer	DRIE etch of Si; TMAH	N/A	Unaxis SLR 770 (Cornell); wet TMAH bench
Photoresist S1813	PR stripper; ashing	Spin-coating	Spinball coater/developer; EVG 620 Mask Aligner; Tegal O_2 Plasma Etch
Oxide mask	RIE etch (CF4/CHF3); Buffered HF	Wet thermal oxidation	Tylan 4-stack furnace; Applied Materials P5000 4 Chamber RIE; wet HF bench
PMMA cladding	RIE (Ar/O_2)	Spin-coating	Programmable oven; Applied Materials P5000 4 Chamber RIE
Aluminum	PAN etch	Sputtering	MRC 603-III DC sputter system
SU8 core	PGMEA developer	Spin-coating	Spinball coater/developer; EVG 620 Mask Aligner
PDMS for bonding	N/A	N/A	Tegal O_2 Plasma Activation

Table 5.1 Materials, etching, deposition and equipment used in the fabrication process flow

5.1.1 Silicon wafer patterning

Starting with a standard, RCA cleaned, 625μm thick Silicon wafer with <100> top and bottom surfaces, a centrally located square trench is produced to accommodate for the waveguides and the microchannel (Figure 5.2(a)). This is done using photolithography to pattern the photoresist (PR) which will serve as a mask for the following etching of the substrate. An anisotropic DRIE etch of silicon is chosen to avoid any sort of undercutting which could lead to alignment problems. The DRIE etch will also ensure vertical side walls for the square cavity which is essential for the waveguide-to-fiber alignment. The choice of different etching and deposition mechanisms is justified more elaborately in the previous chapter and in the detailed process flow. After the square pit is produced, the V-grooves are etched into the silicon substrate using anisotropic TMAH etch for which oxide mask is employed (Figure 5.2(b)). Thermally grown silicon oxide is patterned using photolithography and RIE. The TMAH etch, being least selective to the <111> surface, etches the silicon by leaving behind only the <111> surfaces inside each groove. Hence, the desired shape for the grooves is obtained.

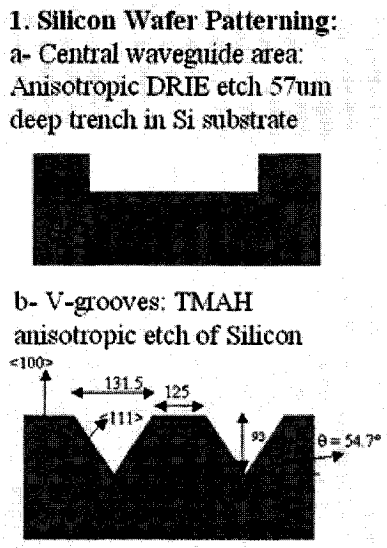

- Pattern Si:
  - Create Waveguide area (T = 57μm) – **Mask 1**
    - Photolithography (PR 2um)
    - DRIE Etch Si (57μm)
    - Ash PR
  - Create V-Grooves – **Mask 2**
    - Deposit Silicon Oxide – 800nm (mask for TMAH)
    - Photolithography (PR 1.4μm)
    - Etch Silicon Oxide (pattern using RIE) and ash PR
    - TMAH etch Si: 93μm deep V-groove
    - Remove remaining Silicon Oxide (HF bath)

Figure 5.2 Silicon wafer patterning

5.1.2 Waveguide fabrication process

After groove formation, PMMA is deposited by spin-coating onto the wafer to act as the lower cladding for the waveguides. The next step in the process flow is SU8 deposition and patterning to form the core of the waveguides. The core is patterned using photolithographic techniques, and the upper cladding is then deposited in the same manner as the lower one (Figure 5.3).

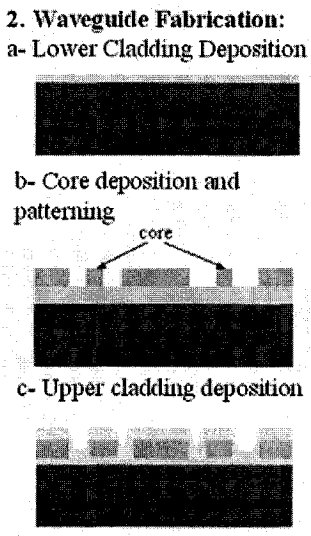

- Waveguide fabrication:
  - Lower Cladding Deposition:
    - Spin Coat PMMA (5μm thick)
    - Anneal in programmable oven
  - Core Deposition and patterning – **Mask 3**
    - Spin coat SU8 (47μm thick)
    - Prebake
    - UV Expose
    - Postexposure bake
    - Develop
  - Upper Cladding Deposition:
    - Spin coat PMMA (5μm thick)
    - Anneal in programmable oven

Figure 5.3 Waveguide fabrication process

5.1.3 Channel formation process

In the next step, excess cladding material is removed from all areas outside the waveguide region thus defining the channel and releasing the V-grooves (Figure 5.4). This step is performed using RIE for which Al hard mask is deposited and patterned using photolithography and wet PAN etch.

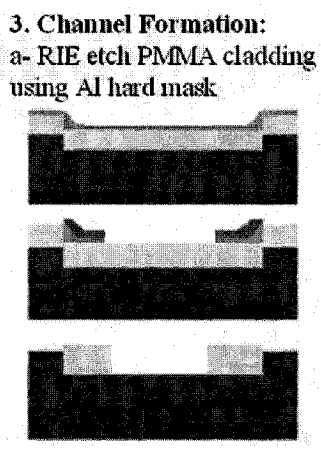

- Cladding removal everywhere outside the waveguide area:
  - Photolithography – **Mask 4**
    - Al deposition (250nm) to serve as hard mask
    - Photolithography – Mask 4 (PR 1.4um)
    - PAN etch Al (pattern)
    - RIE etch PMMA (also removes PR)
    - PAN etch remaining Al mask

Figure 5.4 Channel formation process

5.1.4 Device packaging

The final step consists of the device sealing using either plasma or thermally activated PDMS cover which contains fluidic interconnect holes. PDMS lid bonds to the device by applying external pressure (Figure 5.5). Fluidic interconnects can then be adjusted to each ends of the channel via interconnect holes for sample injection purposes. Multimode fibers can be inserted and self-aligned using fabricated V-grooves and attached to the waveguides by means of UV curable adhesives.

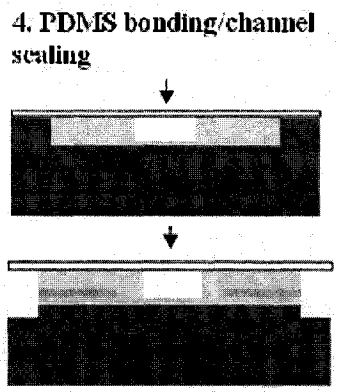

- Final PDMS Bonding
  - Plasma or thermally activated bonding of PDMS cover to seal the microchannel and protect the device

Figure 5.5. Device packaging

5.2 Masks

The mask used in a photolithographic process is the key component in a fabrication process [50]. A traditional mask consists of a UV-transparent glass plate with the pattern generated by deposition of thin metal film, typically chrome (Cr). These masks, while producing high quality images with micron/sub-micron features, are also quite expensive when trying to build microfabrication capabilities at the university level with each mask costing around $700 each. There are several options available for low cost photolithographic masks. One of them is transparency or mylar mask that can be generated using a 3600dpi or better photoreproduction quality laser printer, through commercial printing services and costs around $25. Hence, it offers the lowest cost and quickest turnaround, usually the same day. One drawback is that minimum feature size is limited to 30μm. By defining the geometries of the device down to 30μm, the initial project goal was to use the inexpensive transparency masks to fabricate the device. The following section describes the steps used to generate the transparency mask and the results obtained, highlighting the need for more expensive chrome mask.

5.2.1 Transparency Mask

The layouts for the four masks have been designed using AutoCAD software [51] by applying the design rules provided by ADTEK Photomask [52] to generate closed polylines. Once the mask layout was generated, the AutoCAD's DXF file format is converted to EPS file and the files were sent for transparency printing. The turnaround time was approximately 3-4 days. The printed transparencies were inspected using an optical microscope, and no defects were observed, meaning that the features translated perfectly to the transparency. The next step was to produce the 'home-made' chromium masks by lithographically transferring the transparency features onto a 5" chrome-coated glass plate. For this purpose, transparency with patterns for V-groove fabrication was used first. A glass slide was coated with 0.5μm of Cr onto which 1.4μm of positive photoresist, S1813 was deposited and baked. The transparency was then laid out onto this glass slide with the printed side down and another blank glass slide was put on top of it. A metal rim was used to clamp the three together by carefully adjusting the screws on the rim to eliminate any air voids between the plates. The metal rim was then loaded into the

EVG mask aligner and exposed for 4.5sec. Following the exposure, the photoresist was developed for 50sec to be used as a mask in subsequent chrome etching. The Cr was etched for 4min in Cr developer, rinsed and finally the photoresist was stripped with acetone. The first inspection using an optical microscope showed that some of the alignment marks were missing, indicating that not all the features got transferred onto the Cr. This was due to the shadows generated under the transparency from the light source. Next, it was observed that the patterns of the etched channels were not all well defined and their widths seemed to vary across the mask. This observation was verified using the profiler, which showed indeed a variation in pattern widths in excess of 40μm across the mask and 6.2μm across a single device. Further observation showed very rough sidewalls (see Figure 5.6a), which would create defects in the transferred structures (Figure 5.6b) in the early stage of fabrication (photolithography) and thus the effects of other process steps such as dry or wet etching could not be assessed. Moreover, rough sidewalls from the mask would especially affect the waveguide fabrication, as prohibitive light scattering losses resulting from the core roughness would seriously impede the device performance.

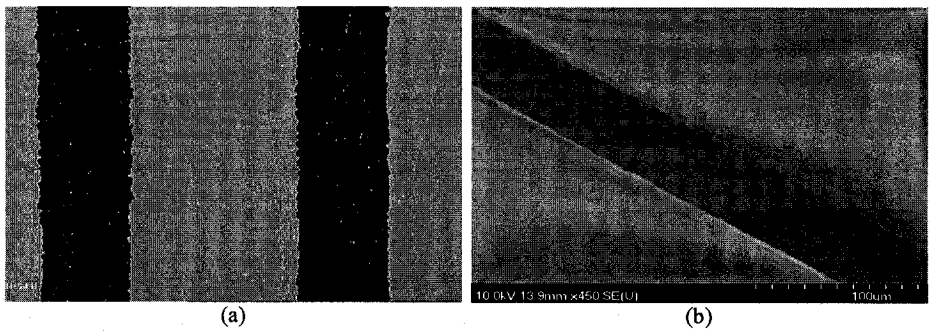

(a) (b)

Figure 5.6 (a) Patterns on the home-made chrome mask from transparency showing rough sidewalls (b) transferred sidewall roughness in SU-8 pattern as imaged using a scanning electron microscope (SEM)

5.2.2 Professional chrome masks

For all the above reasons, it was decided to order the more expensive masks from ADTEK Photomask [52]. Due to high cost of these masks ($690/mask), instead of ordering four masks, each for a given layout, only two masks were ordered by placing two mask designs onto one layout. This required two exposures for each mask. In each exposure, one side of the mask with the desired features was exposed, while the other side was covered with an aluminum semi-disk specially designed for this purpose (Appendix D, Figure D.2). After first exposure, the mask was rotated and the same

procedure was repeated. This method allowed for a substantial reduction of the cost associated with device fabrication, as photolithography presented the most expensive fabrication step [50]. The final designed masks are included in Appendix D.

5.3 Silicon trench deep reactive ion etching (DRIE)

The first step in the process flow required etching of the central square trench in Si substrate to accommodate the waveguides and the microchannel. In order to reach the goals of fabrication using resources available at McGill Nanotools Microfabrication Facility, the initial plan was to use the Applied Materials P5000 4 Chamber RIE system with $HBr/Cl_2/O_2$ gas compositions for this purpose. However, preliminary test showed slow etch rates (0.3μm/min), which would require extremely long process runs, in excess of three hours, in order to etch 57μm deep trench. Due to the aggressive nature of the chemistries used in the etch process, long runs would severely damage the RIE chamber mechanism and hence an attempt to etch the 57μm deep trench has not been made. The only plausible solution was to use the DRIE etch specifically designed to etch deep trenches in silicon substrates with vertical sidewalls using 2μm thick photoresist mask. Due to unavailability of this system at McGill, it was decided to outsource the DRIE fabrication step. The wafers were patterned lithographically at McGill, and sent to Cornell University for further processing [55]. The turnaround time was one week and the cost per wafer was USD$98. Next section describes wafer preparation for DRIE, including photolithography. This is followed by the general description of DRIE process and the results obtained from Cornell.

5.3.1 Photolithography

Photolithography involves spin-coating of the resist, followed by the softbake and UV-exposure. Next, the exposed resist is developed, rinsed and spin-dried. Finally, obtained patterns are hard baked to promote film hardness. These process steps, with values for each parameter used to pattern Shipley S1813 photoresist are briefly explained below.

1. Spinning Resist

The wafer was placed on the wafer platen of the Spinball coater/developer automated system with the vacuum chuck holding the wafer in place (Figure 5.7). The photoresist

was then dispensed dynamically onto the slowly spinning wafer (300rpm). This was done with the dispense arm moving from the center to the outside edge of the substrate. The advantage of this method is a reduction in the amount of coating necessary for the wetting process, better elimination of voids, and greater film uniformity at the substrate's outer edge [54]. At an acceleration of 10,000rpm, the wafer was then spun at high speeds (3900rpm for 1.4μm thickness and 1950rpm for 2μm thickness) for 30sec to produce a uniform film. At these speeds, centrifugal force resulted in radial flow and while most of the liquid was swept off the disk leaving only a thin film [56], a small amount of the solution built up at the edges, creating the so-called "edge bead." This had to be removed at the final stage of spin-coating program to ensure uniform film across the wafer. For further informations on spin-coating process, please refer to [22,53-56].

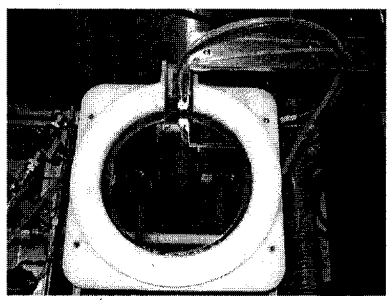

Figure 5.7 Spinball resist spinner with the wafer positioned at the wafer platen

2. Prebake or Softbake

After spin-coating, the resist was prebaked on a hot plate at 90°C for 1min to remove the solvent and built-in stress and promote adhesion of the resist film to the substrate.

3. Exposure

After softbake, the resist was exposed using broadband EVG 620 Mask Aligner (Figure 5.8). This step transferred the features of the mask to the exposed resist by altering the solubility of the resist in solvent using radiation.

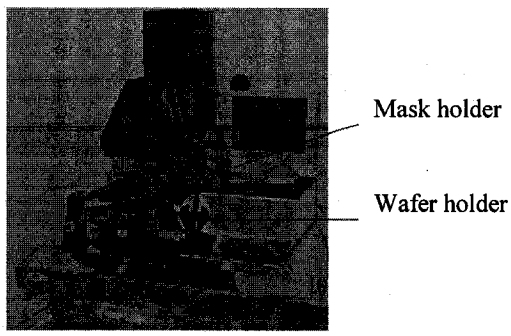

Figure 5.8 EVG 620 Mask Aligner

The mask was loaded into the aligner image side down and vacuum held just below the microscope objectives. Next, the wafer was loaded underneath the mask, and using the adjustment screws the wafer was aligned with respect to the mask. Following the alignment, the microscope retracted, and the wafer/mask were exposed to the high intensity light. The incident energy or dose across the surface of the film (in mJ/cm^2) was computed by multiplying the incident light intensity (in mW/cm^2) by the exposure time (in s). The exposure dose used was approximately $70mJ/cm^2$. Proximity printing, where the mask and the wafer were separated by a distance of 1μm was employed to minimize defects caused by contact printing and prevent mask degradation.

4. Development

Development was performed using Spinball coater/developer system. After placing the wafer on a wafer platen, the dispense arm dynamically dispensed the solvent onto the wafer at slow spin speed to spread it uniformly over the wafer. The wafer was then left to sit for 50sec, during which selective dissolving of the exposed positive resist took place. Next, the wafer was rinsed with de-ionized (DI) water and spun at high speed to dry.

5. Postbake

Following the development step, postbaking was performed to remove residual solvents, and promote film hardness and adhesion. It was carried out at 115°C for 2min.

Process Optimization

All of the above parameters affect the quality of the patterned resist and careful, often yearlong optimization of the above process steps needs to be carried out in order to obtain smooth, vertical sidewalls that transfer the features of the mask with perfect fidelity. The spinning step is of primary importance to the effectiveness of pattern transfer, since the quality and the uniformity of the resist film determines the density of defects transferred to the device [22]. To obtain the needed film uniformity of +/-0.3% that would ensure reproducible line widths and development times in subsequent steps, optimization of the regular resist coating process in terms of resist dispense rate, dispense volume, spin-speed, ambient temperature and humidity present a major challenge.

Prior to the time of the chip fabrication, these processes have not been established at our microfabrication facility, and the initial recipe yielded rough sidewalls with 61.5° slope (Figure 5.9(a)). Much effort has been made on the part of McGill microfabrication staff

to resolve this issue and full optimization is still in process. However, due to the time constraint, during this project, full optimization was not reached and the best possible sidewall slope of 80° was obtained (Figure 5.9(b)) using the values listed in Table 5.2.

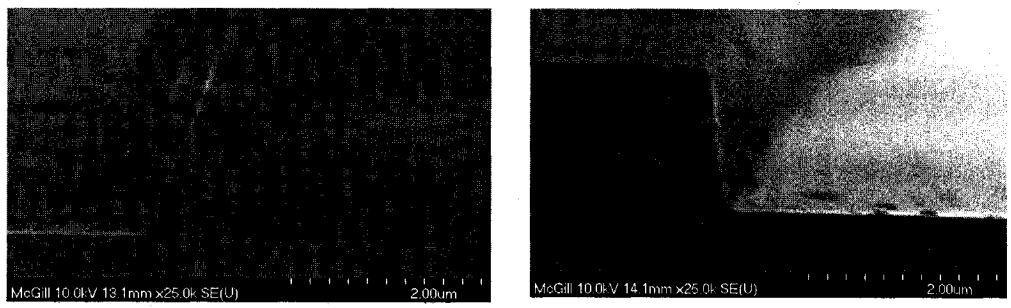

Figure 5.9 Image showing photolithography results using (a) preliminary recipe that yielded 65° sidewall slope (b) optimized recipe that yielded 80° sidewall slope

Process Step	**Initial Recipe**		**Optimized Recipe**	
Spin-coat	1.4μm	2μm	1.4μm	2μm
	3900rpm	1950rpm	3900rpm	1950rpm
Prebake	60 sec at 100°C		60 sec at 90°C	
Expose	50mJ/cm^2		70mJ/cm^2	
Develop	60 sec		50 sec	
Postbake	60 sec at 100°C		120 sec at 115°C	

Table 5.2 Initial and optimized recipe for patterning S1813 positive photoresist

5.3.2 DRIE

Using the optimized recipe listed in Table 5.2, the 2μm thick photoresist mask was formed and the wafers were sent to Cornell University for DRIE etching of a 57μm deep trench in silicon substrate employing the Bosch fluorine process. The equipment used for this step was a Unaxis SLR 770 inductively coupled plasma (ICP) / reactive ion etcher providing etch rates of 2μm/min. An advantage of ICP etch tool over conventional plasma systems lies in their ability to generate high plasma densities, while maintaining low pressures (<10mTorr) [57]. High plasma density enables high etch rates while low pressure operation reduces ion scattering allowing precise control of etch profiles. Furthermore, low pressure discourages microloading, a problem commonly encountered with conventional plasma etch systems [22]. Hence, by employing DRIE Bosh process, 57(+/-1)μm deep trenches with vertical sidewalls have been obtained (Figure 5.10). Note that the operating conditions for the DRIE process employed by Cornell University were not available to us due to copyrights, and thus are not reported on.

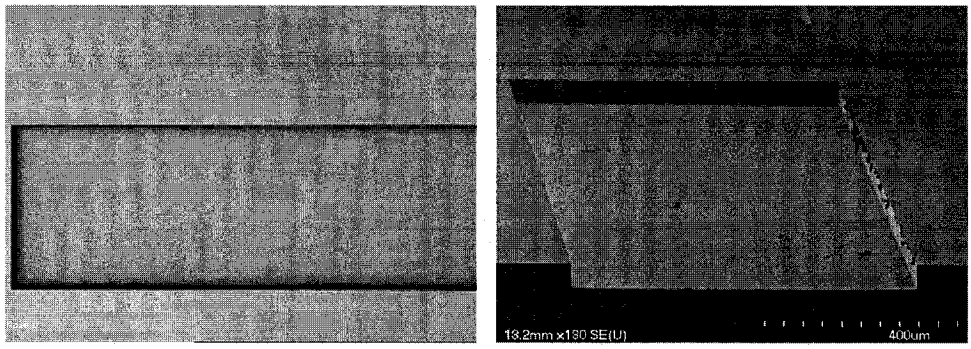

Figure 5.10 57μm deep trench DRIE etched in Si substrate viewed from the top using an optical microscope and SEM

After DRIE, the remaining photoresist mask was etched using Tegal O_2 Plasma Etch system for 40min at RF Power of 200W.

5.4 Anisotropic TMAHW etching

To etch the fiber-waveguide interconnecting V-grooves, wet-chemical TMAHW anisotropic etching of Si substrate was employed. TMAH has {100}/{111} etch rate ratio of 36:1-59:1 [22] and oxide selectivity (Si etch rate/Oxide etch rate) of $5.3x10^3$ [59]. The etch rate in TMAH etching is reaction rate controlled and thus temperature dependant (Figure 5.11). The etch rate for all planes increases with temperature and the surface roughness decreases with increasing temperature, so best results are obtained with etching at higher temperatures [22]. These are typically 80-85°C and are used to avoid solvent evaporation and temperature gradients in the solution. For this reason, the solution was heated to a temperature of 85°C. Depending on the fabricated structure application, different concentrations of TMAH can be employed, yielding different etch rates (Figure 5.11(a)), however, a concentration above 22% is preferred, since lower concentrations result in more pronounced roughness on the etched surface. In order to obtain smooth sidewalls, a concentration of 25% of TMAH in water was used. As mentioned in chapter 3, TMAH exhibits excellent selectivity to silicon oxide mask (Figure 5.11(b)), hence, RIE patterned thermal oxide was used for masking purpose.

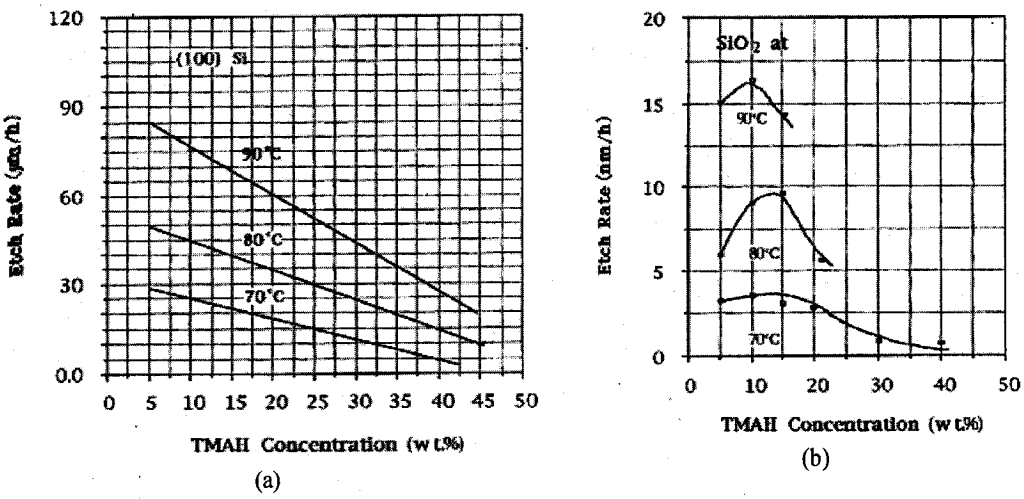

Figure 5.11 Etch rate as a function of TMAH temperature and concentration of (a) (100) silicon; (b) silicon oxide [58]

The complete process for V-groove fabrication is explained in more details below.
In order to assess TMAH etching of V-grooves in silicon substrates, blank test wafers were used. To remove any resist residue, a piranha clean was performed on the wafers for 10min, followed by DI water rinse and N_2 dry. Clean wafers were then pushed into Tylan 4-stack furnace at 50cm/min for wet thermal oxidation at a temperature of 1150°C for duration of 60min. The thickness of the grown oxide layer was measured using Promatrix and was found to be 0.837μm with 0.15% uniformity. The next step required photolithography (section 5.3.1) to define the patterns in the oxide mask to be etched with the RIE. The patterned resist served as a mask for the oxide RIE etch with chemistries that are highly selective to oxide (Table 5.3).

Parameter	Value
Gases (sccm)	CHF_3=30
	CF_4-1 = 7
	Ar = 70
RF Power (W)	720
Magnetic Field (Gauss)	70
Pressure (mTorr)	150

Table 5.3 Silicon oxide RIE recipe

Using the above recipe, the obtained etch rate of oxide was approximately 390nm/min. Several tests were run, and the time required to fully etch 0.84μm of oxide as inspected by Nanospec thin film measurement system, was found to be 137sec. The etch rate of

S1813 photoresist in this chemistry was found to be 1.55nm/sec (oxide : resist selectivity was 1:4.2). Following the oxide patterning, the remaining photoresist was ashed in Tegal O_2 Plasma Etch system for 40min at RF Power of 200W. After ashing, the remaining resist residue was removed by placing the wafer in Piranha solution for 10min, followed by DI water rinse and N_2 dry. Then the wafer was pretreated by briefly dipping it into concentrated HF solution for 20sec. This step was needed to remove the native oxide that was formed during Piranha clean, which would otherwise hinder the silicon wet etch. Finally the wafers were placed in 25% concentrated TMAH etch solution at 85°C, for 1hour to determine the etch rate. The solution was not stirred, and several wafers were processed for this purpose. The maximum etch rate for fresh TMAH bath was found to be 28.5μm/hour with 1.3% etch depth variation across the wafer. Therefore to etch approximately 93μm deep groove, 3hours and 19minutes were required (Figure 5.12).

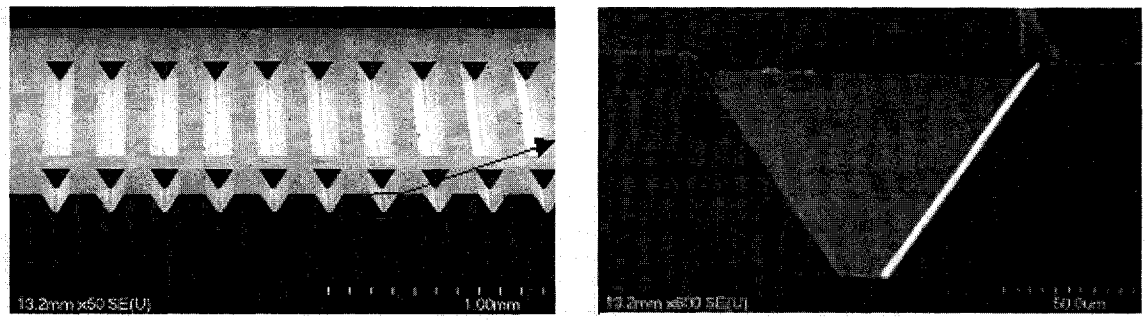

Figure 5.12 SEM photographs of V-grooves etched for 3hours 19minutes in fresh TMAH solution

Several observations have been made with respect to TMAH silicon etch characteristics. First, it has been found that TMAH etch produces an orange peel-like surface [59]. Second, the surface roughness was found to increase with the number of processed wafers, while the etch rate tended to drop. After 15-20 processed wafers, the etch rate decreased to 23.7μm/hour, and the (100) etching fronts were covered significantly with pyramidal shaped hillocks bounded by (111) crystal planes (Figure 5.13).

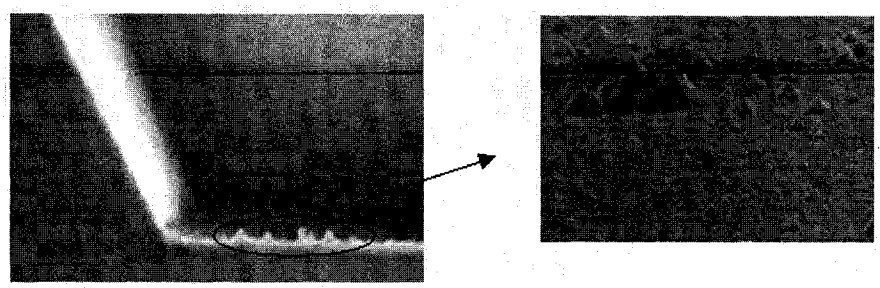

Figure 5.13 Hillocks formation on (100) crystal plane

Formation of the hillocks was linked to a decrease in the pH value due to an increase in silicon concentration during etching [59]. These hillocks slowed down the etch rate significantly which could be prevented if ammonium persulfate is added to the solution [60]. However for the final device production, fresh TMAH solution was used for which no hillocks were observed (Figure 5.14).

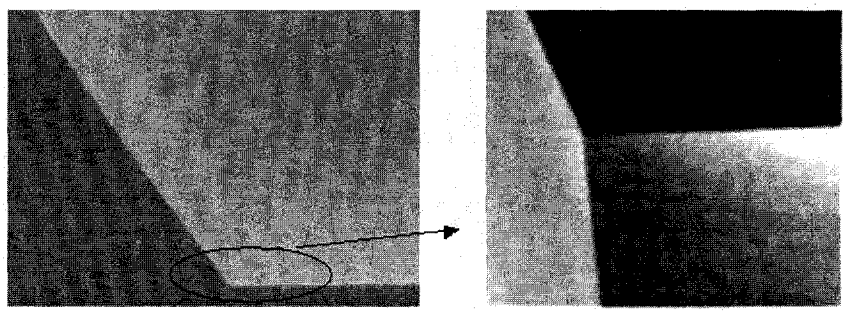

Figure 5.14 Smooth surface for silicon etch in fresh TMAH solution

Finally, after successful TMAH etch of the V-grooves, the remaining oxide mask was etched using 10:1 HF solution with etch rate of 23.5nm/min for a total time of 40min to ensure complete removal of the oxide layer. The wafer was then rinsed with DI water and dried using nitrogen.

5.5 PMMA deposition

A first step in the waveguide fabrication process required the deposition of the PMMA cladding layer. The initial goal was to deposit 10μm thick PMMA cladding that would in turn yield optimum device performance, since the thickness of the SU8 core would be matched to maximize the coupling from/to the optical fibre (see Chapter 4). In addition to this, requirements of uniform, crack-free film needed to be met in order to avoid scattering losses [39] and leakage of the analyte from the microchannel (Chapter 3). Using the datasheet provided on the manufacturer's website, it was found that 10μm thick layer would require multiple coatings of PMMA (Figure 5.15). This datasheet was used as a starting point for developing the process parameters.

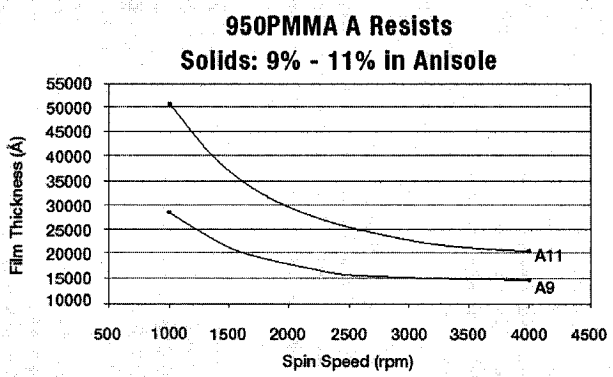

Figure 5.15 PMMA film thickness vs. spin speed [61]

To develop a process for coating uniform PMMA film, Bidtec R&D Spinner was used initially. This tool required manual dispensing of the resist solution and syringe was used for this purpose. The process commenced by placing a 6" wafer on the spinner and static dispensing 8ml of the PMMA solution from the syringe, followed by ramping the spin speed to 2250rpm at high acceleration rate and holding for 45sec. This gave non-uniform film thickness with variations in excess of 1μm across the wafer as measured with Promatrix film thickness map. The non-uniformity was mainly due to voids that are caused by trapped air bubbles inside the dispensed solution. To prevent bubble formation during dispense, the size of the orifice was increased and the syringe was heated in the oven at 55°C for 30min. Although this removed the air from the syringe completely prior to dispensing, it did not improve the film uniformity. Finally, the PMMA was dispensed on the center of the wafer directly from the bottle, which gave 3.4μm thick film with 4.154% uniformity. Next, the PMMA was baked on hot plate at 180°C for 60 sec as recommended by the manufacturer [61] after which the thickness decreased to 2.99μm and uniformity improved to 3.2% uniformity. From this, a thickness decrease due to solvent evaporation was determined to be 12%. After this, a second coat of PMMA was deposited in the same manner and baked at a slightly lower temperature (170°C) for 75sec. The mean thickness measured after the second coat was 5.59μm with 6.69% uniformity. Therefore, with multiple coats, non-uniformity was increased. Finally, third coat of the film was applied, however PMMA cracked after this deposition (see Figure 5.16).

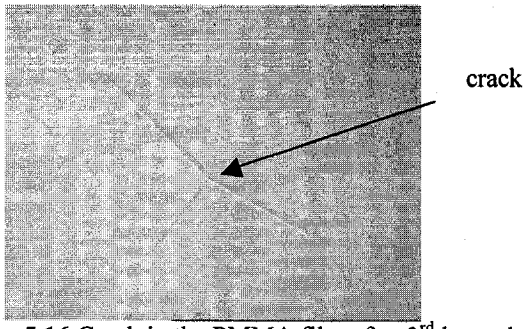

Figure 5.16 Crack in the PMMA film after 3rd layer deposition

It was presumed that the first two bakes did not cure the film completely so when the third bake was performed, the solvent in the lower layers while trying to escape, caused the cracks in the upper layer. To resolve this, different baking schemes were explored, namely baking was performed in programmable oven by slowly ramping the temperature and baking for longer times to reduce the film stress.

Bake Recipe 1

The recipe that was tried first, has been published by Musa et al [40]. They reported a smooth, uniform 10μm thick PMMA layer deposition using three layer coating, where each layer was cured at 100°C for 10min. In our experiments, the same deposition at 2250rpm spin speed (3μm thickness) was used and the bake was performed with 5°C/min temperature ramp. After each layer, the wafer was left to cool to room temperature for 30min before subsequent depositions to reduce thermal stress. While the uniformity after the second deposition was improved to 4.7%, the cracks appeared after the third layer deposition as before.

Bake Recipe 2

The second bake recipe, used to resolve the crack issue, has been developed by researchers at the University of Wisconsin-Madison [62]. They used 496,000 molecular weight PMMA (9% concentration) to deposit 8μm thick film using multiple 1.6μm thick layers at spin speed of 2000rpm. In their recipe, each layer was carefully annealed in a precision bake-out oven by ramping to 180°C at 1°C/min, holding at 180°C for 1 hour and ramping to room temperature at -1°C/min. They wrote that this procedure was stable and has been used to produce spun-on films of 30μm thickness. In our recipe, the actual bake time at 180°C was increased to 3 hours to accommodate for each layer thickness difference (3μm compared to 1.6μm). The uniformity of each deposited layer improved

using this recipe, (3.24% after second layer). The three layers have been successfully deposited to a total thickness of 8.68μm, however, after fourth layer, small cracks started to appear. This indicated that multiple-layer thick PMMA cladding would crack under the deposited core layer due to the high stress induced by multiple deposition-bake procedures.

Bake Recipe 3

In an attempt to further decrease the film stress, the third bake recipe was tried. The maximum temperature was decreased to 135°C, and the ramp rate was reduced to 0.1°C/min. However, with this program, the cracks appeared at the third layer.

In addition to cracks, hardened PMMA particulates were observed in the film (see Figure 5.17). These particulates were found to be the crust of the dried resist that stayed on the rim of the bottle and has been introduced on the wafer by pouring the solution directly from the bottle. For this reason, automated dispense needed to be used for the final device production.

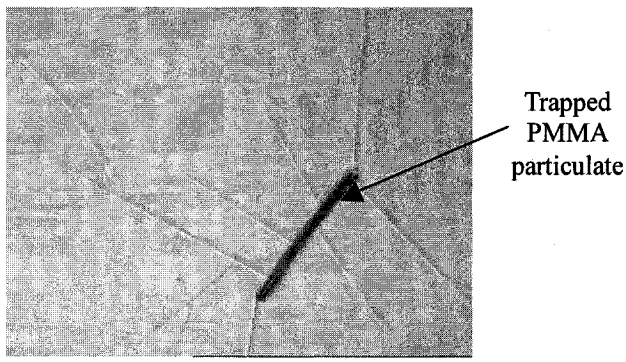

Figure 5.17 Hardened PMMA particulate

For this purpose, Spinball coater/developer automated system was used instead of Bidtec R&D spinner. The cartridge dispense system provided by the tool solved the contamination problem due to manual dispense, however another problem associated with this particular machine was observed. At spin speeds exceeding 1500rpm, a thin spider web of PMMA formed between the edges of the wafer and the coater cup, due to their close proximity (see Figure 5.18), which then tended to fall onto the wafer once the spin cycle is complete, causing contamination (Figure 5.19).

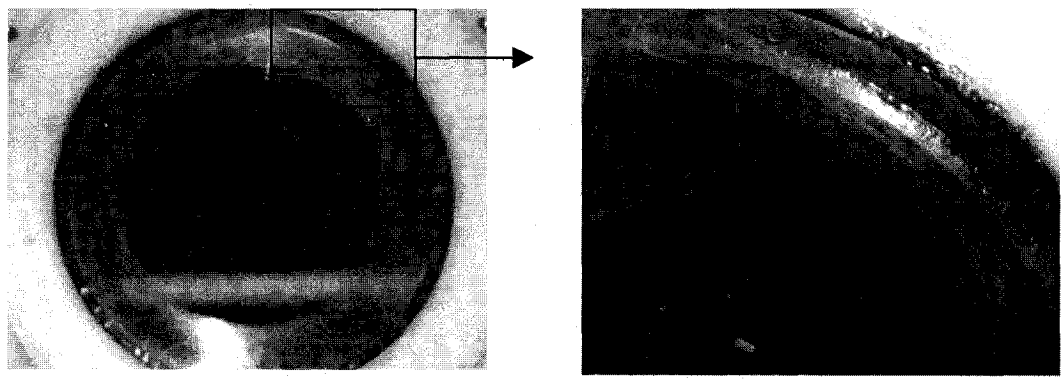

Figure 5.18 Thin spider-web formation between the wafer and the spinner cup during PMMA deposition at spin speed of 2250rpm

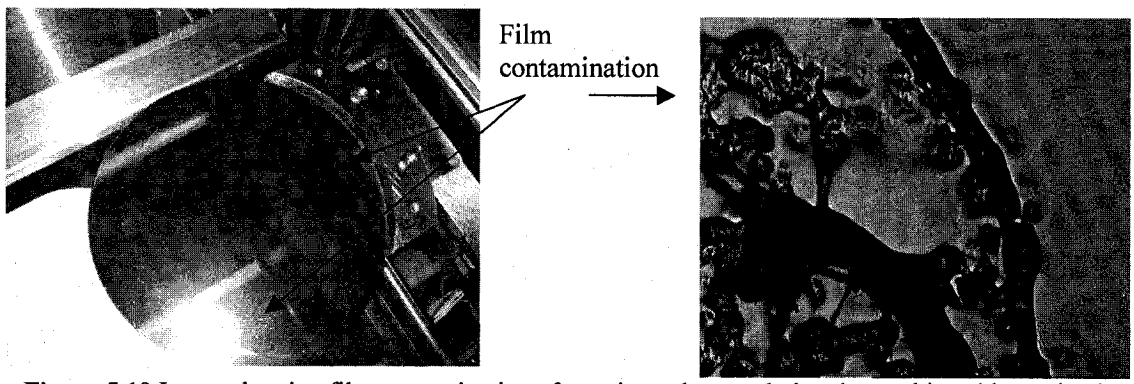

Figure 5.19 Image showing film contamination after spin cycle completion due to thin spider-web taken with digital camera and 20x microscope objective

This problem could only be resolved by manually extracting the thin web during spin-coating using a pair of tweezers. However this did not guarantee contamination-free film as particles could be introduced on the wafer by mere manipulation above it during processing. Therefore in order to produce contamination-free film, automatic dispense with slow spin-speeds needed to be used. For thickness of the order of 10μm two layers deposited at 1000rpm and baked using the second anneal recipe were explored. However after the second deposition and bake, the film was covered with cracks. The thicker layer created more stress and several modified bake times were tried, including annealing for 5, 7 and 10 hours at 180°C and decreasing the ramp rate to 0.1°C/min, but the cracks were always present. This indicated that a single PMMA layer would have to be used for lower cladding in order to maintain the structural integrity of the device. Thus, single-coat of PMMA at very slow spin speeds (500rpm, 600rpm, 700rpm, 800rpm and 900rpm) was explored to obtain the required thickness however, the maximum thickness obtained was 7.5μm at 500rpm but the uniformity was compromised due to such slow spin speed.

Finally it has been decided to use a single layer of 5μm thick PMMA, automatically dispensed and coated at 900rpm followed with bake using the above recipe [62] with 3 hour cure at 180°C. This gave 5μm thick lower cladding layer with optimum uniformity (3.01% or 0.51%std). The final recipe is summarized in the table below.

Step	Spin Speed (rpm)	Time (s)		Bake Step	Temperature	Total time
Dispense	0	10		Ramp	1°C/min	155min
Spin	500	5		Soak	180°C	3hr
Spin	900	60		Ramp	-1°C/min	155min

Table 5.4 PMMA deposition and anneal recipe

Two main reasons for using a single 5μm layer of PMMA were structural integrity and contamination control. Increase in the tensile stress induced by multiple layer deposition caused the film to crack. This stress has been measured using TENCOR FLX-5200 thin film stress measurement system and has been found to quadruple with the second layer deposition (see Table 5.5) for the same cure recipe.

Wafer #	**Spin speed(rpm)**	**Stress (MPa)**
1	900 (5um)	19.4 tensile
2	900 (5um)	20.1 tensile
3	900 (5um)	19.6 tensile
4	2250 (2.5um)	17.2 tensile
5	2x2250 (5um)	92.1 tensile
6	2x900rpm (10um)	108.6 tensile

Table 5.5 Stress measured for single and multilayer PMMA films

It should be noted that the effect of this tensile stress has been seen during the attempt to pattern SU8 core on multilayered PMMA cladding, where, during the development stage, all the experiments resulted in the cracking of the PMMA underneath the SU8 (see section 5.6). Hence, even though the optical coupling losses would increase by decreasing the cladding thickness while increasing the deposited core thickness (2.74dB increase in waveguide-fibre coupling losses), this was the only viable option to obtain defect-free structures.

5.6 SU8-25 process development

To meet the requirements for the fabrication of the waveguide core (Chapter 3) including smooth straight sidewalls and voids and crack-free structures, the SU8-25 *(63.3% solids; viscosity = 2646cSt)* process development required careful control of all the parameters involved, including spin-coating the resist, prebake, exposure, post-exposure bake and

development. Furthermore, once the process was developed for direct SU8 on Si deposition, the processing parameters, especially exposure dose and development time needed to be adjusted for SU8 film deposited on PMMA-coated Si substrate. Exposure dose adjustment was carried out to compensate for change in substrate reflectance due to the deposition of the PMMA cladding layer since this affected the energy coupled into the SU8 film [63,67]. The development time needed optimization to reduce stress induced in the cladding layer that would otherwise result in cracking of the film. The process development hence included both, the SU8 on Si process optimization and the SU-8 on PMMA coated Si substrate process adjustment.

5.6.1 Process optimization

The challenges for fabricating a thick microstructure include SU8 coating, baking process, SU8 developing efficiency and residual stress formed after the curing of SU8 [64]. Film coating, besides tailoring the spin speed to match the exact resist thickness, also needs to be tailored for maximum surface flatness to facilitate the subsequent lithography process. As already mentioned, one problem associated with spin-coating is the so-called 'edge bead effect', which will cause a poor lithography image in the center of the wafer due to the air gap created by the edge bead, between the mask and the coated substrate. This problem becomes even more prominent when using thick resist film on substrates with topography. The baking process, if carried out on a flat leveled hotplate can to a certain degree resolve the edge bead problem, since the resist will reflow at temperatures higher than its glass transition temperature (Tg) for resist thickness up to 50μm [73]. Besides edge-bead control, prebaking process of SU8 resist is considered to be of paramount importance for its lithographic quality [65-68], while post-exposure bake (PEB) which initiates further film crosslinking, dictates the generation of internal film stresses [69-72]. Exposure dose is also found to be of critical importance for final film quality, as both underexposed and overexposed film decrease the resolution of the transferred features and are prone to delamination and cracking during development [67,73]. Next, timed development is needed to fully release high-aspect ratio structures while minimizing the amount of overetch associated with wet-etch process. Finally, rinsing and drying of the wafer needs to be optimized to remove the residues, while

improving film quality. All of the above issues were encountered and addressed while developing SU8 processing specifically adapted to square waveguide core fabrication. All experiments were performed on 6" test wafers and the process steps are explained in more detail below.

1. Wafer preparation

The test wafers used in these experiments had undergone extensive processing in the past. It was found that their cleanliness played an important role in the quality of processed film, and was largely responsible for the poor film adhesion. Hence, before depositing SU8, wafers were cleaned in Piranha solution for 10min to remove all the organic residues, followed by DI water rinse and dehydration bake at 200°C for 30min in convection oven. Note that this step was performed before PMMA deposition for SU8 on PMMA-coated Si wafers.

2. Resist Spin

Spin-coating of the resist was carried out using Spitball coater/developer automated system in order to prevent bubble formation associated with manual dispensing. Using the information provided on the manufacturer's data sheet for SU8-25, for the thickness of 47μm, the required spin-speed is stated to be around 1000rpm (see Figure 5.20) [74].

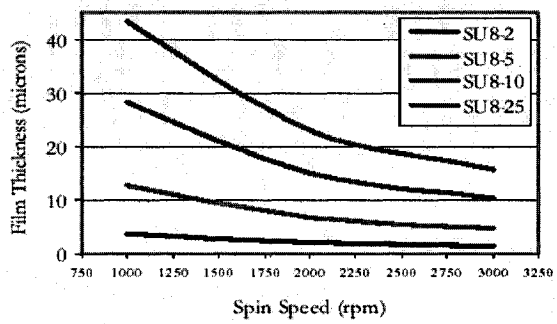

Figure 5.20 Spin-speed vs. thickness curves for the specified SU-8 resist formulations [74]

This was used as the starting point to determine the exact spin-speed needed to produce 47μm thick film. Static dispense, as the preferred method of viscous resist application was used. As a rule of thumb 1mL of SU8 per inch diameter of the wafer to be coated was dispensed. For tighter Teflon tube this process took 20sec for a maximum pressure of 60psi. After dispense, the speed was ramped to 500rpm at 100rpm/sec increments (5sec) followed by 300rpm/sec increments to the final spin speed which was held for 30sec. It should be noted that for lower spin-speeds (<1000rpm) longer spin time might be needed

to obtain more uniform films. As direct optical metrology such as spectroscopic ellipsometer cannot be used for measurement of very thick films, a different method had to be employed. To measure the film thickness, prior to resist spin-coating, a piece of adhesive tape was placed on several places on the wafer. The resist was then deposited and softbaked, followed by the removal of the tape from the wafer and Tencor profiler instrument was used to measure the height difference. However this method was later found to give misleading results, as 'edge-bead' effect would form around the tape yielding large film non-uniformities across the wafer. For exact determination of the film thickness, complete film processing was carried out including softbake, exposure, PEB and development and the difference in topography of the fabricated features, was measured using profilometer. To obtain accurate thickness measurement, careful manipulation of the instrument was required. It was found that insufficient stylus force would prevent the tip of the stylus to reach the bottom of the structures thus yielding lower thickness reading. However, too strong a force would cause the stylus tip to penetrate the soft SU8 structures which would not only give an incorrect reading, but could also damage the tool. Optimum force depended strongly on the length of the scan and calibration was often needed to determine the required input parameters to obtain exact thickness measurement (for 2mm scan length, 10mg force and 50μm/sec scan speed was found to yield correct measurements for SU8 film as verified using SEM). The exact spin-speed for 47um thick film was found to be 1300rpm with film uniformity of +/-3%. The results of the measurements are summarized in Figure 5.21.

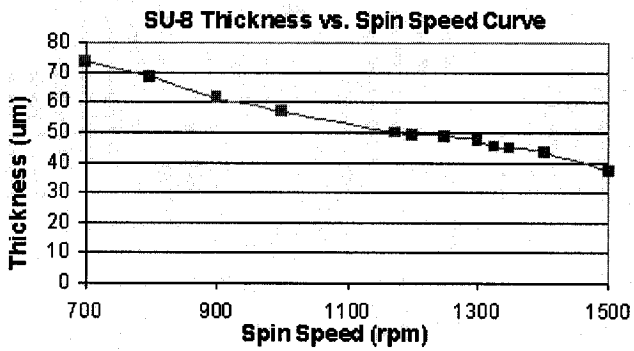

Figure 5.21 Experimental spin-speed vs. thickness curve for SU8-25

SU8 process parameters were hence developed for resist thickness of 47μm. It should be noted that the solvent content was a critical factor in the determination of all the process

variables, which might explain discrepancies with values found in literature [67,68]. Also, given several process variables to be optimized, large process latitude was employed to find processing parameters that yielded best results, and the process optimization was then carried out around those values. The basis for parameter evaluation included quality of the patterned film (adhesion and crack-free structures), resolution and sidewall profile and was assessed out using an optical microscope and HITACHI 6700 SEM.

4. Pre-exposure bake

Pre-exposure bake (PB) was performed using a hot plate with a nominal temperature of 95°C. This step was needed to evaporate the solvent content from the deposited film and depending on the PB time, the subsequent processing steps will need to be adjusted [68]. Specifically, the longer the softbake time, the longer exposures will be required in order to crosslink the exposed SU8. The bake times were varied from 15 to 35 minutes. The optimum time that yielded best adhesion and resolution was found to be 20min. Furthermore, it was found that by including a 5min bake at 65°C, stress-induced cracks both, at the corners of the developed SU8 structures and those in PMMA undercladding layer can be eliminated. Hence, for the final device production, this step has been included. The wafer was placed on a hot-plate at room temperature and the temperature was then increased to 65°C at 8°C/min and held at 65°C for 5min. Then, the temperature was further increased to 95°C at the same ramp rate, and held for 20min. Finally to further reduce stress, the temperature was ramped back to room temperature at 10°C/min. After softbake the wafer was left to relax at room temperature for 15 minutes before exposure.

3. Exposure

The exposure was performed on a broadband UV EVG-620 mask aligner using the intensity measured at 365nm-spectrum line (in mW/cm^2) to calculate the exposure dose (mJ/cm^2) depending on the exposure time (s). For this purpose, Lutron UVA-365 bandpass (320-390nm) lamp meter with peak at 365nm was used. An Omega optical filter (PL-360LP) [92] that filters out all the light below 360nm was used during exposure to ensure straight sidewalls and improved resolution, since excessive exposure to wavelengths below 350nm will cause an exaggerated negative sloping sidewall problem

commonly referred to as 'T-topping' [74]. Exposures performed in contact and small gap proximity (1μm) showed similar results [75], hence proximity printing was used in process optimization in order to minimize mask degradation associated with contact lithography. Note that hard-contact was employed in several preliminary experiments, which resulted in SU8 film sticking to the mask, especially at the chrome edges, that could later only be removed by placing the mask in piranha solution for 10min. Since piranha slowly etches chrome, doing this often is not recommended and for the remaining experiments, proximity was used. The exposure was divided in 10-15sec intervals with 60sec waiting time in between. This was done to prevent the formation of the thin solid crust that is often observed when dealing with the thick layer of photoresist. This crust causes a loss of resolution, due to the heating of the surface induced by high dose (>200mJ/cm^2) and long exposure time. The recommended exposure dose obtained from the manufacturer's datasheet for 47μm thick film varies between 200 and 400 mJ/cm^2(see Figure 5.22) and this was used as the starting point.

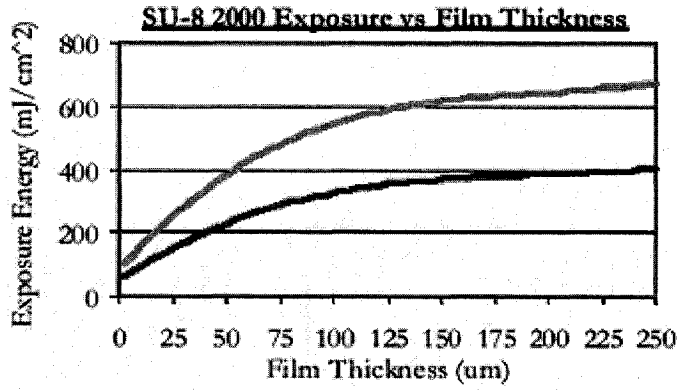

Figure 5.22 Recommended exposure dose processes [74]

The exposure dose was varied between 280mJ/cm^2 and 968mJ/cm^2. It was found that catastrophic adhesion failure and excessive cracking occurred for exposures below 450mJ/cm^2 (see Figure 5.23(a,b,c,e)).

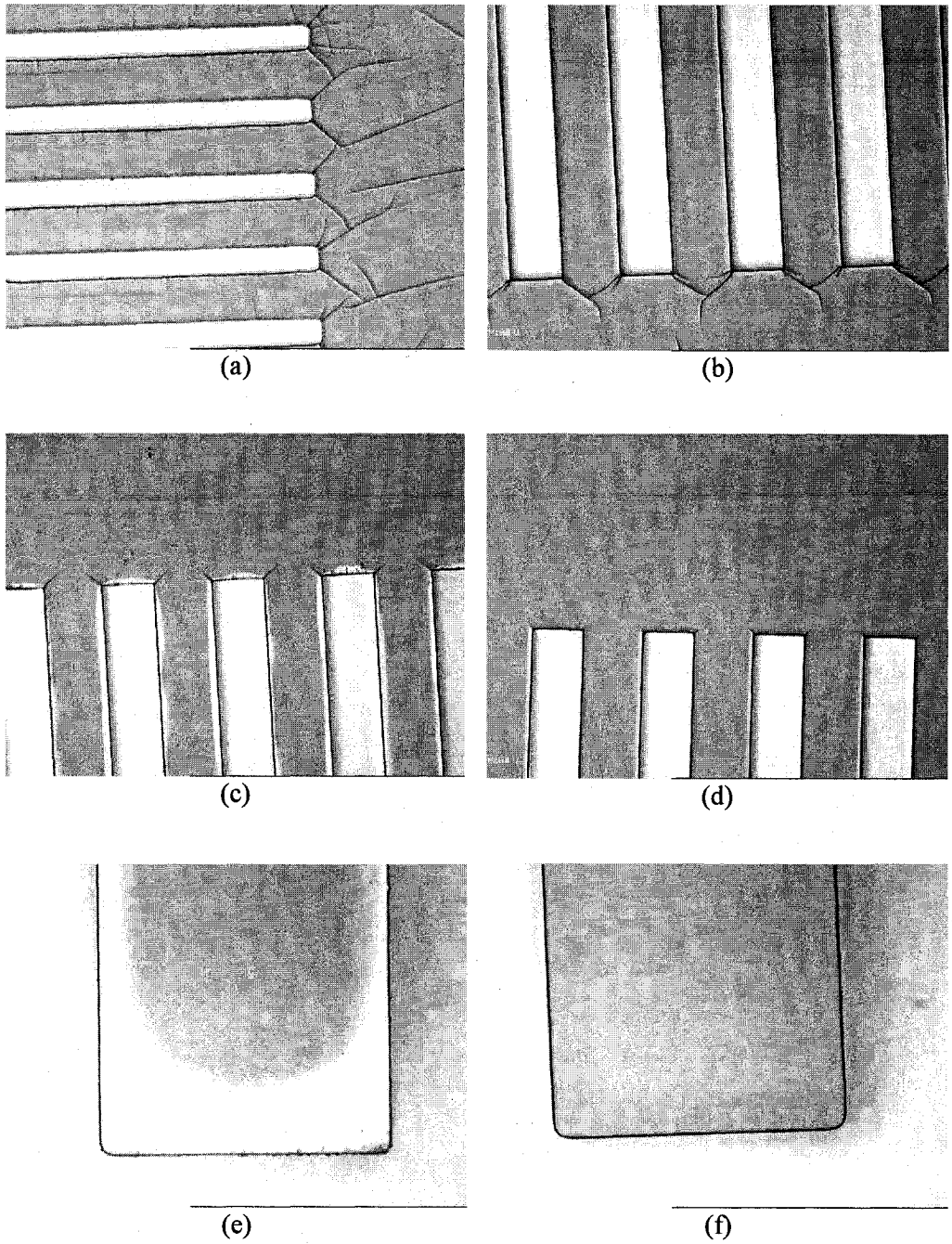

Figure 5.23 SU-8 cracking and delamination is highest for lower exposure doses and these problems decrease as exposure dose increases for same pre-bake, post-exposure bake and development times (a)323mJ/cm^2; (b,e)420mJ/cm^2; (c)535mJ/cm^2; (d,f)676mJ/cm^2

This indicated an under-crosslinking condition and to correct the problem, either exposure dose or PEB time needed to be increased. Both were tried, and it was found that increasing the exposure dose gave better resolution results (Figure 5.23(d, f)) since very long PEB times tended to distort fine lines and space resolution, as the unexposed region

of the film puckered and then relaxed, while the exposed pattern was unaffected [67]. However, excessive exposure was also found to have an adverse effect on the resolution, producing rough sidewalls and rounded corners. This occurred for exposure doses exceeding 950mJ/cm^2 (see Figure 5.24).

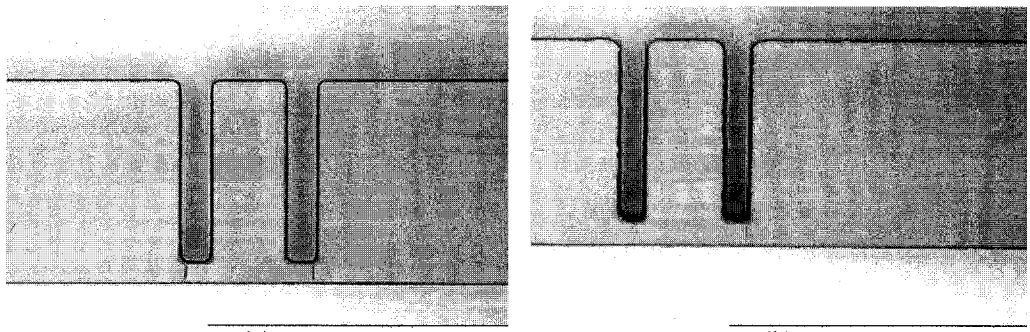

Figure 5.24 Resolution and sidewall smoothness for exposure dose of (a)676mJ/cm^2 and (b)968mJ/cm^2 with other processing parameters left unchanged

In addition to this, it was found that excessive exposure degraded the optical quality of the exposed film (yellowing of the film), which would lead to increased absorption losses in the waveguide core. The optimum exposure dose was found to be 676mJ/cm^2 for the corresponding optimum pre-bake and post-exposure bake times. The vertical sidewall profile was obtained for this exposure and sidewalls were smooth (see Figure 5.25). It should be noted that this exposure dose was primarily chosen as to eliminate the cracks that were occurring in the SU8 film especially at sharp edges (the corners of the waveguides) and PEB was then tailored to produce vertical sidewall slope.

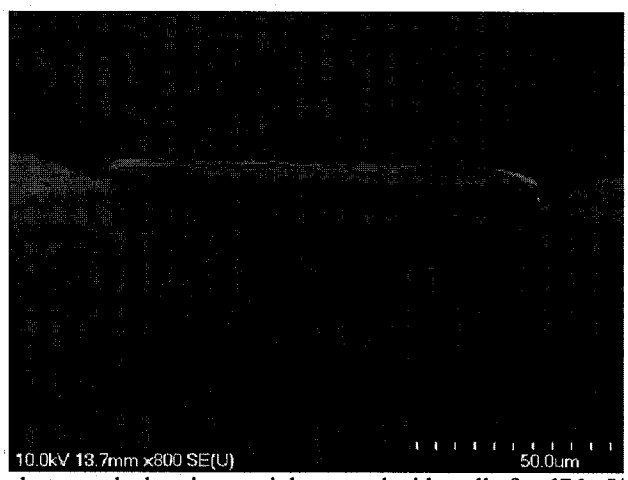

Figure 5.25 SEM photograph showing straight smooth sidewalls for 676mJ/cm^2 exposure dose

For SU8 on PMMA-coated substrate, this exposure those was insufficient as cracks appeared not only at the corners of the SU8 structures but also on the PMMA lower cladding layer all around the SU8 patterns. The crack propagation (Figure 5.26a) indicated undercrosslinking of thick SU8 near the PMMA, which then caused overetching in the bottom layer, exposing the PMMA to added stress. Increasing the exposure dose to 800mJ/cm^2 alleviated this problem (Figure 5.26b).

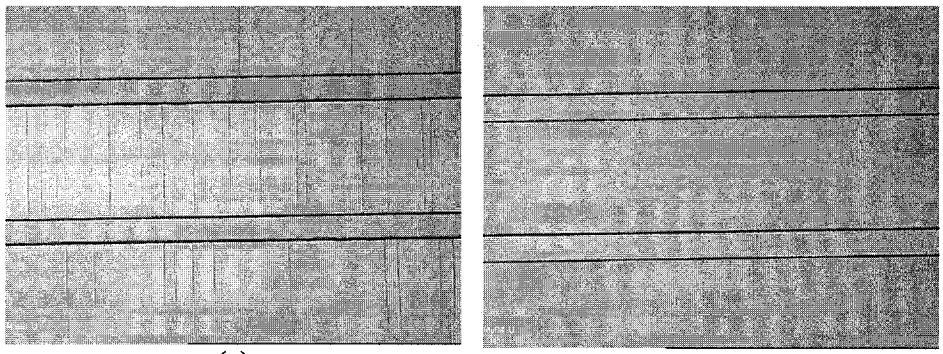

(a) (b)

Figure 5.26 Results of the SU8 exposure dose adjustment to eliminate the cracks in PMMA (a)676mJ/cm^2; (b)800mJ/cm^2

After exposure the wafer was left to relax at room temperature for 15 minutes before PEB.

5. Post-exposure bake

Post-exposure bake was performed using a hot plate with nominal temperature of 95°C, to selectively cross-link the exposed portions of the film. The optimum PEB time depended on the exposure dose, since the lower the exposure dose, the longer will the PEB time be required to fully cross-link the exposed regions. Therefore PEB times ranging from 15min to 110min were explored depending on the previous exposure dose. However, as outlined in the previous section, very long PEB times tended to distort fine lines and space resolution, which was avoided in final device production. Optimum PEB time for the corresponding exposure and softbake times was found to be 15min. To minimize stress, wafer bowing and resist cracking, a slow ramp was included in the same manner as it was used for the softbake. After PEB the wafer was left to relax at room temperature for 15 minutes before developing.

6. Develop

Developing was found to play an important role in the film adhesion. Extended developing time may increase the chance of delamination of the SU8 exposed area from the substrate, and also etching of the PMMA cladding layer (Figure 5.27), but insufficient time may negatively reflect on the lithographic resolution [76].

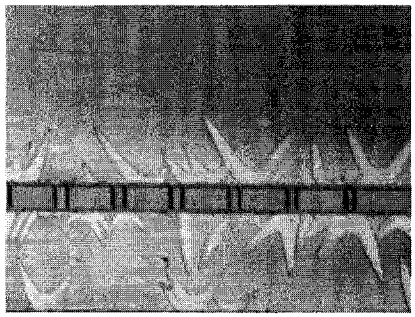

Figure 5.27 Effect of 10min immersion in PGMEA of SU8 patterned core on PMMA lower cladding; color change indicates etching of PMMA

SU8 was developed by wafer immersion in the same solvent used to dilute the original epoxy resin, PGMEA (propylene glycol methyl ether acetate). Agitation was employed to decrease the developing time. Ultrasonic agitation was explored for several experiments, however this caused the SU8 structures to lift-off and float away from the wafer. Therefore, less aggressive, manual stirring of the developer solution was employed instead. It should be noted that developing time largely depends on the solvent concentration, and if several wafers are developed in the same solution, increased time may be needed for successive wafer processes. To determine the time needed to fully develop SU8, the wafers were placed in the PGMEA and the immersion was timed. Then the developed wafers were rinsed with Isopropyl Alcohol (IPA) which caused formation of white residue for underdeveloped film. The wafer would be placed again in the PGMEA for 1min and rinsing was repeated. This process was repeated until no white residue could be seen. Optimum develop time in fresh developer was found to be 5min when manual stirring of the solution was employed.

7. Rinse and dry

As no ideal rinsing/drying process has yet been reported for SU8, several different techniques were tried [77]. First, as a rinse, a final dip in a fresh bath of PGMEA was used to rinse away any SU8 residue that remains on the wafer. The top wafer surface was

then dried using nitrogen gun. This caused streaking of the PGMEA solution resulting in dark lines on the wafer surface (see Figure 5.28).

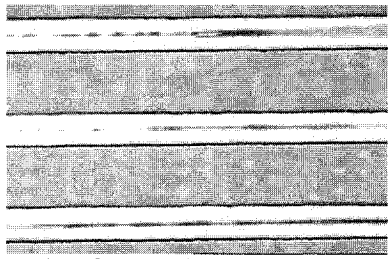

Figure 5.28 Image of dark lines on Si wafer resulting from PGMEA solution when blow-dried with N_2

This method was also found to cause delamination of the patterned structures due to high pressure exerted on the structures during nitrogen flow. Hence drying from the back of the wafer was tried. This however was inefficient since very long time was required to completely dry the wafer and some residue still remained around the developed structures. To decrease the time required to dry the wafers, rinse with IPA was explored. This method, while significantly reducing the dry time, was found to be the worst in terms of residue. Not only that the residue formed around the edges of the structures, but it also stuck at the top of the patterns and this residue could not be removed afterwards by repeated IPA rinse or PGMEA dip (see Figure 5.29).

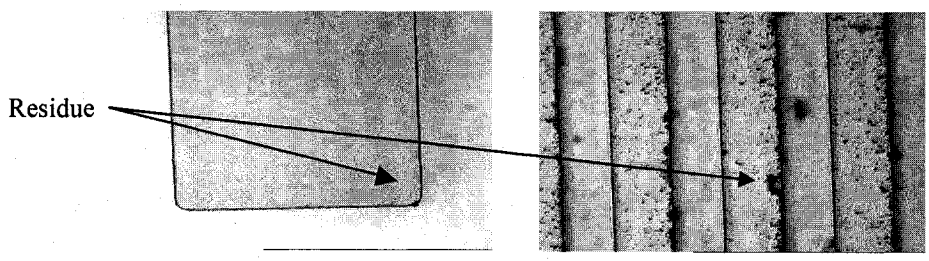

Figure 5.29 Image of the residue remaining from IPA rinse and blow dry of SU8 on Si and SU8 on PMMA-coated Si substrate

Finally, to resolve this problem, three-step rinse and spin-dry was employed. First the wafer was dipped in a fresh solution of PGMEA for 10 sec, taken out of the solution and placed on the wafer chuck of Bidtec R&D Spinner. It was then flooded with PGMEA solution at low spin speed, followed by fast ramp to 3000rpm, which was held for 30sec to complete the drying process. No residue was observed for this procedure and hence this was used for the final device fabrication (see Figure 5.30).

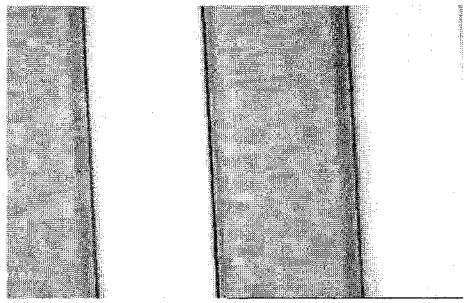

Figure 5.30 No residue remains when spin-drying after PGMEA rinse is employed

The complete optimized process for 47μm thick SU8 structures with 90° corners and sidewall slope is summarized in the table below.

Process Parameter	Parameter Steps
Wafer preparation	- Piranha clean (sulfuric acid and hydrogen peroxide in 3:1ratio) - DI water rinse - Dehydration oven bake at 200°C for 30min
SU8 deposition	- Dispense static 6mL for 6" substrate - Ramp to 500rpm at 100rpm/sec - Ramp to 1300rpm at 300rpm/sec and hold for 30 sec
Prebake (hotplate)	- 25°C to 65°C at 8°C/min - 65°C for 5 min - 65°C to 95°C at 8°C/min - 95°C for 20min - 95°C to 25°C at 10°C/min
Expose	- 676mJ/cm^2 on Si and 800mJ/cm^2 on PMMA coated substrate divided in 9-10s exposure intervals with 60sec wait - 1μm proximity
Post-exposure bake	- 25°C to 65°C at 8°C/min - 65°C for 5 min - 65°C to 95°C at 8°C/min - 95°C for 15min - 95°C to 25°C at 10°C/min
Develop	- 5min in fresh PGMEA, manual stirring
Rinse	- 10sec immersion in fresh PGMEA solution - Place on spinner and flood with PGMEA - Spin dry at 3000rpm for 30 sec

Table 5.6 SU8-25 processing recipe for 47μm thick film

5.7 PMMA RIE

From the process flow, after core deposition and patterning, PMMA upper cladding layer is deposited and patterned in the same manner as the lower cladding. After this, the PMMA etch is required to release the V-grooves and the microchannel by removing the cladding layers everywhere outside the waveguide area. Reactive ion etching (RIE) is chosen for this purpose. RIE enables profile control due to synergetic combination of

physical sputtering with the chemical activity of reactive species with a high etch rate and high selectivity [22]. The etch yield Y(E) for both physical and chemical mechanisms involved can be described by the following expression:

$$Y(E) = A(E_i^{1/2} - E_{th}^{1/2}) \quad (1)$$

where E_i is the ion energy, A is constant representing the slope and E_{th} is the threshold energy of etching. The magnitude of E_i has been shown to be directly proportional to the applied RF power, responsible for induced dc bias voltage at the cathode [80]. Besides ion energy which provides the necessary activation and controls the degree of anisotropy, ion and neutral atom concentrations also control the etch rate in a plasma reactor [22]. For high anisotropy, low pressure is required ($<10^{-2}$Torr) so that positive ions strike the surface at normal incidence, but at very low pressures, physical sputtering dominates where ion density drops off quickly causing a lower etch rate. Then to increase the etch rate, the power of wafer bias should be increased which in turns makes the remaining ions more energetic. Therefore, pressure and RF power play a crucial role in control of etch rate and quality of the etched structures and their effect has been explored in the following section. The process development for Al hard mask used for RIE etch of PMMA is described first, followed by the PMMA RIE process development.

5.7.1 Al hard mask deposition and etching

For patterning of the PMMA film using RIE etch, hard mask is required. For this purpose sputtered Al film was chosen for the reasons described in Chapter 3. The complete process for the formation of Al hard mask is described in details below.

Al Sputtering

The sputtering was performed using MRC 603-III DC sputter system. To develop an appropriate recipe for Al deposition, a standard recipe to sputter 500nm thick Al film was used as a starting point. The vacuum level for this deposition was set at 5E-6 Torr, the speed of moving target was set at 7.5cm/sec, the RF power was set at 1.1kW and the pressure was at 10mTorr. To measure the thickness of the deposited Al film, a blank Si wafer was used with circular tape positioned at several places on the wafer to keep those parts of the wafer clear and enable easy measurement of the thickness by removing the

tape after deposition and measuring the difference in height using the profiler. The thickness of the sputtered film was uniform across the wafer and measured to be 497nm.

Al PAN Etch

According to this thickness and the reported manufacturer's Al etch rate in PAN etch solution (10nm/sec at 50°C) indicates that 50sec should be sufficient to remove the required 500nm of Al. To determine the actual etch rate, a blank Si wafer with deposited 500nm of Al was used. Al etchant type A from Transene (PAN etch: $80\%H_3PO_4$ + $5\%HNO_3$ + $5\%HA_c$ + $10\%H_2O$) was poured in a Pyrex beaker and placed on a programmable hot plate with attached temperature probe that serves as a thermostatic controller, set to 50°C. The solution was stirred with magnetic stir bar set to 200rpm, and the wafer was placed inside the beaker once the temperature has stabilized to 50°C. After 50 sec of etch, the wafer was taken out of the PAN etch and rinsed. The remaining thickness as measured with the profilometer was 298nm. The actual etch rate for Al film with no patterns was thus found to be 4nm/sec, and the time required to remove all the film was 2min 5sec.

Al deposition on PMMA coated wafer

Four blank Si wafers were cleaned and used to deposit 5μm thick PMMA layer (see section 5.5). Following the PMMA cure, these wafers were then used to sputter 500nm thick Al film using the above recipe. To verify the sputtered film quality with each PMMA wafer, a blank Si wafer was placed on the plate next to it. In addition, a tape test was conducted after the metal deposition as a preliminary check to see if the metal will adhere to the substrate and not be removed during subsequent etches [79]. First Al on PMMA wafer came out with bubbles created in the Al film, while the Al film on blank Si wafer was of good quality and passed the tape-test. This indicated that the temperature of the process possibly exceeded the PMMA glass transition temperature and that Al was bubbling and breaking during PMMA reflow due to solvent evaporation underneath it (see Figure 5.31).

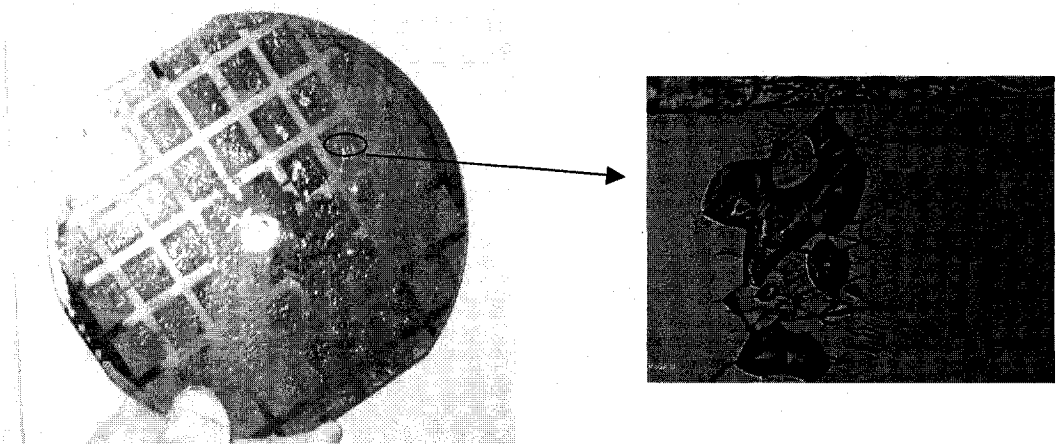

Figure 5.31 Al bubbling and cracking during PMMA reflow (T>105°C) captured by a digital camera and 20x microscope magnification

For the next wafer in process, a temperature sensor was placed on the back and the same recipe was run. The temperature was measured to exceed 132°C which was well above the PMMA Tg of 105°C. To control the temperature below PMMA Tg, the speed of moving target was decreased to 15cm/min, meaning that the thickness of the sputtered film would be reduced to half, i.e. 250nm. The temperature at this speed was measured to be below 88°C, however the Al film on PMMA coated wafer was still not of good quality. Compared to the blank Si wafer, the film was cloudy, non-reflective, and did not pass the tape-test, which indicated that there was an adhesion problem between Al and PMMA, caused by PMMA outgasing. This low quality film, besides being a poor mask for subsequent PMMA RIE etch, also proved difficult to pattern. To solve this problem, additional time was taken to put system in high vacuum, where the vacuum level was set to 6E-7 Torr. The resulting Al film on the PMMA coated wafer was of very high quality, mirror-like, identical to that deposited on the blank Si wafer. This Al deposition recipe is summarized in table below.

Parameter	**Value**
Target moving speed	15cm/min
RF Power	1.1kW
Pressure	10MTorr
Vacuum level	6E-7
Resulting thickness	250nm

Table 5.7 Al deposition parameters

The next step in the process development required photolithography to define the patterns in Al hard mask (section 5.4.1). The patterned resist served as a mask for Al PAN etch which is highly selective to Al. Following the photolithography, Al was timed-etched for 62sec in constantly stirred PAN etch at 50°C to reduce undercut. The wafers were then rinsed in DI water and dried using nitrogen. The obtained Al pattern showed smooth sidewalls with approximately 60° slope (Figure 5.32), typical for isotropic etchants.

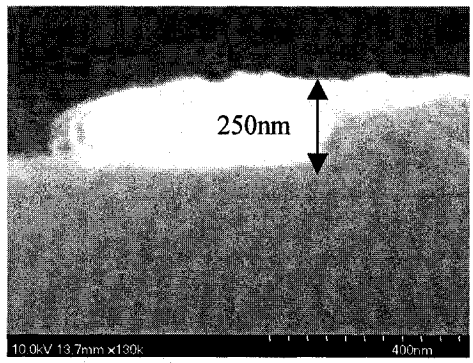

Figure 5.32 SEM Image of patterned Al film

Several wafers were submitted to the above process to be used in determining of optimum PMMA RIE etch conditions described below.

5.7.2 PMMA RIE process development

To remove the PMMA cladding layers everywhere outside the waveguide area, dry etching was performed in a commercial Applied Materials P5000 RIE system with O_2/Ar as etching gases. It has been previously reported that PMMA etched in O_2 (10sccm)/Ar(40sccm) produces a smooth and vertical sidewall with etch rates of 0.3μm/min and 0.37μm/min at RF powers of 30W and 40W respectively and 30mTorr chamber pressure[80]. This was used as a starting point to determine the actual etch rate for P5000 RIE system, however the chamber pressure was kept at 150mTorr to prevent the domination of physical sputtering over chemical activity and keep the benefits of synergy. A blank Si wafer coated with 4.4μm thick PMMA was used for this purpose. The thickness of the film was measured after etch using Promatrix Film Thickness Map system. The etch process created consisted of two steps. First step was intended for system stabilization and not the actual etch, hence the RF power was set to 0W and the O_2:Ar gas flow ratio to 10:40 sccm. The second step was the actual etch carried out for

120sec with the RF power increased to 40W and other parameters left unchanged. The etch rate for these parameters was found to be 0.12μm/min, more than three times lower than the reported value [80]. This etch rate was not satisfactory as it would require 83min to etch 10μm thick PMMA layers. To increase the etch rate, RF power was increased gradually and the temperature was monitored using temperature sensor to prevent overheating of the 6" wafer and smaller cleaved wafer samples at the temperatures above the PMMA Tg. It was found that for 6" wafers the upper temperature limit was reached at powers above 300W, while for the wafer samples this limit was lower, at powers above 150W. The etch rate of PMMA was hence measured as a function of RF power varying from 40 to 300 W for 6" wafers, while keeping the O_2:Ar gas flow ratio constant at 40:160 sccm. To investigate the effect of the gas flow ratio on the etch rate, a series of experiments also included varying the ratios of the O_2/Ar mixture while keeping the power constant at 100W. The results are summarized in Figures 5.33 and 5.34.
In figure 5.33, a least squares fit of equation (1) to the data shows that the etch rate

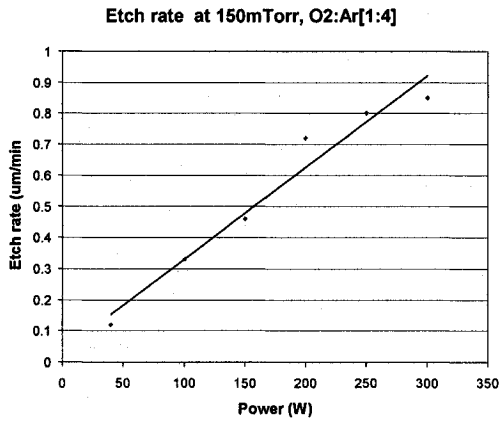

Figure 5.33 Etch rate versus power, O_2:Ar=40:160sccm, Pressure=150mTorr

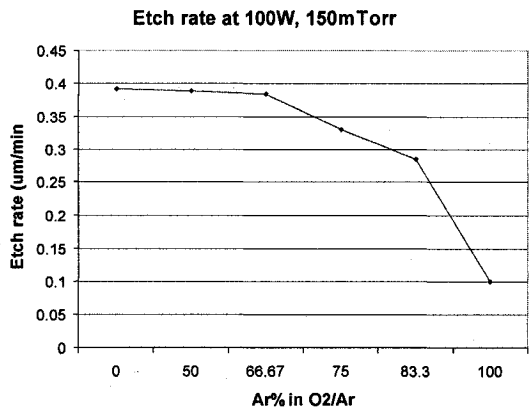

Figure 5.34 Etch rate versus proportion of Ar in O_2/Ar Plasma, Power=100W, Pressure=150mTorr

increases linearly as a function of applied RF power, as expected [80]. The dependence of etch rate on the proportion of Ar in O_2/Ar gas mixture with total flow rate held constant at 200sccm, RF power of 100W and chamber pressure of 150mTorr has been plotted in Figure 5.34. The plot shows that the etch rate decreased with the decreasing proportion of reactive O_2 in the plasma. This was expected, since etching in O_2 plasma is attributed to dissociation into O radicals accompanied by the formation of volatile etch products of CO, CO_2 and H_2O. Hence decrease in the flow rate, decreases supply of radicals for

potential reaction. After determining the etch rates, an investigation of the effect of gas flow ratio on the surface morphology of PMMA after etching was conducted. For this purpose, small Si wafer samples with coated PMMA film and patterned Al mask were used. Ratios of the O_2:Ar mixture were varied (1:0, 1:1, 1:2, 1:3, 1:4 and 1:5) while keeping the overall gas flow constant at 200sccm, power constant at 150W and pressure at 150mTorr. The microstructures were examined using SEM, the results of which are shown in Figure 5.35 for three different ratios.

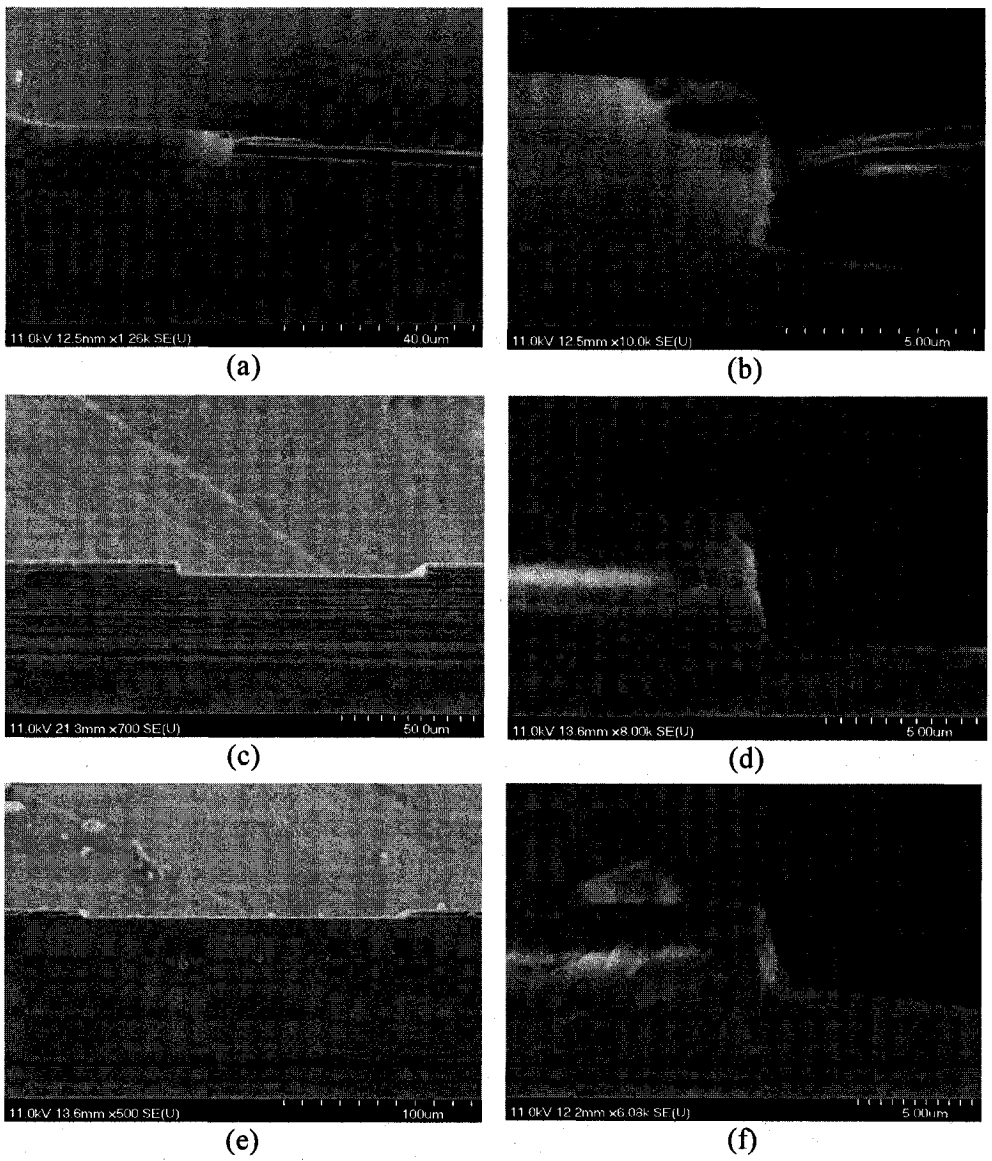

Figure 5.35 PMMA RIE using different O_2/Ar gas flow ratios at a power of 150W and pressure of 150mTorr (a,b)1:3; (c,d)1:4; (e,f)1:5

From Figures 5.35(b), and 5.35(f), it can be seen that higher oxygen flow results in PMMA overetching with undercut, while lower oxygen flow results in PMMA underetching and non-vertical sidewall profile respectively. The best results in terms of sidewall smoothness and verticality were produced for O_2:Ar gas flow ratio of 1:4 (40:160 sccm) (Figure 5.35(d)). This gas flow ratio was thus used in 6" wafer device processing. The actual power used for device fabrication was 200W which gave lower etch rate that the 300W limit, however the higher temperature associated with higher power generally leads to rougher surface so a compromise was made [22]. Process program is summarized in the table below.

Parameter	**Step 1**	**Step 2**
Pressure (mTorr)	150	150
RF Power (W)	0	200
Ar flow (sccm)	160	160
O_2 flow (sccm)	40	40
Time (sec)	15 sec	N/A
Etch Rate (um/min)	Assumed 0	0.72

Table 5.8 PMMA RIE etching parameters

6 Process flow steps integration

Having each individual fabrication process developed, the next step comprised of their integration into a complete process flow. This chapter describes the issues encountered during process flow integration, and the needed adjustments for the final device production. The fabrication results are shown throughout the sections 6.1-6.3, including a motivation for the revised device design. Section 6.4 describes the bonding procedure development. Finally, the fabrication of the alternative device is presented in section 6.5.

6.1 Silicon wafer patterning

6.1.1 DRIE Etch

The first step in the process flow required DRIE etching of the central waveguide/microchannel trench in silicon substrate. As mentioned previously, this step included patterning 2μm thick positive S1813 photoresist (PR) (section 5.3) which served as the mask for the DRIE. Etching was carried out at Cornell University. The processed wafers were inspected using profilometer and the depth of the etched structures was found to be 57μm +/- 1.8%. To prepare the wafers for the next step, the remaining photoresist was ashed using Tegal O_2 plasma system for 40min at 0.7mTorr pressure and 300mW power. After ashing, the wafers were treated in Piranha solution for 15 minutes.

6.1.2. TMAH Etch

Cleaned wafers were then pushed in Tylan furnace for 1hour at 1150°C to grow 0.8μm of wet thermal oxide which served as a mask for wet TMAH etching of V-grooves in silicon substrate. The next step was photolithography to define the patterns in the oxide film. For this purpose 1.4μm of positive S1813 PR was spin-coated onto the wafer and prebaked (section 5.3). The wafer was then aligned with the mask and exposed with nominal 70mW/cm^2. The exposed resist was developed and postbaked. The obtained patterns were then inspected using Nikon optical microscope. It was found that the exposed resist did not etch completely in the area that is immediate to one side of the trench (Figure 6.1(a)) leaving a strip of resist across all of the V-groove patterns, which would then prevent complete silicon etching of the V-grooves entering the channel.

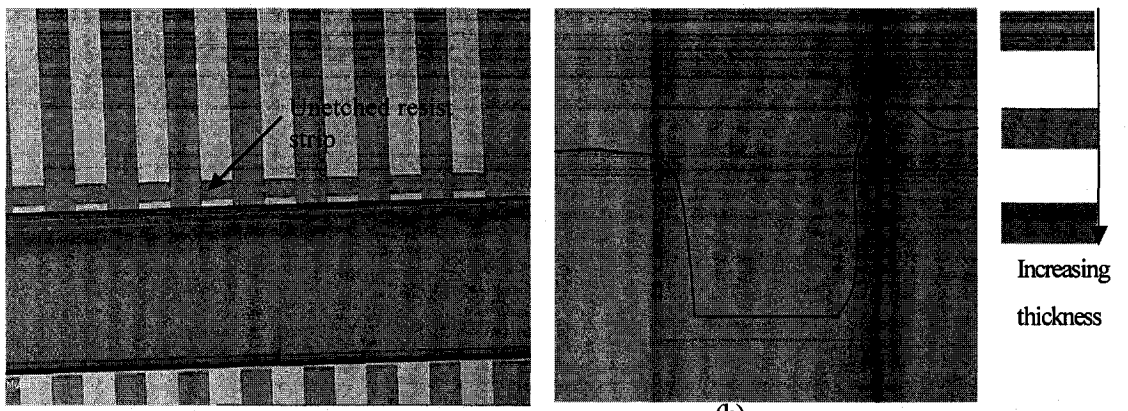

Figure 6.1 (a)Underetch of the resist near the trench leaving the strip across the V-grooves; (b)Spin-coated resist thickness variation inside and outside of the trench (left-thin resist; right-thick resist; dashed line-topography; full line-resultant resist thickness using spin coating on topography)

The cause of this problem was the uneven resist film deposition (uniformity>56%), resulting from the spin-coating process on a wafer with topography. The etched trenches impeded or prevented the smooth flow of resist from the center to the edge of the wafer during spin cycle, causing the resist to form pools inside the trench. This resulted in "shadows" [81] of thin resist coverage on the side of the feature opposite the center of the wafer. Additionally, a surface-tension effect at the edges of the features resulted in increased film thickness at the edges closest to the center of the wafer, as can be seen in the variation of resist color at these two edges (Figure 6.1(b)). Then during the exposure, the thicker resist was not fully exposed near the surface of the substrate, creating the strip obstructing the V-groove pattern during development. The best way to alleviate this problem would be to use spray-coating process [81,82] for photoresist deposition, however, the required equipment was unavailable at the time. Instead, a modified PR deposition program and a modified exposure dose were used. In addition to this, the process flow steps for silicon patterning were inversed for one processed wafer in an attempt to alleviate this problem.

1. Deposition

First, the photoresist was flooded onto the wafer, in order to cover the whole surface. A 30sec pause was introduced after the dispense step, allowing additional time for the solution to flow into the trenches. Next, a slow acceleration and spin speed (500rpm) was applied for 15sec, allowing enough time for the solution to flow and spread prior to drying. Then, a second step with a fast spin speed promoted the drying of the film and

reduced the further flowing of photoresist that would cause non-uniform coating. Using this program, the uniformity of photoresist was found to be between 10-20% [82], which was better compared to the previous program.

2. Exposure

Even with the modified deposition program, the resist strip across V-grooves pattern was not eliminated for all the devices. Therefore, it has been decided to overexpose the resist, using a dose of 200mJ/cm^2, which was sufficient to expose the thicker resist film at the edge of the trench and create the desired pattern (Figure 6.2) for all the devices.

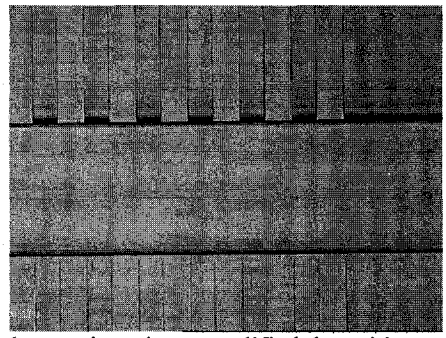

Figure 6.2 V-groove pattern in photoresist using a modified deposition program and higher exposure dose

The overexposure however had an adverse effect on the thinner resist film. The overexposed region containing the thin resist caused resist overetching, which transferred during subsequent fabrication procedures: oxide RIE and TMAH etch of silicon. The final product resulted in overetched grooves on one side of the device (Figure 6.3).

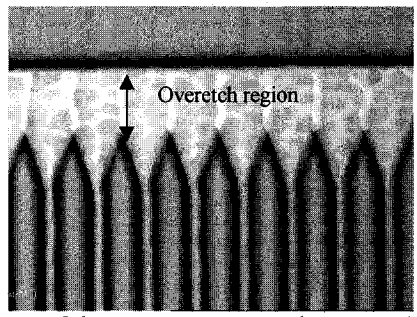

Figure 6.3 Image of the V-groove overetch next to the channel wall

Given a short length of the overetch (200μm), this should not create the problems during fiber insertion, as the overall length of well defined grooves (4800μm) should be sufficient to confine the fiber and keep it in place, aligned with the waveguides. However, this issue has been a major motivator for development of the alternative device design, as described in section 6.5.

3. Process Flow Steps Inversion

Finally, another way to alleviate the above problem was explored. The process steps used in Silicon wafer patterning were inversed. Namely, first the V-grooves were etched in silicon wafer (section 5.4) and then the DRIE process was used to etch the central waveguide trench. Instead of photoresist mask previously used for the DRIE, thermally grown oxide was patterned and used as a more stable mask, in the same manner as for the TMAH etch. This resulted in perfect translation of the V-grooves and on both sides of the etched trench (Figure 6.4).

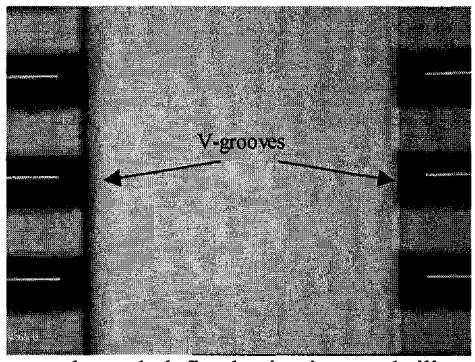

Figure 6.4 V-grooves and trench defined using inversed silicon patterning process

Hence the problem inherent to spin-coating process has been eliminated using two different techniques, allowing further process integration.

6.2 Waveguide fabrication

After silicon wafer patterning, the waveguide fabrication has proceeded as outlined in sections 5.5 and 5.6. First a PMMA lower cladding was deposited and baked. During the anneal cycle, PMMA reflowed thus creating a fairly uniform coat across the wafer. Next, SU8 core was deposited and patterned inside the silicon trench. Finally, PMMA upper cladding was deposited and cured in the same manner as the lower cladding. This step required a slight modification, where the final ramp-up temperature has been reduced to 135°C (instead of 180°C), in order to minimize the thermal degradation of the SU8 affecting the optical properties of the patterned core layer commonly associated with high temperature hard-bakes [35]. To compensate for the temperature reduction, the bake time was increased to 5hrs, opposed to 3hrs used for lower cladding, resulting in a, uniform, crack-free film. However, this last step has introduced another problem. During the

PMMA upper cladding cure, some devices experienced SU8 structures deforming, shifting, and sticking to the middle of the trench (Figure 6.5).

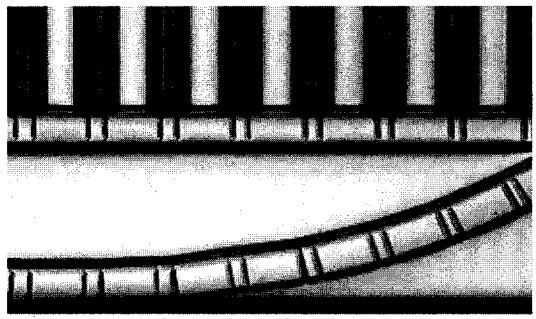

Figure 6.5 SU8 structure deformation after the PMMA upper cladding anneal

This problem has been contributed to the curing and reflow of the PMMA cladding layer deposited in the V-groove area and underneath the SU8 pattern. Since the lower cladding consisted of cured but uncrosslinked PMMA film, this layer tended to reflow at temperatures above the PMMA Tg (105°C). As the PMMA flowed from the overetched V-groove area into the channel, it caused the moving of the SU8 film that was patterned next to it. The typical device yield after this process step was found to be between 60 and 70%. For 100% yield, curing would need to be performed at lower temperature for a longer time, however this was not explored, as the device yield was found to be satisfactory for our purpose. The fabricated waveguides inside the silicon trench, aligned with the V-grooves for successful dies are shown in Figure 6.6. As can be seen in Figure 6.6, the fabricated waveguides are perfectly aligned to the V-grooves.

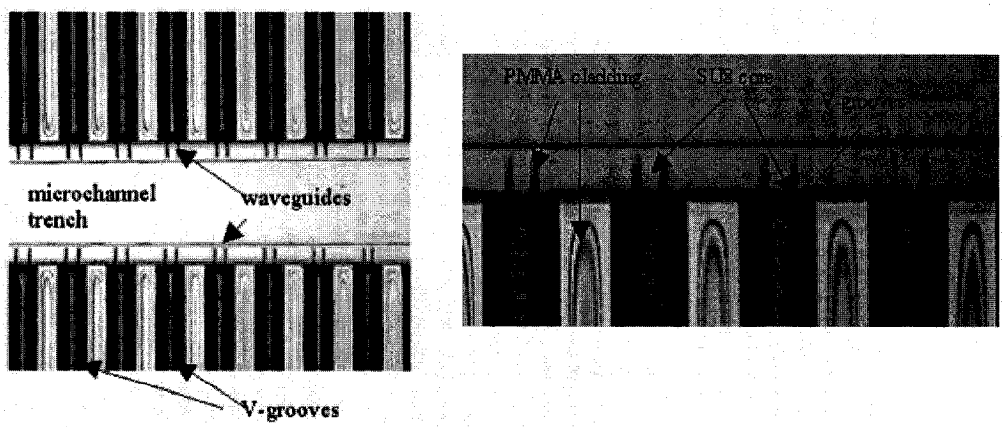

Figure 6.6 Waveguide fabrication process integration (image of the wafer with inversed silicon patterning steps shown)

The next step in the process flow required the removal of the PMMA cladding layer everywhere outside the waveguide area to define the microchannel and allow planar device surface for bonding purposes.

6.3 Channel formation process

For the RIE of PMMA cladding everywhere outside the V-grooves, 250nm of Al film was sputtered to serve as a hard mask (section 5.7.1). Conformal coating was achieved as shown in Figure 6.7.

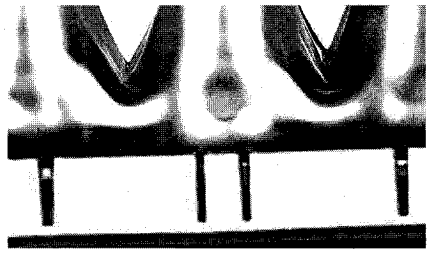

Figure 6.7 Al film deposition resulting in conformal coating

Next, photolithography was performed to define the pattern in Al mask. The same problem of non-uniform resist thickness previously encountered, inherent to spin-coating process was anticipated for this step. For this reason, modified spin-coating program was used which helped obtain the desired pattern for most of the devices (Figure 6.8(a)). However, a small fraction of devices experienced overetching of the resist, which translated in Al overetch (Figure 6.8(b)).

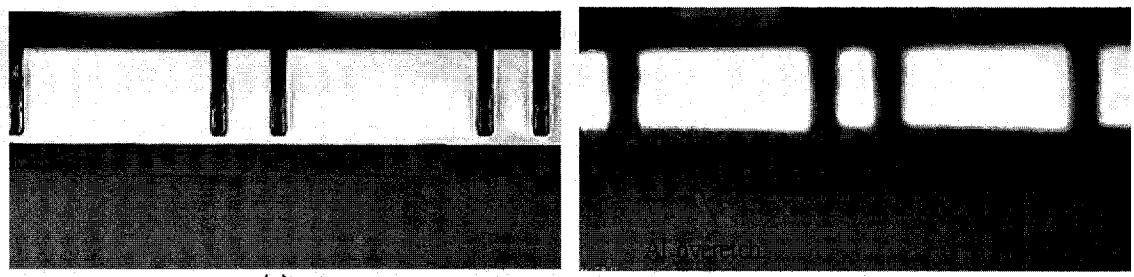

(a) (b)

Figure 6.8 Al patterning: (a) Successful die (b) Al overetch

Following the definition of Al hard mask, PMMA RIE was carried out as outlined in section 5.7.2. The two-step program was run first and some residue near the waveguide enface was observed (Figure 6.9(a)). To alleviate this problem, a third "pump-out" step was added. This step was used to pump out the chamber and thus prevent the etched particles falling on the wafer. It consisted of 15sec gas flow with the same ratio (O_2/Ar = 40/160) at low power (50W) and low pressure (50mTorr). This step helped reduce the amount of residue formed, as can be seen in Figure 6.9(b).

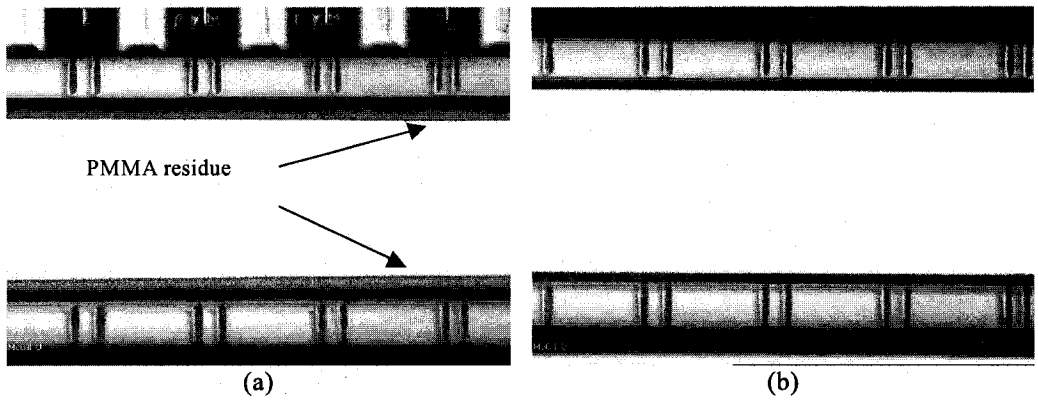

Figure 6.9 PMMA RIE: (a) Without the pump out step, residue is observed; (b) With the pump out step, the amount of residue is considerably reduced

The complete fabrication process flow has been carried out and the problems encountered have been described and solved for most of the processed devices. The device yield following the last fabrication step, has been found to be between 40-60% for all processed wafers. This was considered more than satisfactory given the time and equipment constraints. The final device with the accent on the waveguide area is shown in the figure below.

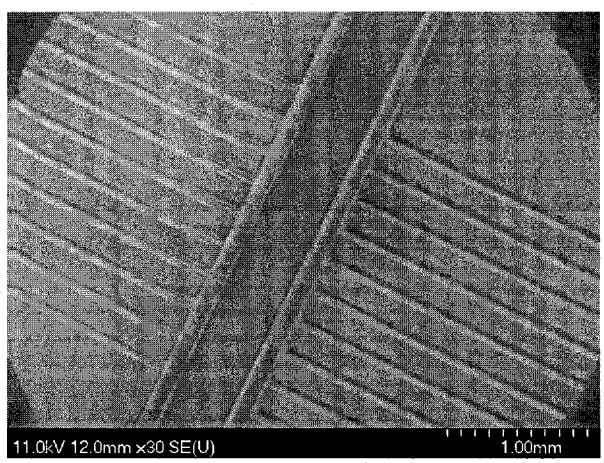

Figure 6.10 SEM image of the final device

The final bonding step could not be performed simultaneously for all devices on the wafer, hence the devices needed to be diced before this procedure, for several reasons. First, the protective cover would need to have predrilled holes to interface with the microfluidic channel and fluid interconnects that match exactly the channel layout of each individual device on the wafer. Given that two-on-one-mask approach was used in patterning of the channels (section 5.2), during the mask rotation necessary for second exposure of the other half of the wafer, an arbitrary horizontal and vertical shift is made

on the wafer pattern. This means that the devices on the left and on the right side of the wafer are not in perfect alignment with each other. Therefore, it would be extremely difficult if not entirely impossible to reproduce the exact layout for interconnecting holes for both wafer sides. Another reason was that the defective devices, having the SU8 patterns lifted off, would prevent the watertight sealing of the complete wafer surface. Hence, after dicing, only the successful devices were considered for bonding. The next section of the chapter describes dicing procedure and different bonding methods employed.

6.4 Final device packaging

As mentioned in the previous section, final device packaging, more specifically bonding, needed to be carried out after wafer dicing and selecting only successful devices for this procedure. These steps are described below.

6.4.1 Silicon wafer dicing

Silicon wafer dicing was carried using the Esec 8003 Dicing Saw equipped with the Thermocarbon diamond resin blade compound, 38μm wide. Given that the devices have not been sealed prior to this step, it was essential to keep the surface contamination from debris produced during wafer dicing to an absolute minimum, which would then allow for the later bonding step to take place. Contamination was largely due to the saw dust which tended to deposit and adhere to the wafer surface. Automatic water jetting system provided by the tool, has been proven helpful in the past for prevention of debris adherence, however, it has not been able to provide complete protection from residue formation. In order to completely remove the residual contamination, generally, the diced parts have to be treated with acetone in an ultrasonic bath. In our case, this kind of surface cleaning would be impossible to perform, as PMMA is easily dissolved in acetone, while ultrasonic bath would cause the SU8 structures to lift off. Therefore, a procedure needed to be developed to prevent the debris from settling onto the wafer surface, permitting the less aggressive cleaning procedure to be carried out. Several parameters such as feed rate, dice blade RPM and surface wetting uniformity, have been found to play an important role in residual contamination control. Several test wafers

containing SU8 and PMMA patterns were processed to determine the optimal parameters that would achieve contamination free dice. The developed dicing procedure is described next.

The wafer was placed on a vacuum carrier plate covered with an adhesive tape to hold the wafer in place and prevent the parts that have been cut from moving which could cause the damage to both, the devices and the blade. Next, using split-screen projector, the wafer was carefully aligned to produce straight cut for all devices. Following the alignment, the dicing parameters were programmed. Dice blade has been set to 18000rpm and the feed rate has been set to 2mm/sec. Using slower feed rate allowed easier and more uniform water stream to be applied to the wafer. In addition to the automated water dispersion system, additional manual wafer flooding with DI water was constantly applied using a water gun. This assured sufficient surface wetting and complete wafer coverage thus preventing the dispersed dust particles from settling on the wafer surface. The cut devices were instantly removed from the carrier plate, placed in a beaker filled with 1:1 ratio of DI water and FL-70 detergent, and left in the solution overnight. Following the 24-hour soak in the cleaning solution, the devices were rinsed with DI water, dried using nitrogen gun and inspected with an optical microscope. No residue was found on the surface of any of the devices. Therefore, the individual devices were ready for bonding.

6.4.3 Bonding

Two different bonding techniques, glass cover bonding using an intermediate adhesion layer and plasma activated or thermally treated PDMS bonding, were attempted for this purpose and are described next.

1. **Glass adhesion bonding**

Glass substrates are often used as covers since they allow for easy visual inspection of the bonded structures [83]. Adhesive bonding is commonly employed method for sealing structures in various materials, including silicon, glass and polymers. This technique uses an intermediate polymer bonding layer to seal the fabricated structures. A wide range of polymers have been used as an intermediate layer, including UV curable epoxies, photoresists, thermoplastics and polyimides [43,64,83-85]. The choice of intermediate

material depends on the mechanical, chemical and thermal requirements of the application. For our purpose of sealing the microchannels, adhesion bonding of glass slide, using an intermediate layer of 950k molecular weight PMMA, at relatively low temperatures, was attempted first. The procedure employed, has been adopted from the researchers of the Technical University of Denmark, who used an intermediate PMMA layer deposited on Pyrex substrate to seal the SU8 microfluidic channels [83,84]. In our case, instead of Pyrex cover, glass microscope slide of 22x22mm dimensions was used and the bonding temperature was decreased to 90°C as opposed to 150°C [83], to avoid reflow of PMMA cladding layers which would destroy the patterned structures. First, a 5μm thick PMMA layer was deposited on a clean glass slide, in the same manner as for the Si wafer (section 5.5). Next, the PMMA was baked on a hot plate at 150°C for 10min to remove the solvent. The glass substrate was then put on top of the device, with the PMMA facing the device. The bonding was carried out at 90°C, with 2000N bonding force and vacuum pressure of 10^{-1} mbar for 10min in EVG bonding machine. After bonding, the devices were inspected using an optical microscope to inspect the quality of the bonded structures. First observation showed that the watertight seal was not accomplished, due to the trapped air bubbles between the glass slide and the intermediate PMMA layer for all the processed devices. Secondly, the bond was found to degrade with time, where after several days, the PMMA layer completely peeled of the glass slide preventing it from sealing the device. Due to the lack of time to fully develop the process for adhesion bonding of the glass slide, it was decided to use PDMS cover instead, which would then alleviate the need of an intermediate adhesive layer.

2. PDMS cover bonding

The silicone elastomer polydimethylsiloxane (PDMS) has gained considerable use in the fabrication of microfluidic devices [86], especially for sealing purposes [87]. In addition to optical transparency, which facilitates the alignment, the primary advantage of PDMS material for microfluidic applications lies in its ease of bonding, both reversibly and irreversibly to different materials, and its biocompatibility in a biological environment [88]. Bonding can be achieved using various methods, such as, plasma treatment [87,88], thermal treatment and UV adhesives [88], or in the simplest case, clamps or spring-mounted screws [2]. Furthermore, fluidic interconnects can be easily punched through

PDMS, due to material softness, using the same syringe needle that can be later employed for fluid injection. Hence, for the above mentioned reasons, it was finally decided to employ PDMS to seal the microfluidic channel using plasma activation method for irreversible bond and thermal treatment for reversible bond. For final device assembly reversible bond was preferred, as this allowed non-intrusive detachment of the lid from the device and subsequent re-assembly for fluid purging and cleaning purpose. PDMS film of 5x10cm, obtained from Marc Herman - department of Biomedical Engineering at McGill University, was cut into rectangles of 1x2cm with a razor blade. Prior to bonding, interconnect holes were punched in PDMS using a syringe needle, ultrasonic cleaning in DI water and isopropyl alcohol for 5 min was carried out, followed by 30min dehydration bake at 90°C in convection oven. Both bonding methods employed are described next.

A. Plasma activated PDMS bonding

Short oxygen plasma treatment of substrate and PDMS cover, by making the surfaces hydrophilic, allows bonding to occur at room temperature [87]. The recipe used is briefly summarized below, while for more informations, the reader is referred to [88,89]. Clean substrate and PDMS with bonding surfaces facing up, enclosed in a petri dish to preserve process cleanliness, were placed in Tegal O_2 Plasma Etch system for 20sec, with the power set to 70W, and the pressure at 0.7mTorr. After activation, PDMS was immediately bonded onto the substrate, by removing the air bubbles starting from the center of PDMS and working outward. Then a sheet of paper was placed on top of PDMS and hard-pressed for 2min. This method achieved channel sealing with an irreversible bond (Figure 6.11(a)).

B. Thermally treated PDMS bonding

As mentioned earlier, thermal treatment resulted in a reversible bond, and was employed for final device sealing as it allowed easy microchannel cleaning by removing the PDMS cover. This technique required heating of the bonding surfaces at 90°C for 15min on a hot plate. Then, both PDMS and the device were removed from the hot plate and pressed together using a screw-adjustable clamp for 5min. Finally, bonded structure was placed back on a hot plate at 90°C for 30min to enhance bonding strength. Such bond, being

reversible, cannot withstand high fluid injection pressure, however it was sufficient to seal the channel for our purpose (Figure 6.11(b)).

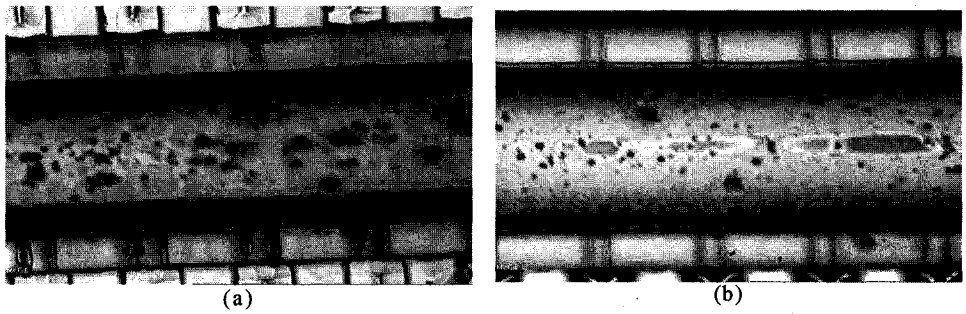

Figure 6.11 Water tight seal achieved using (a) Plasma PDMS bonding and (b) Thermal PDMS bonding

Water tight seal was achieved for both methods as demonstrated in Figure 6.11 (a,b). Food coloring was diluted in DI water and injected into the microchannel using a syringe connected to the needle that was used to punch the hole through the PDMS lid. No liquid was observed in the waveguide or the V-groove area.

6.5 Alternative device design and fabrication

One of the main motivators for the revised device design and fabrication stemmed from the problems encountered during resist spin-coating on the wafer with topography. As no other method was available at the facility for resist deposition, this problem for the developed process flow, could only be solved by resist overexposure. Although this solved the problem for the thicker resist film, it created a number of other problems associated with overexposure as presented above. Another factor that contributed to the alternative device development was that the silicon DRIE process needed to be outsourced which slowed the process step integration. Hence, a revised version of the device to be fabricated using only resources available at McGill microfabrication facility was designed. It employed only two photolithographic steps, an additional benefit in terms of cost reduction. Brief description of the device design and fabrication is presented below.

6.5.1 Device design

The device design is similar to the one presented by Mogensen and al [34,35]. The difference is that they employed SU-8 only in their waveguide design where side

claddings consisted of air. This resulted in increased scattering losses which might not affect the device performance for absorption applications where the strength of the signal is quite large, however it would severely limit fluorescence detection. In the design presented below, to minimize scattering losses, PMMA cladding is used. Schematic of the device is shown in Figure 6.12.

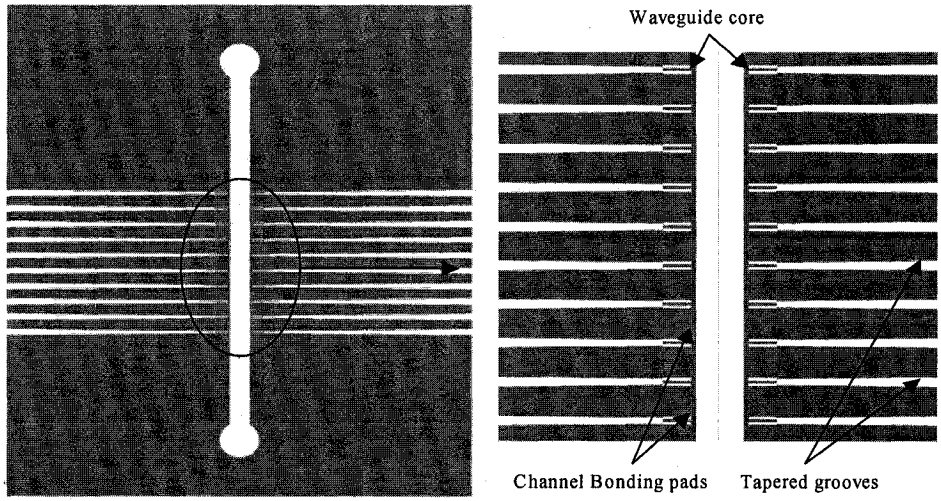

Figure 6.12 Second device layout

The device consisted of 2cm long, 500μm wide microchannel, defined by the bonding pad, with an array of ten waveguides and tapered fibre aligning grooves designed in the same material and placed on both sides of the channel. Given the fibre outer diameter of 65μm, the deposited waveguides consisting of PMMA cladding layers and SU8 core needed to have overall thickness of 65μm. This was achieved by depositing 5μm lower cladding layer, 55μm core and 5μm upper cladding. For this thickness, using BPM simulation, the optimum coupling condition with 40μm fibre core was found to occur for the waveguide width of 32μm (see Appendix E). Several devices varying in waveguide length, channel bonding pad width, side cladding width and width of the taper at the waveguide termination were designed and placed on the same mask to assess the optimum parameter for device packaging and performance (Table 6.1).

Device design	Bonding pad width(um)	Taper width at the waveguide(um)	Side cladding width (um)	Waveguide length(um)
1	10	70	15	500
2	10	70	15	100
3	10	92	30	500
4	50	70	30	300

Table 6.1 Varying device design parameters

6.5.2 Fabrication results

As already mentioned, the device was fabricated using two photolithographic steps, one to define the waveguide core, and the second to remove the PMMA cladding from the grooves and the microchannel region. For this purpose only one mask was ordered from ADTEK with the two masking layers on one plate as before (Appendix D.2). The fabrication proceeded using the same recipes developed for the fabrication of the original design (chapter 5) as follows.

Wafers were cleaned in Piranha solution for 10min to remove all the organic residues followed by DI water rinse and dehydration bake at 200°C for 30min in convection oven. Next, 5μm thick PMMA lower cladding was deposited and cured (table 5.4). Following the PMMA cure, 55μm thick SU8 layer was deposited and patterned (table 5.6) to form the waveguides, the channel and the tapered fibre grooves. The only modified parameter for this step was the spin speed for deposition of SU8-25 that needed an adjustment for producing a uniform 55μm thick film. At the time of the revised device fabrication, an increase in the humidity level was experienced at the microfabrication facility which affected the deposited resist thickness for a fixed spin speed. It was found that to produce a desired film thickness, spin speed needed to be adjusted on a day-to-day basis. The spin cycle time needed to be increased from 30sec to 60sec in order to obtain more uniform film, however increasing the spin cycle time resulted in thinner film for the same spin speed, and as a result, spin speed was decreased dramatically. This spin-speed, for the day of fabrication, was found to be 650rpm for 60sec spin cycle. The deposited film thickness was found to be 55μm +/- 3.05%. Note that under normal lab conditions this speed for 30sec spin cycle would be 1050rpm. After defining the patterns in SU8, PMMA upper cladding was deposited and cured in the same manner it was done for the lower cladding layer. Defined waveguides are shown in the figure below.

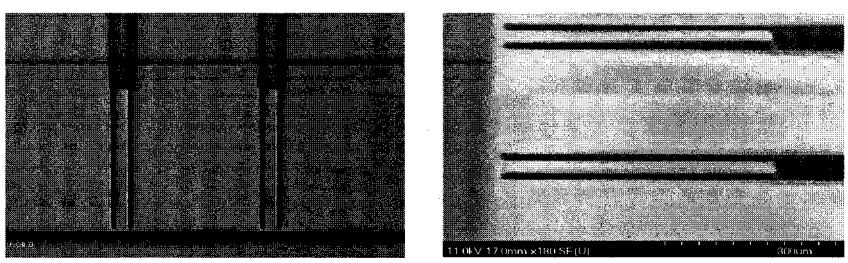

Figure 6.13 SU8 waveguides with PMMA cladding layers as imaged with an optical microscope and SEM

Finally, PMMA needed to be removed from the groove and microchannel area to allow fiber insertion and to clear the waveguide core pathway in the channel. This was done using the developed PMMA RIE recipe for which Al hard mask was employed (section 5.7). Fabricated device is shown in figure below (note that PMMA charges under electron bombardment which caused white reflection patterns in SEM image below).

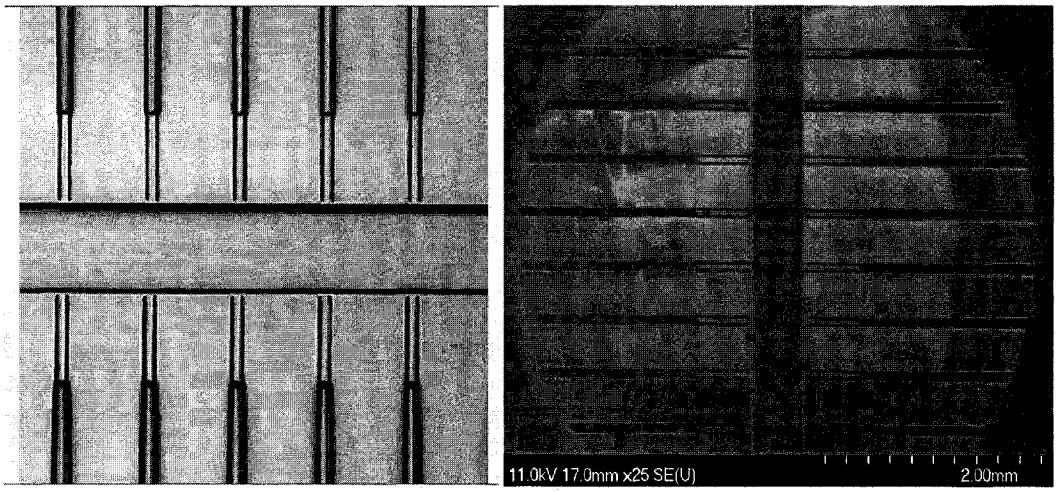

Figure 6.14 Fabrication results as imaged using an optical microscope and SEM

After fabrication, the device was diced and bonded with PDMS lid to seal the channel (section 6.4). As before, watertight seal was achieved and no leakage was found in the waveguide or the groove area (Figure 6.15).

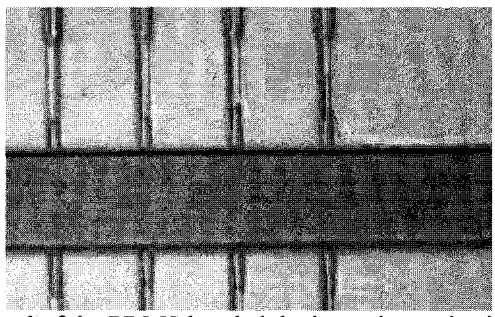

Figure 6.15 Watertight seal of the PDMS bonded device as imaged using an optical microscope

7 Experimental test results

To asses the performance of the fabricated devices, two types of measurements were performed, one to determine the optical losses through the device and the second to demonstrate fluorescence and absorption detection capabilities. This required insertion of the optical fibres in the fabricated grooves (Figure 7.1), which was achieved with the help of an optical microscope or a CCD camera connected to a monitor (Figure 7.2). After insertion, PMMA was used as an adhesive to keep the fibres in place.

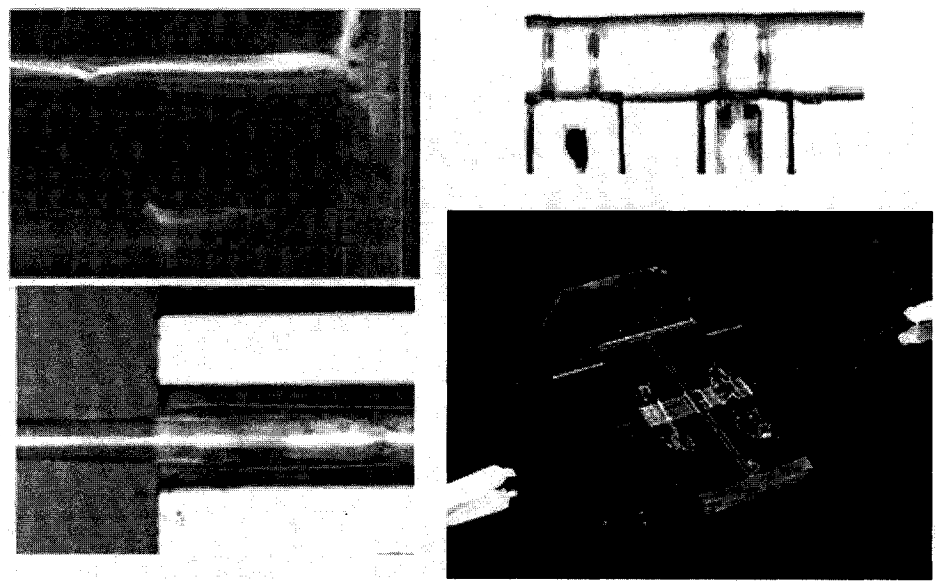

Figure 7.1 SEM and microscope images of fibre inserted in a V-groove and self-aligned to the waveguide (left and top right); image of connected device with laser turned on (bottom right)

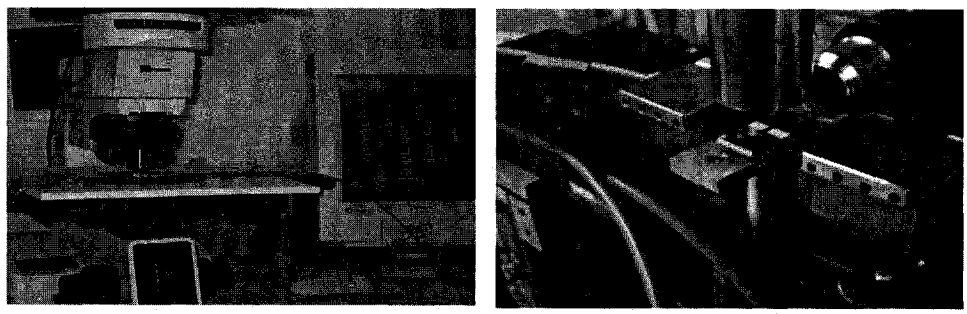

Figure 7.2 Equipment used to visualize fiber insertion (left:optical microscope; right:CCD camera)

Excitation light for all experiments was provided by a 10.4mW He-Ne laser, λ=633nm, which had a permanent single mode fibre (SMF) patchcord attached at the output.

7.1 Transmission efficiency

7.1.1 Polymicro multimode fibre (MMF) losses

In order to compute the propagation losses through the device, first the propagation losses through 2m long Polymicro MMFs were measured. These included both coupling and transmission losses when coupled to the SMF patchcord. Using a Newport photodetector (818F-IR) and optical power meter (2832C)[90], these losses for several patchcords tested, were found to vary between 7.55dB and 10.3dB, corresponding to 9.33% and 17.58% transmission respectively. Such large losses were due to the misalignment of MMF FC termination and SMF FC termination in a connector sleeve. As MMF FC connector was not standard, it was difficult to insert it into the standard FC-to-FC mating sleeve, resulting in poor coupling of fast diverging SMF output. Following the measurement of fiber losses, total propagation loss throughout the device with inserted fibres was determined.

7.1.2 System losses

The setup used for the measurements is shown in Figure 7.3.

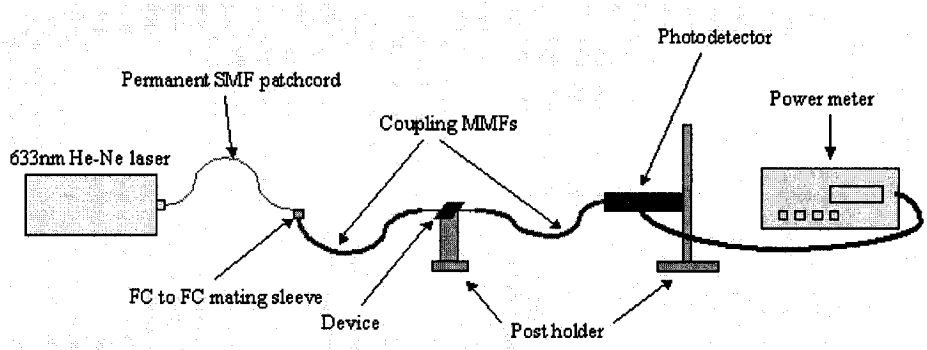

Figure 7.3 Test setup used to characterize the device propagation loss

The propagation loss of the system consists of: (1,5) input/output fibre-waveguide coupling losses ($L_{1\text{-}5}$), (2,4) waveguide transmission losses including absorption and scattering losses ($L_{2\text{-}4}$), (3) channel loss (L_c) including the propagation loss (L_3) and the reflections at SU8-channel interface ($R_{2\text{-}3}$), and (6) output fibre transmission loss (L_6). The schematic indicating each component loss is shown in Figure 7.4 and an estimate of each component loss is summarized in Table 7.1.

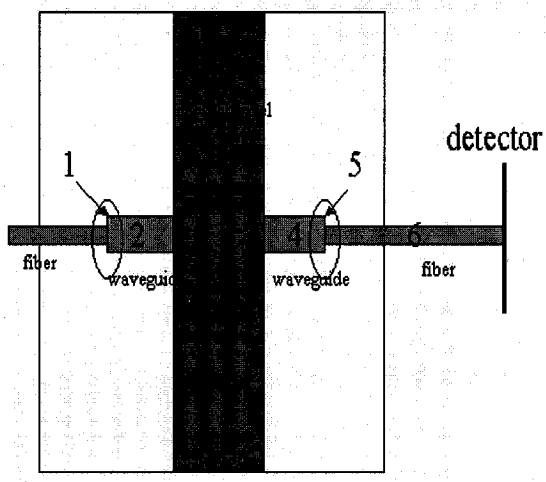

Figure 7.4 Propagation loss of the system

Component	Estimated Loss (dB)	
	Device 1	***Device 2***
1,5	0.98[1]	3.02[1]
2,4	0.03[2]	0.14[2]
3	$Lc^{3}=L_3+2R_{2-3}=L_T-(2L_{1-5}+2L_{2-4}+L_6)$	
6	0.01[4]	
L_T	$2.03+(L_3+2R_{2-3})$	$6.33+(L_3+2R_{2-3})$

Table 7.1 Estimated loss of each component

[1]Loss computed using coupling efficiency without axial misalignment for device 1, and including the axial misalignment for device 2, obtained from BPM simulation
[2]Calculation based on reported SU-8 waveguide loss of 2.7dB/cm [35]
[3]Channel loss $Lc = L_3+0.46$dB for air filled channel and $L_3+0.068$dB for water filled channel
[4]Obtained from fiber manufacturer [45] (6dB/km)

Device 1

For an empty channel (air filled) total loss was measured to be between 13.9 and 16.7dB (4.05% and 2.15% transmission) and with water filled channel it was 9.1 and 11.8dB (12.44% and 6.60% transmission) for the first fabricated device. Hence, the approximated average channel loss was 13.27dB and 8.42dB for air and water filled channel respectively.

Device 2

For the revised device design, only one configuration was tested with waveguide length of 500μm. For this device, total loss was found to be higher; 22.8dB (0.53% transmission) and 17.9dB (1.6% transmission) for air and water filled channel respectively. The estimated loss through the water filled channel was 11.57dB. This loss is higher than the one reported for the first device, however this is only an estimation based on calculations using simulation results for waveguide-fibre coupling losses and literature reported results for SU8 waveguide transmission losses, which do not take into account the variations in processing conditions.

Compared to the device designed by Mogensen and al. [13,35], who measured 11dB and 20dB loss across the water filled 500μm and 1000μm wide channel respectively, the obtained transmission efficiency for the system was found to be satisfactory.

7.2 Analytical measurements

For all the measurements performed, fluorescent dye Alexa Fluor 633 [91] with absorption and emission maxima located at 633nm and 647nm respectively was used. Both devices were tested with the same setup and experimental procedures. Since similar fluorescence measurements were obtained, combined results are presented to avoid repetition.

7.2.1 Test setup and measurement procedure

Fluorescence emissions were analyzed using a similar setup configuration as that shown in Figure 7.3. The modification included placing a bandpass filter (Omega optical) [92] at the detector input, to filter out the excitation light and pass only the emitted fluorescence signal. A CCD camera equipped with a microscope objective lens was placed above the channel at the excitation volume region, to image the fluorescence emission. The modified schematic of the setup is shown in Figure 7.5.

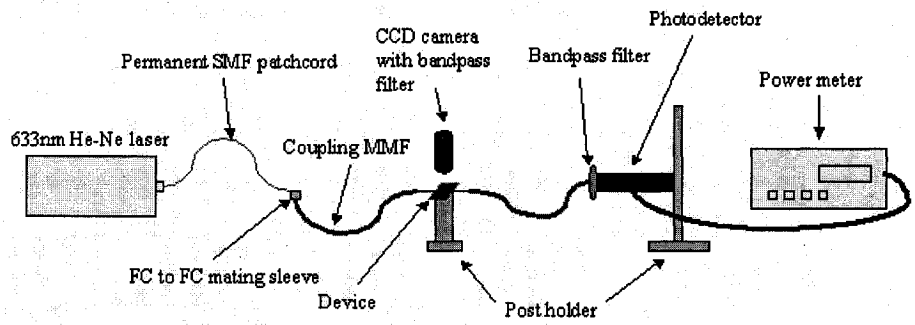

Figure 7.5 Test setup used for fluorescence measurements

To avoid degradation of signal to noise ratio (SNR) and measurement errors due to background noise, fluorescence measurements were carried out in a dark room. The detector signal with the excitation light off was found to be negligible (<0.0001μW). In order to allow for a complete signal and noise analysis to be made, the buffer signal level was measured prior to each fluorescence measurement by filling the channel with water. The total signal consisting of the sum of buffer and analytical signals was then measured for different analyte concentrations. After each fluorescence measurement, the channel was flushed with water to ensure that no significant memory effects took place due to adsorption of the sample molecules onto the channel walls.

7.2.2 Measurement results

The dye was prepared in concentrations ranging from $1x10^{-8}$M to $1x10^{-3}$M to find the limit of detection (LOD). LOD was defined as the analyte concentration at which signal to noise ratio (SNR) equals 3 [16]. SNR was computed using the following relation [23]:

$$\mathrm{SNR} = \frac{\left(\overline{S} - \overline{B_k}\right)^2}{\sigma_s^2 + \sigma_{Bk}^2}$$

where $\overline{S}$ and $\overline{B_k}$ are the average values of the fluorescence and the background (buffer) signal respectively, while noise is presented as sum of variances σ_s^2 and σ_{Bk}^2. At the smallest prepared concentration of 10nM, SNR was found to be 7.5, which was above the defined LOD. Due to time constraints, smaller concentrations were not prepared, hence 10nM was taken as a value for LOD of the system. Figure 6.5 shows the signals obtained when DI water and several different concentrations of Alexa Fluor 633 solution are introduced in the channel. Measurements are taken over a time period of 60sec.

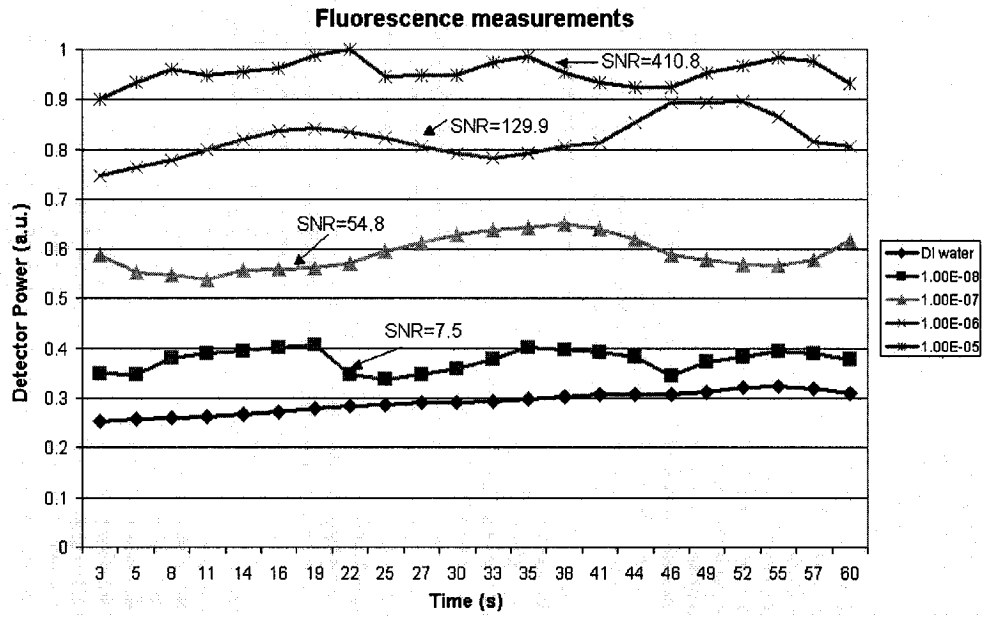

Figure 7.6 Signal detected for DI water and several concentrations of AlexaFluor 633 solution

Variations in the signal level are contributed to laser and detector flicker. At higher dye concentration (C=0.1mM), a phenomenon called "concentration quenching" [29] was observed (Figure 7.7 (a)), which is due to the reabsorption of the emitted fluorescence (self-absorption), resulting in fluorescence loss. For lower concentrations, the increase in fluorescence signal is fairly linear (Figure 7.7(b)).

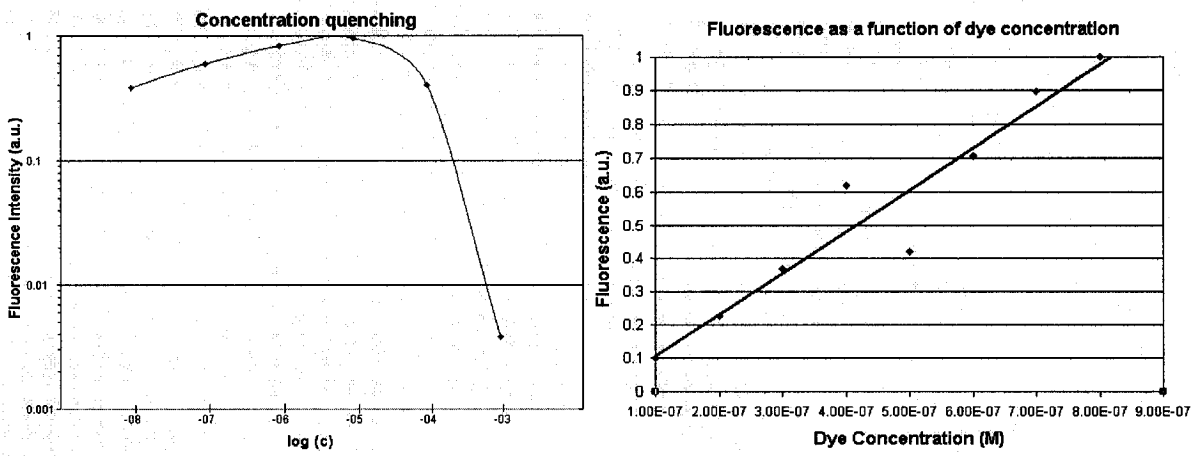

Figure 7.7 Fluorescence signal vs. dye concentration (a)Log-log plot of the fluorescence signal showing the "concentration quenching"; (b) Curve of fluorescent light collected versus AlexaFluor concentration

Finally an image of the fluorescence emission in the microchannel filled with the 10μM dye solution was taken (Figure 7.8) using a CCD camera with bandpass filter attached to remove the excitation laser light.

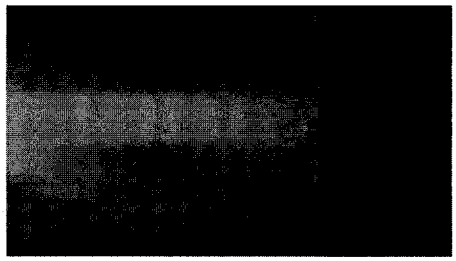

Figure 7.8 Image of emitted fluorescence coupled into the output waveguide

7.3 Absorption measurements

Absorption measurements were also attempted using the first fabricated device and Alexa Fluor 633 dye, which has the extinction coefficient of 10^4 [91]. The same setup from Figure 7.3 was used for this purpose. Note that no filter was placed at the detector to remove the fluorescence of the dye. Absorption was measured at three different concentrations, 0.1μM, 1μM and 10μM, after which the inserted fiber tip broke and further measurements were not performed due to time constraints. For the first two concentrations, absorption of excitation wavelength was apparent, since the measured signal decreased in comparison with the buffer solution (Figure 7.9), however with increased concentration (10μM), the fluorescence signal of the dye was much stronger and absorption could not have been observed without the appropriate filters that would filter out the fluorescence signal. The LOD was found to be less than 1μM.

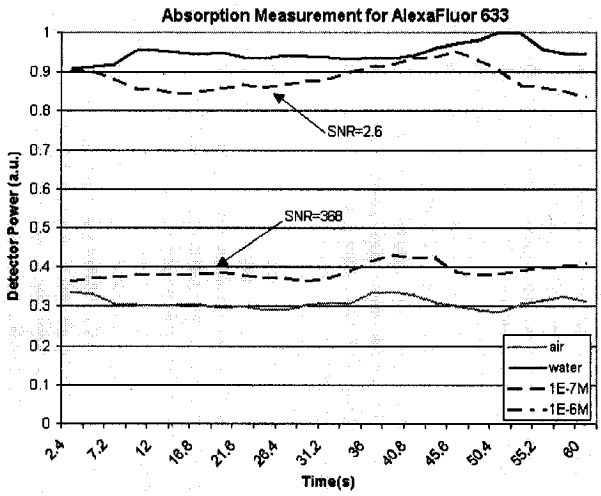

Figure 7.9 Unfiltered detector signal for 0.1μM and 1μM of Alexa Fluor 633 solution

7.4 Issues encountered during experimental procedures

The major issue encountered during experimental procedures related to sample insertion and washing cycle that needed to be performed after each measurement. Solution was inserted into the channel using manually operated syringe with a needle, due to the lack of pressure driven syringe pump (Figure 7.10).

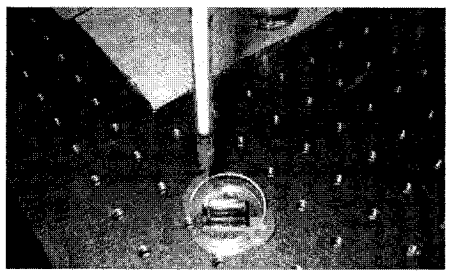

Figure 7.10 Image of manual liquid insertion into the device using a syringe

With this method continuous solution pumping could not be performed, so after first measurement, PDMS cover had to be removed to allow for the washing procedure. However after this step, bonding with the same PDMS lid could not be achieved. Either plasma or thermal treatment needed to be performed to reseal the channel, which was not attempted, as the fibre connections could not be removed for this step. Hence for the other measurements, the channel was filled with the solution and cover was placed on top of the device which might have caused small amount of analyte to leak outside of the channel, which could not be prevented. This might explain some of the discrepancies for the fluorescence signal curve, exhibiting nonlinearity at few measurement points.

8 Conclusion

So far, we have presented the realization of an optical detection setup based on guided wave optics with potential for integration into a micrototal analysis system. An array of optical waveguides were fabricated in spin-on polymer technology on a silicon substrate and monolithically integrated with the microfluidic channel and the V-groove fibre alignment scheme. The design and the layout of the integrated planar waveguides in the microfluidic optical detection system has been adapted to accommodate both absorption and fluorescence measurement schemes. Two different versions of the device were designed and fabricated at McGill microfabrication facility. In the development of both structures, a number of fabrication processes were developed that will have application beyond this specific device to the creation of other MEMS structures.

The evaluation of the integrated polymer optical waveguide approach to miniaturization of fluorescence and absorption spectroscopy system shows, so far, that the requirements outlined in chapter 3 are or can be met. Total system losses with water filled microchannel were experimentally determined to be 10.45dB and 17.9dB for the two different versions of the devices. These losses are comparable to or lower than those found in literature [13, 35]. Both fluorescence and absorption detection capabilities of the fabricated devices were demonstrated using Alexa Fluor 633 dye, and the corresponding detection limits (LOD) were found to be less than 10nM and 1μm respectively. A direct comparison to other detection systems would require utilization of the same fluorescent dye for exactness, nonetheless, the presented detection system has low LOD, comparable to the detection system based on silica-on-silicon waveguide technology [10,15] and detection system that utilizes microlenses [23] (see Table 2.1). Additional benefits of the presented detection system include the following assets:

(i) The use of integrated optical waveguide technology in the detection system allows simultaneous multianalyte detection and increases system throughput. Furthermore, monolithic integration of the optical waveguides with the microfluidic channel provides precise alignment of the optical components and inherent system stability.

(ii) Integration of a V-groove fibre coupling method on chip allows system portability and reduces packaging time and cost.

(iii) The use of inexpensive polymer materials (SU8 and PMMA) in the device fabrication enables rapid production and thicker waveguiding layers, which reduces system costs and increases sensitivity.

(iv) The design is adapted to accommodate for both fluorescence and absorption measurements thus encompassing the benefits of both methods: fluorescence for highly sensitive analysis and absorption for label-free detection.

(v) All the fabrication steps are fully automated and thus amenable to mass production.

(vi) The choice of silicon as a substrate offers the opportunity to produce fully integrated structure for complete LAC system.

Further testing of the devices is needed to experimentally determine the optical loss of each component and asses the fabrication and design parameters influencing the specific component performance. This includes the measurement of the waveguide transmission losses, since those have been taken from literature for system analysis purposes (Chapter 7). Waveguide transmission losses can be found using the cut-back method. Several test waveguiding structures that are not interrupted by a microchannel, have been included on the mask layout of the second device and fabricated for this purpose. In addition to this, several areas of improvements in the detection system design and fabrication have been identified for future works towards better integration for a Lab-on-a-chip system.

8.1 System optimization

8.1.2 Design

The presented design has been optimized to minimize the coupling losses with the optical fibres under the imposed fabrication constraints, however further optimization of the waveguide components with the same fabrication methods and materials is possible. Instead of rectangular waveguiding structures, horizontal tapers can be included to improve the collection/dispersion efficiency at the chamber interface [29,30]. This requires careful design of the taper profiles of both input and output waveguides, which can be realized using BPM simulation software [93]. In addition to this, beam splitters can be included in the waveguide design in the form of Y-branches [30] for instance, to allow simultaneous excitation using a single source. This feature would prove extremely important if a light source is to be integrated on the same chip.

8.1.3 Fabrication

Due to the limitation of the maximum cladding thickness deposition, an estimated coupling loss increase from the optimum 34μm square waveguide core, based on BPM simulation, has been determined to be as high as 5.48dB for both input and output waveguide/fibre coupling. Since the lower cladding layer could be deposited only up to 5μm thickness without compromising the structural integrity of the device, and due to the monolithic integration of the fibre self-aligning V-grooves, the core layer needed to be 47μm thick to ensure planar chip surface for bonding. Besides increase in coupling losses due to the increase in core thickness (2×0.86dB), this created additional coupling losses due to axial waveguide-to-fibre misalignment (2×1.88dB), which was especially critical for the output structures. These losses can potentially be minimized or even eliminated if a different cladding material that can be deposited in thicker layers (11.5μm) is employed. For example, Eldada et al. [94] report on the development of photopatternable high-performance organic polymers (ASI optical polymers) with better optical and material properties than those of PMMA and that can be deposited in thickness up to 100μm, making them a good candidate for this purpose.

8.2 Future works

While the proposed design integrates a part of the detection system to the reactive phase, it does not completely achieve total integration yet. Indeed, much research is now being pursued in order to monolithically integrate light-emitting sources as well. These can be, for instance, silicon avalanche diodes [95] or microfluidic dye lasers [95,96]. This integration could be made much more easily using the presented IOW design, compared to microlens or embedded fibres solutions, for example. The active light-emitting region could be constructed on the same silicon substrate with readily available microfabrication techniques, and monolithically aligned to the core layers of the embedded waveguides for best light coupling. The same could be done at the other end with photodetectors, utilizing standard p/n junctions. Such system will one day revolutionize the biochemical field, and be commonly used for many biomedical or environmental monitoring purposes.

9 References

Chapter 1

[1] Huikko, K. et al., "Introduction to micro-analytical systems: bioanalytical and pharmaceutical applications," European J. of Pharmaceutical Sci., 20, pp.149-171, 2003
[2] Wang, Z., et al., "Measurement of scattered light on a microchip flow cytometer with integrated polymer based optical elements," Lab Chip, 4, pp.372-377, 2004
[3] Verpoorte, E. et al., "Microfluidics meets MEMS," Proc. Of IEEE, Vol. 91, No. 6, pp. 930-953, June 2003
[4] Medoro, G., "A lab-on-a-chip for cell detection and manipulation," IEEE Sensors J., Vol. 3, No. 3, pp. 317- 325, June 2003
[5] Luppa, P., et al., "Immunosensors — principles and applications to clinical chemistry," Clinica Chimica Acta 314, pp.1-26, 2001
[6] Nabok, A.V., "Planar silicon nitride waveguides for biosensing," IEE Proc. Nanobiotechnol., Vol. 150, No. 1, pp.25-30, June 2003
[7] Ligler, F. S. and Taitt, C.A.R., *Optical Biosensors: Present and Future*, Elsevier Science Ltd., 2002
[8] Duveneck, G. L., et al., "Planar waveguides for ultra-high sensitivity of the analysis of nucleic acids," Analytica Chimica Acta 649, pp.49-61, 2002
[9] Lakowicz, J.R., *Principles of fluorescence spectroscopy*, 2nd Ed., Kluwer Academic/Plenum Publishers, New York, 1999
[10] Hubner, J., et al. "Integrated optical measurement system for fluorescence spectroscopy in microfluidic channels," Review of Scientific Intruments, Vol. 72, No. 1, pp.229-233, January 2001
[11] Tissue, B.M., "Spectroscopy," Chemistry department, KAIST University, Republic of Korea, Feb. 26, 1996. May 30, 2005. <http://elchem.kaist.ac.kr/vt/chem-ed/spec/spectros.htm>
[12] McMullin, J. N., et al., "Optical detection system for biochips using plastic fiber optics," Rev. of Sci. Instr., Vol. 74, No. 9, pp. 4145-4149, Sept. 2003
[13] Mogensen, K. B., et al., "Ultraviolet transparent silicon oxynitride waveguides for biochemical Microsystems," Optics Letters, Vol. 26, No.10, pp.716-718, May 2001
[14] Deverkadra, P. R. and McShane, M. J. "Fabrication of a biosensor with embedded waveguides for sensing in microchannels" IEEE Proceedings of the 2nd Joint EMBS/BMES Conference, Houston, pp.1720-1721, October 23-26, 2002
[15] Friis, P., et al., "Monolithic integration of microfluidic channels and optical waveguides in silica on silicon," Applied optics, Vol. 40, No.34, pp. 6246-6251, Dec. 2001
[16] Ruano, J. M., et al., "Flame hydrolysis deposition of glass on silicon for the integration of optical and microfluidic devices," Anal. Chem. 72, pp.1093-1097, 2000
[17] Leeds, A.R. et al., "Integration of microfluidic and microoptical elements using a single-mask photolithographic step," Sensors and Actuators A, Vol 115, pp.571-580, September 2004

Chapter 2

[18] Garcia, N., "Sandians seek tiny chemistry lab on a chip," Sandia Lab News, 28/04/1998, 23/07/2005, <

http://www.sandia.gov/LabNews/LN04-24-98/chip_story.html>
[19] Roy, S., and Fleischman, A., "MEMS and Micromachining in the New Millennium: Biomedical Applications Aid Surgery, Diagnosis, Drug Delivery and More," Medical Equipment Designer, 09/10 1999, 07/06/2005, <
http://www.manufacturingcenter.com/med/archives/0999/999mem.asp>
[20] Jack W. Judy, "Microelectromechanical Systems (MEMS) - Their Design, Fabrication, and Broad Range of Application", *Journal of Smart Materials*, vol. 10, no. 6, pp. 1115-1134, December 2001
[21] Jack W. Judy, "Biomedical Applications of MEMS", Measurement Science and Technology Conference, Anaheim, CA, pp. 403-414, January 20-22, 2000
[22] Madou, M. J., *Fundamentals of Microfabrication: the science of miniaturization*, 2nd Ed., CRC Press LLC, 2002, USA
[23] Roulet, J-C., et al., "Fabrication of multiplayer systems combining microfluidic and microotical elements for fluorescence detection," Journal of Microelectromechanical Systems, Vol 10, No.4, pp. 482-491, Dec. 2001
[24] Balberg, M., et al., "Optical detection of molecular beacons in microfluidic devices," 1st Annual International IEEE-EMBS Special Topics Conference on Microtechnologies in Medicine and Biology, Lyon, France, pp.425-428, October 2000
[25] Chabinyc, M. L., "An integrated fluorescence detection system in poly(dimethylsiloxane) for microfluidic applications," Anal. Chem. 73, pp.4491-4498, 2001
[26] Whitesides, G. M., "Components for integrated poly(dimethylsiloxane) microfluidic systems," Electrophoresis, 23, pp. 3461–3473, 2002
[27] Chang-yen, D.A. and Gale, B. K., "An integrated optical oxygen sensor fabricated using rapid prototyping techniques," Lab Chip, 3, pp.297-301, 2003
[28] Burke, C. S., "Design and fabrication of enhanced polymer waveguide platforms for absorption-based optical chemical sensors," Meas. Sci. Technol., 15, pp.1140-1145, 2004
[29] Ruano, J.M., et al., "Fabrication of integrated microanalytical chambers and channels for biological assays using flame hydrolysis deposition glass," Microelectronic Engineering 46, pp.419-422, 1999
[30] Ruano, J. M., et al., "Design and fabrication of a silica on silicon integrated optical biochip as a fluorescence microarray platform," Biosensors and Bioelectronics 18, pp.175-184, 2003
[31] Mackenzie, K. D. and Lateef, A., "High rate PECVD for Silica," Magneto Electronics Business Unit, Unaxis USA, Inc.
[32] Lien, V. et al., "A prealigned process of integrating optical waveguides with microfluidic devices," IEEE Photonics Technology Letters, Vol. 16, No. 6, pp.1525-1527, June 2004
[33] Lin, C. H. et al., "Micro capillary electrophoresis chips integrated with buried SU-8/SOG optical waveguides for bio-analytical applications," Sensors and Actuators A 107, pp.125-131, 2003
[34] Mogensen, K. B., et al., "Integrated polymer waveguides for absorbance detection in chemical analysis systems," Transducers'03 (The 12th International Conference on Solid State Sensors, Actuators and Microsystems), Boston, pp.694-697, June 2003
[35] Mogensen, K. B., et al., "Integrated polymer waveguides for optical detection in chemical analysis systems," Applied Optics, Vol. 42, No. 19, pp. 4072-4079, July 2003

Chapter 3

[36] Borreman, A. et al., "Fabrication of polymeric multimode waveguides and devices in SU-8 photoresist using selective polymerization," Proc. Symposium IEEE/LEOS Benelux Chapter, Amsterdam, pp.83-86, 2002
[37] Strandman, C. et al., "Bulk silicon holding structures for mounting of optical fibers in the V-grooves," Journal of Microelectromechanical systems, Vol. 6, No. 1, pp. 35-40, March 1997
[38] Zhao, Y. G., et al., "Polymer waveguides useful over a very wide wavelength range from the ultraviolet to infrared," Applied Physics Letters, Vol. 77, No. 19, pp. 2961-2963, November 2000
[39] Yeniay, A., et al., "Ultra-low-loss polymer waveguides," Journal of Lightwave Technology, Vol. 22, No.1, pp.154-158, January 2004
[40] Musa, S. et al., "Fabrication of polymeric multimode waveguides for applications in the local area network and optical interconnects," Proc. Symposium IEEE/LEOS Benelux Chapter, The Netherlands, pp.95-98, 2000
[41] T. Kaino, *Polymers for Lightwave and Integrated Optics*, Ed. Lawrence A. Hornak, Marcel Dekker, New York, Chapter 1, 1992.
[42] McGill Nanotools Micromachining Fab < http://www.physics.mcgill.ca/nanotools/>
[43] Jackman, R.J., et al., "Microfluidic systems with on-line UV detection fabricated in photodefinable epoxy," J. Micromech. Microeng., 11, pp.263-269, 2001
[44] Lee, G. B., et al., "Micro flow cytometers with buried SU-8/SOG optical waveguides," Sensors and Actuators A 103, pp.165-170, 2003

Chapter 4

[45] Polymicro tehnologies, www.polymicro.com
[46] Optiwave Corporation, http://www.optiwave.us/bpm/optibpm.htm
[47] Yamada, Y., et al., "High silica multimode channel waveguide structure for minimizing fiber-waveguide-fiber coupling loss," Journal of Lightwave Technology, Vol. 4, No. 3, pp.277-282, March, 1986
[48] Kurokawa, T., et al, "Polymer optical circuits for multimode optical fiber systems," Applied Optics, Vol.19, No.18, pp.3124-3129, September 1980
[49] Optical Research Associates (ORA®), <www.opticalres.com/products_f.html#codev>

Chapter 5

[50] Dotson, N.A., et al., "Low cost MEMS processing techniques," Proc. ASEE/NCS Spring Conference, Kalamazoo MI, April 2004
[51] Autodesk, Inc., <www.autocad.com>
[52] ADTEK Photomask, "Using AutoCAD as a photomask design tool," Montreal, Canada, www.adtekphotomask.com
[53] Flack, W. et al., "A mathematical model for spin coating polymer resists," J. Appl. Phys., 56, 1199 (1984)
[54] Colzani, M., "A novel robotic workcell makes high-end MEMS devices," Sensors, May 2003
[55] Ilic, R., Cornel NanoScale Science and Technology Facility, <www.cnf.cornell.edu>

[56] Ohara, T., et al., "Resist film formation in spin coating," InterSociety Conference on Thermal Phenomena, pp.281-288, 1992
[57] McAuley, S.A., et al., "Silicon micromachining using a high-density plasma source," J. Phys. D: Appl. Phys., 34, pp.2769-2774, 2001
[58] Gösele, U. and Tong, Q.T., *Science and technology of semiconductor wafer bonding*, in print, (sample chapter 7 <http://www.duke.edu/web/wbl/ch7/ch7-hpge.html#7.2.2.1>
[59] Schnakenberg, U. et al., "TMAHW etchants for silicon micromachining," In Proc. Transducers, Dig Tech Papers, San Francisco, CA, pp.815-818, 1991
[60] Tabata, O. et al., "Anisotropic etching of silicon in TMAH solutions," Sensors and Actuators, A34, pp.51-57, 1992
[61] Microchem Corp., "PMMA datasheet," <www.microchem.com>
[62] H. Guckel, et al., "Deep X-Ray and UV Lithographies for Micromechanics," Technical Digest IEEE Solid-State Sensor and Actuator Workshop, June 1990
[63] Harry J. Levinson, *Principles of Lithography*, SPIE Press, 2001
[64] Lin, C-H. et al., "A new fabrication process for ultra-thick microfluidic microstructures utilizing SU-8 photoresist," Journal of Micromechanics and Microengineering, 12, pp.590-597, 2002
[65] Bogdanov, A. et al., "Use of SU8 PR for very high aspect ratio x-ray lithography," Microelectron. Eng., 53, pp.493-496, 2000
[66] Zhang, J., et al., "Characterization of the polymerization of SU8 photoresist and its applications in micro-electro-mechanical systems (MEMS)," Polym. Test., 20, pp.693-701, 2001
[67] Eyre, B., et al., "Taguchy optimization for the processing of EPON SU-8 resist," Proc. MEMS'98 (IEEE, Heidelberg, Germany) pp.218-2122, 1998
[68] Zhang, J., et al., "Polymerization optimization of SU8 photoresist and its applications in microfluidic systems and MEMS," J. Micromech. Microeng., 11, pp.20-26, 2001
[69] Hong, S.J., et al., "Characterization of low-temperature SU-8 photoresist processing for MEMS applications," IEEE/SEMI Adv. Semiconductor Manufacturing Conf., 2004
[70] Lorenz, H. et al., "Mechanical Characterization of a new high-aspect ratio near UV-PR," Microelectron. Eng., 41-42, pp.371-374, 1998
[71] Chang, H.K. et al., "UV-LIGA process for high aspect ratio structure using stress barrier and C-shaped etch hole," Sensors and Actuators A 84, pp.342-350, 2000
[72] Conradie, E.H. et al., "SU-8 thick photoresist processing as a functional material for MEMS applications," J. Micromech. Microeng., 12, pp.368-374, 2002
[73] Despont, M. et al., "High-aspect-ratio, unltrathick, negative-tone near-UV photoresist for MEMS applications," IEEE, pp.518-522, 1997
[74] Microchem Corp., "SU8-25 datasheet," <www.microchem.com>
[75] EVG, "Automated SU-8 resist processing," courtesy of Chad Brubaker
[76] Wong, A. et al., "Application of SU-8 in flip chip bump micromachining for millimeter wave applications," Proc. Of 3rd Electronics Packaging Technology Conference, pp.204-209, Dec. 2004
[77] SU-8: A thick photoresist for MEMS, <http://aveclafaux.freeservers.com/SU-8.html> (accessed on 8/9/2004)
[78] Williams, K.R. et al., "Etch rates for Micromachining Processing," Part II, Journal of Microelectromechanical Systems, Vol 12. No 6, December 2003

[79] Woodruff, G.W., "Microfluidic Channels in Polymethylmethacrylate by Opitmizing Aluminum Adhesion," 22nd Annual Microelectronic Engineering Conference, May 2004
[80] Zhang, C., "Deep reactive ion etching of commercial PMMA in O_2/CHF_3, and O_2/Ar-based discharges," Journal of Micromechanics and Microengineering, 14, pp.663-666, 2004

Chapter 6

[81] Brubaker, C., et al., "Investigating the use of spray coating technology in MEMS applications," Micro Magazine, pp.45-55, March 2004
[82] Pham, N.P. et al., "Spin, spray coating and electrodeposition of photoresist for MEMS structures - A comparison," Proc. SAFE, the Netherlands, November 2002
[83] Bilenberg, B. et al., "PMMA to SU-8 bonding for polymer based lab-on-a-chip systems with integrated optics," J. Micromech. Microeng., 14, pp. 814-818, 2004
[84] Bilenberg, B., "Technology for integrated optics on Lab-on-a-chip microsystems," M. Sc. Thesis, Technical University of Denmark, September 2003
[85] Pan, C.T., et al., "A low temperature wafer bonding technique using patternable materials, " J. Miromech. Microeng., 12, pp.611-615, 2002
[86] Garra, J. et al., "Dry etching of polydimethylsiloxane for microfluidic systems," J. Vac. Sci. Technol., A 20 (3), pp.975-982, 2002
[87] Mia, X., et al., "Low temperature bonding for wafer scale packaging and assembly of micromachined sensors," Final Report for MICRO Project 98-144, University of California, 1998-99
[88] Li, S., et al., "Polydimethylsioxane fluidic interconnects for microfluidic systems," IEEE transactions on advanced packaging, Vol. 26, No. 3, pp. 242-247, August 2003
[89] Duffy, D.C., et al., "Rapid Prototyping of Microfluidic Systems in Poly(dimethylsiloxane)," Anal. Chem., 70 (23), 4974 -4984, 1998

Chapter 7

[90] Newport corporation, <www.newport.com>
[91] Invitrogen Molecular Probes,
<http://probes.invitrogen.com/handbook/sections/0103.html>
[92] Omega optical, <http://www.omegafilters.com/>

Chapter 8

[93] Duport, I., et al., "Study of linear tapered waveguides made by ion exchange in glass," J. Phys. D: Appl. Phys. 25, pp.913-918, 1992
[94] Eldada, L. et al., "Advanced polymer systems for optoelectronic integrated circuit applications," SPIE Vol. 3006, pp.344-361, 1997
[95] Misiakos, K., et al. "Monolithic integration of light emitting diodes, detectors and optical fibres on a silicon wafer: A CMOS compatible optical sensor," IEEE/IEDM 98, pp.25-28, 1998
[96] Balslev, S. et al., "Fully integrated optical system for lab-on-a-chip application," Proceedings of the 17th IEEE MEMS, pp.89-92, 2004
[97] Balslev, S. and Kristensen, S. "Microfluidic single-mode laser using high-order Bragg grating and antiguiding segments," Opt. Express 13, pp. 344-351, 2005

Appendix A Coupling efficiency

The coupling loss between the fibres and the waveguides is believed to be induced in the main by the difference in cross-sectional shapes, which gives two types of loss, Li and Lo, in light propagation from fibre to waveguide and waveguide to fibre, respectively. Theoretical optimum waveguide structure that minimizes these losses can be obtained on the basis of ray optic analysis, using the following Matlab code [47,48]:

```
% Code that computes the coupling loss due to geometry difference (circular-rectangular
% cross section):

waveguide_width = 30:1:40;
fiber_diameter = 40;

%Fiber-to-waveguide loss (Li)
Li=0;
p = waveguide_width / fiber_diameter;
if p<(1/sqrt(2))
   Li=-10.*log10(4.*p.^2./pi);
else if p>=1
      Li = 0;
   else Li = -10.*log10((1-(4./pi).*(asin(sqrt(1-p.^2)-p.*sqrt(1-p.^2)))));
   end
end

%waveguide-to-fiber loss (Lo)
if p<(1/sqrt(2))
   Lo=0;
else if p>=1
      Lo = -10.*log10(pi/(4.*p.^2));
   else Lo = -10.*log10(sqrt(p.^(-2)-1)-(1./(2.*p.^2)).*(asin(sqrt(1-p.^2))-asin(p)));
   end
end

%plot loss due to geometrical mismatch:
L_total = Li+Lo;
figure(1)
plot(waveguide_width,Li, 'b', waveguide_width,Lo, 'r', waveguide_width,L_total, 'm');
title('Coupling loss dependence on the waveguide width with fiber core of 50um diameter');
legend('Fiber-waveguide (Li)', 'Waveguide-fiber (Lo)', 'Total loss = Li+Lo');
ylabel('Coupling loss (dB)');
xlabel('waveguide width (um)');
```

For the derivation of the relations used in the code, the reader is referred to [48].

Appendix B Code V Lens data manager

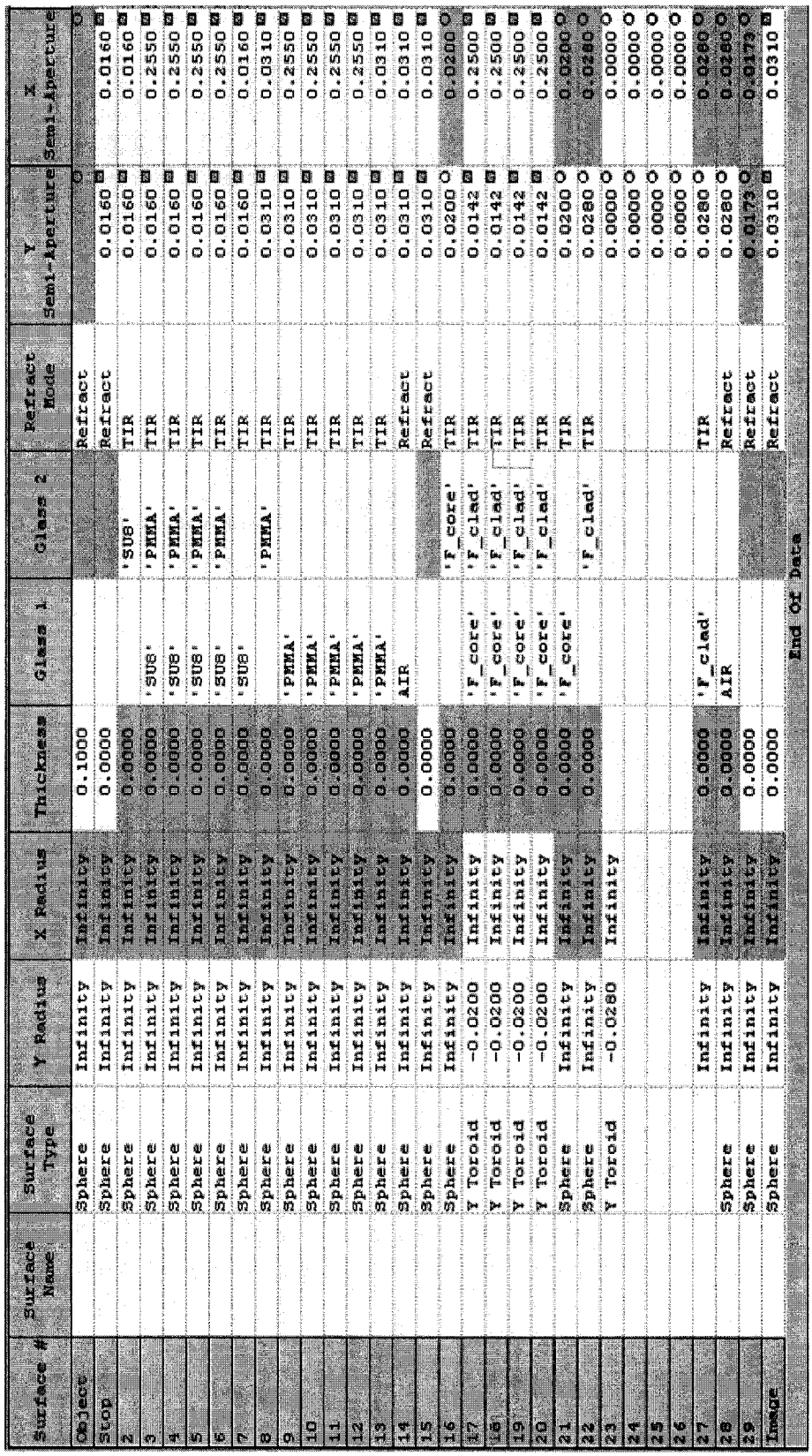

Surface #	Surface Name	Surface Type	Y Radius	X Radius	Thickness	Glass 1	Glass 2	Refract Mode	Y Semi-Aperture		X Semi-Aperture	
Object		Sphere	Infinity	Infinity	0.1000			Refract				
Stop		Sphere	Infinity	Infinity	0.0000			Refract	0.0160	U	0.0160	U
2		Sphere	Infinity	Infinity	0.0000		'SU8'	TIR	0.0160	U	0.0160	U
3		Sphere	Infinity	Infinity	0.0000	'SU8'	'PMMA'	TIR	0.0160	U	0.2550	U
4		Sphere	Infinity	Infinity	0.0000	'SU8'	'PMMA'	TIR	0.0160	U	0.2550	U
5		Sphere	Infinity	Infinity	0.0000	'SU8'	'PMMA'	TIR	0.0160	U	0.2550	U
6		Sphere	Infinity	Infinity	0.0000	'SU8'	'PMMA'	TIR	0.0160	U	0.2550	U
7		Sphere	Infinity	Infinity	0.0000	'SU8'		TIR	0.0160	U	0.0160	U
8		Sphere	Infinity	Infinity	0.0000		'PMMA'	TIR	0.0310	U	0.0310	U
9		Sphere	Infinity	Infinity	0.0000	'PMMA'		TIR	0.0310	U	0.2550	U
10		Sphere	Infinity	Infinity	0.0000	'PMMA'		TIR	0.0310	U	0.2550	U
11		Sphere	Infinity	Infinity	0.0000	'PMMA'		TIR	0.0310	U	0.2550	U
12		Sphere	Infinity	Infinity	0.0000	'PMMA'		TIR	0.0310	U	0.2550	U
13		Sphere	Infinity	Infinity	0.0000	'PMMA'		TIR	0.0310	U	0.0310	U
14		Sphere	Infinity	Infinity	0.0000	AIR		Refract	0.0310	U	0.0310	U
15		Sphere	Infinity	Infinity	0.0000		'F_core'	Refract	0.0310	U	0.0310	U
16		Sphere	Infinity	Infinity	0.0000		'F_core'	TIR	0.0200	O	0.0200	O
17		Y Toroid	-0.0200	Infinity	0.0000	'F_core'	'F_clad'	TIR	0.0142	U	0.2500	U
18		Y Toroid	-0.0200	Infinity	0.0000	'F_core'	'F_clad'	TIR	0.0142	U	0.2500	U
19		Y Toroid	-0.0200	Infinity	0.0000	'F_core'	'F_clad'	TIR	0.0142	U	0.2500	U
20		Y Toroid	-0.0200	Infinity	0.0000	'F_core'	'F_clad'	TIR	0.0142	U	0.2500	U
21		Sphere	Infinity	Infinity	0.0000	'F_core'		TIR	0.0200	O	0.0200	O
22		Sphere	Infinity	Infinity	0.0000		'F_clad'	TIR	0.0280	O	0.0280	O
23		Y Toroid	-0.0280	Infinity					0.0000	O	0.0000	O
24									0.0000	O	0.0000	O
25									0.0000	O	0.0000	O
26									0.0000	O	0.0000	O
27				Infinity	0.0000	'F_clad'		TIR	0.0280	O	0.0280	O
28		Sphere	Infinity	Infinity	0.0000	AIR		Refract	0.0280	O	0.0280	O
29		Sphere	Infinity	Infinity	0.0000			Refract	0.0173	O	0.0173	O
Image		Sphere	Infinity	Infinity	0.0000			Refract	0.0310	U	0.0310	U

End Of Data

Si Patterning: V-Grooves and Waveguide Area

1

Waveguide Area Etching
Photolithography Mask 1

Mask 1 Layout:

Process details:

1) Clean surface (Piranha 10min, DI water)
2) Dehydrate wafer in convection oven at 120°C - 150°C for 30mn minimum
3) Spin-coat PR:
   Shipley 1813, 2um thick
   spin rate of 1950rpm
4) Pre-bake (hot plate):115°C, 1mn
5) Align Mask 1
6) UV expose (50mW/cm2- about 6sec)
7) Develop: AZ 400K, 20°C (1mn)
8) Post-bake: 90°C, 2mn

2

Detailed Photolithography Steps (#3 or #4 Cross-Section Views)

1) Spin-Coat PR and pre-bake

2) Align Mask and UV expose

3) Develop and post-bake

3

Etch Silicon

- **Anisotropic Etch of Silicon**
  (don't want undercut/overcut associated with isotropic etching)
- Needed for subsequent waveguide formation.
- It is extremely important that surface remains smooth after silicon etching so that deposited core and claddings will be deposited uniformly without bending.
- Thickness: T = 57um
  - **DRIE etch silicon**
  - Rate: 4um/mn
  - Time: 17mn
  - Selectivity: Si –1: S1813:1/90 →1.183um of PR etched, 0.8um remains

#3 or 4 Cross-Section Views

4

Remove Photoresist

- Ash remaining PR using Oxygen plasma

#3 or 4 Cross-Section Views

5

Photolithography Mask 2

Mask 2 Layout:

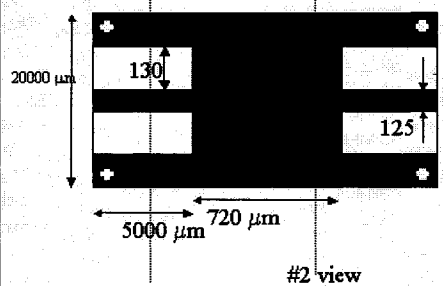

Pattern front side SiO_2:

-Clean surface
-Spin-coat 1.4um thick PR: S1813 (3900rpm)
-Pre-bake: 115°C, 1mn
-Align Mask 2
-UV expose: (200mW/cm2 about 20sec)
-Develop: HPDR 426 (60 sec)
-Post-bake: 90 ° C, 2mns
-Etch SiO_2 using RIE (CHF3: Ar: CF4-1, 30:70:7 sccm; Gauss Magnetic Field=70; RF power=720W at rate of 3900A/min→137sec total)
-Remove PR: ashing (40min)

7

V-grooves Formation

Process details:

- Thin oxide layer (thermal growth)
1) Grow 0.8μm of thermal oxide at 1150 °C on both sides of the wafer:
   – Serves as a mask in subsequent TMAH etch of silicon
2) Pattern front side SiO_2 using standard photolithographic procedures with high exposure dose

6

Detailed Photolithography Steps (#1 Cross-Section Views)

1) a)Deposit thermal oxide
b)Spin-Coat PR and pre-bake

2) Align Mask and UV expose

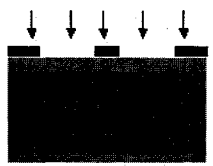

3) Develop and post-bake

4) Etch SiO_2 and remove PR

8

TMAH/H20 Anisotropic (100) Silicon Etching

(#1 Cross-Section Views)

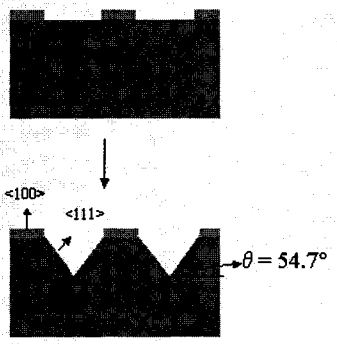

Etch rate ratio
{100}/{111} = 57

Parameters:
-Temperature: 85C
-TMAH Concentration: 25%
-Rate: 28.5um/hr
-Time:3hr20min to etch 93um deep V-groove

9

Silicon Dioxide Removal

Remove remaining oxide using 10:1 HF solution (selective etch that will not etch silicon)
Time: 36min (rate = 235A/min)

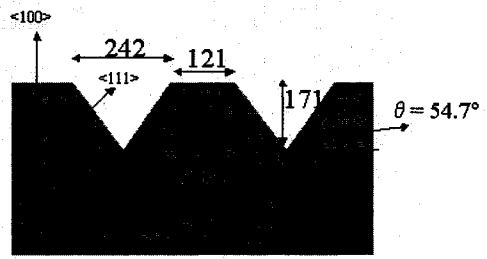

10

Waveguide Fabrication

Now:

Goal:

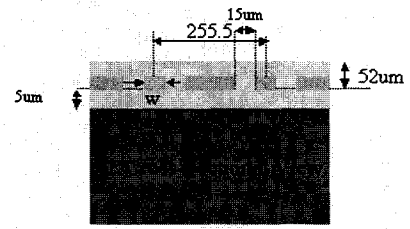

Silicon Substrate with height etched by thickness T = 57um

Core: SU-8
Cladding: PMMA

11

Lower Cladding Deposition

Spin Coating

- clean and dry wafer: solvent and/or O2 plasma clean; piranha; DI rinse
- dispense 5-8ml for 150mm wafer
- spread 500rpm for 5 sec or 0rpm for 10sec
- spin: ramp to final spin speed of 900rpm at acceleration of 300rpm/sec and hold for 60 sec.

Deposition Parameters:

- Deposition rate: 5um thickness at 900rpm spin speed of 950 PMMA A (11% solid PMMA dissolved in anisole)
- Cure with ramp-up recipe (from room temp. to 180C back to room) to avoid cracks in the PMMA deposited layer
- Refractive index: 1.49 at 633nm wavelength
- Thickness Required: 5um
- Total time = 1 day (due to baking recipe to have crack-free structure)

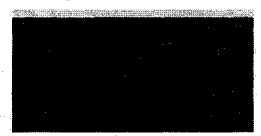

12

Core Deposition

SU-8 spin coating:

-Clean and dry wafer
-Dispense 1ml of SU-8 per inch of substrate diameter (6in diameter = 6ml of SU-8)
-Spread: ramp to 500rpm at 100rpm/sec acceleration and hold this speed for 5-10sec
-Spin: ramp to final speed at an acceleration of 300rpm/sec and hold for total of 30 sec
-For SU-8 25, 47um is achieved at 1300 rpm

Deposition Parameters:

- Ambient: SU-8 25
- Refractive index: 1.596 at 633nm
- Thickness Required: 47um
- Total time: approximately 2mn

13

Core Patterning

-After spin coating, the resist must be soft baked to evaporate the solvent and densify the film
-Bake time stated here is based on contact hot plate process
-For 47um thick layer, prebake first at 65 C for 5mn, and then softbake at 95C for 20mn

14

Photolithography Mask 3

SU-8 is negative resist

Mask 3: Top View

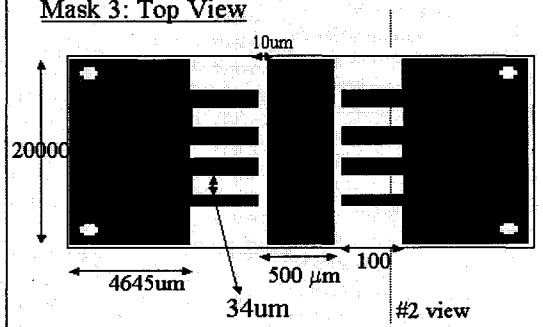

15

Exposure:
-near UV (350-400nm)
-use filter to cut wavelengths below 350nm since these will cause T-toping
-exposure dose for 47um thick layer and crack-free structures, the optimal exposure dose is found to be approximately 800mJ/cm^2
-use 10 to 15 sec exposure intervals with 60 sec. Waiting time in between to alleviate the formation of thin crust and loss of resolution due to heating of the surface induced by high dose and long exposure time.

Post Exposure Bake:
For 47um thick, first bake at 65C for 5mn, and then at 95C for 15min on a hot plate

Photolithography Steps

(SU-8 is –ve PR)

1) Spin-Coat PR and Pre-Bake

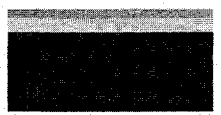

2) Align Mask and UV expose

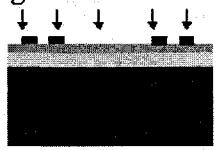

3) Develop and Hard Bake

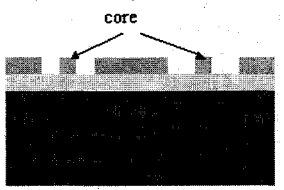

Develop in commercial SU-8 developer, need agitation (time 5), then rinse and spin-dry. (timed etch to avoid cracking and swelling of PMMA lower cladding)

16

Upper Cladding Deposition

Deposit PMMA (same as lower cladding deposition)
Minimum Thickness: 5 um

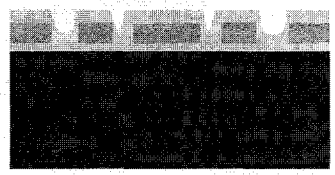

17

Al Deposition (Hard Mask Formation)

Sputter Al:

Parameters:

-Thickness: 2500A
-Target moving speed: 15cm/min
-RF Power: 1.1kW
-Vacuum level: 6E-7
-Temperature: below 88C
-Pressure: 10MTorr

19

Cladding Removal Everywhere Outside Waveguide Area:

Photolithography Mask 4

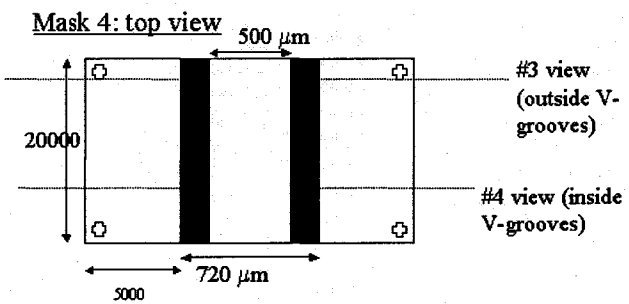

18

Photolithography Steps

(Same conditions as for mask 1— AZ 5214 PR)

1) Spin-Coat PR and Pre-Bake

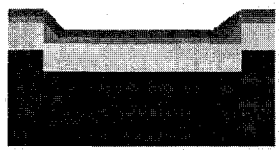

2) Align Mask and UV expose

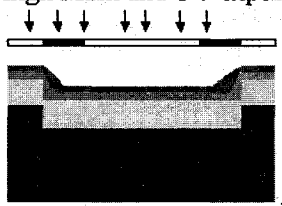

3) Develop and Post Bake

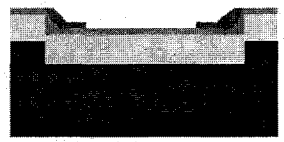

20

Al Removal

PAN Etch AL where unprotected by photoresist:

- Etching chemical: H_3PO_4:DIH_2O:HNO_3:SH_3COOH [16:2:1:1]
- Selectivity: Al:1
- Rate: 40A/sec
- Time: 62sec
- Temperature: 50C

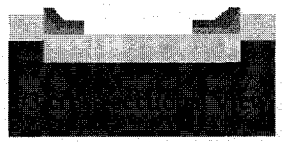

21

Final PDMS Bonding

- Bond PDMS cover for protection and sealing of microchannel using plasma activation or thermal treatment

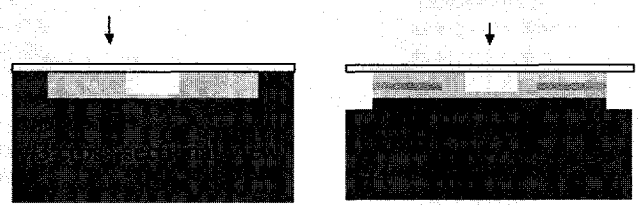

23

Etch Exposed PMMA Cladding Layers (RIE)

RIE etch with following recipe:

-O2 (40sccm)
-Ar (160sccm)
-Power = 200W
-Pressure = 150mTorr

- Etch rate: 0.72um/min =>5um to etch => 7mn
- Temperature: below 88C
- Note, the resist is also etched during this process
- Remove Al mask (PAN Etch)

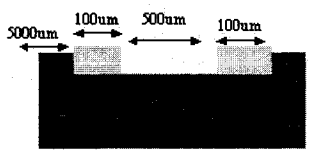

22

Final Device Layout

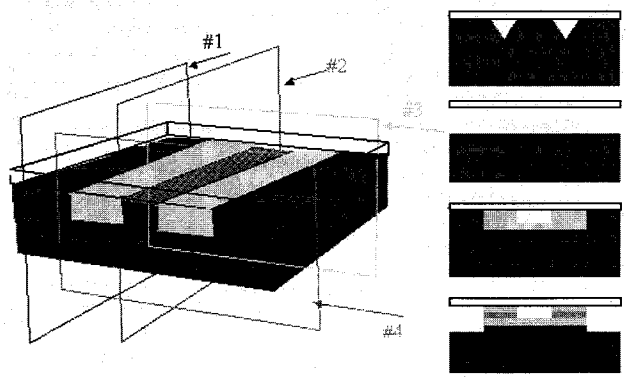

24

Appendix D Mask Layout

D.1 Device 1

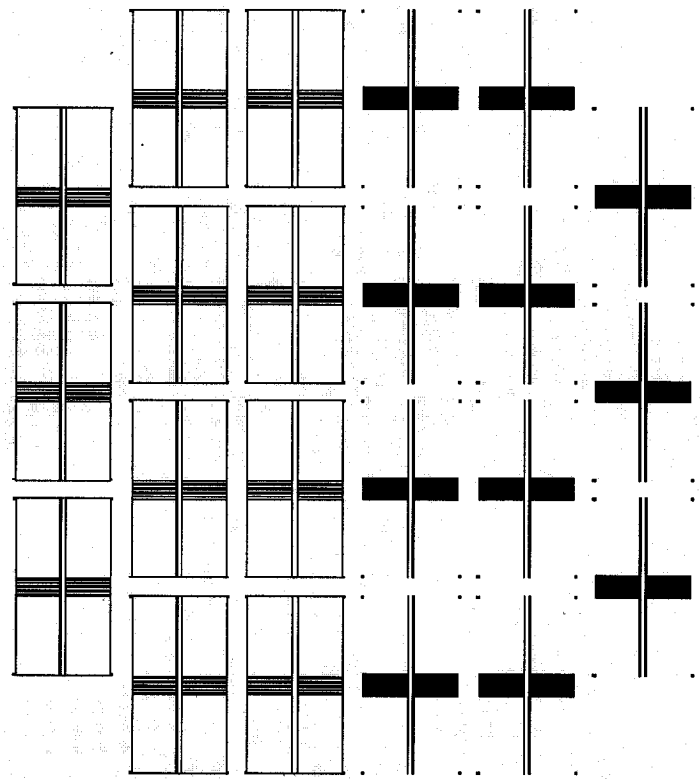

Figure D.1 Device 1 Mask Layout

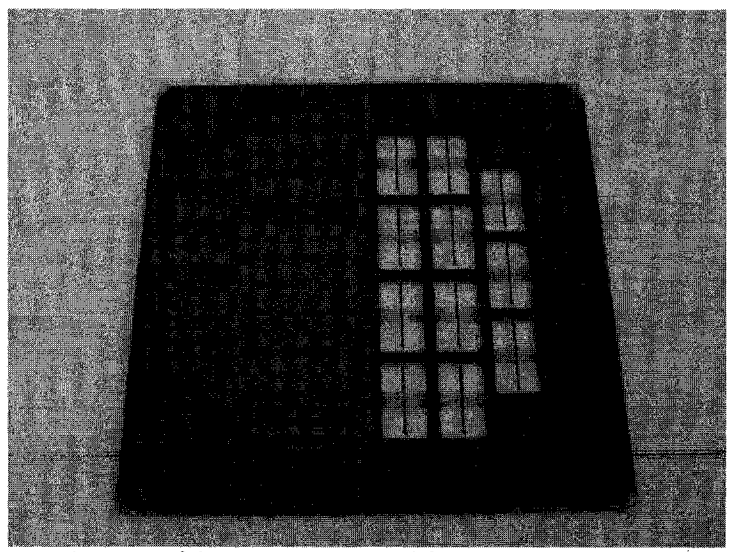

Figure D.2 Image of the arrangement used for "two-on-one" mask exposure

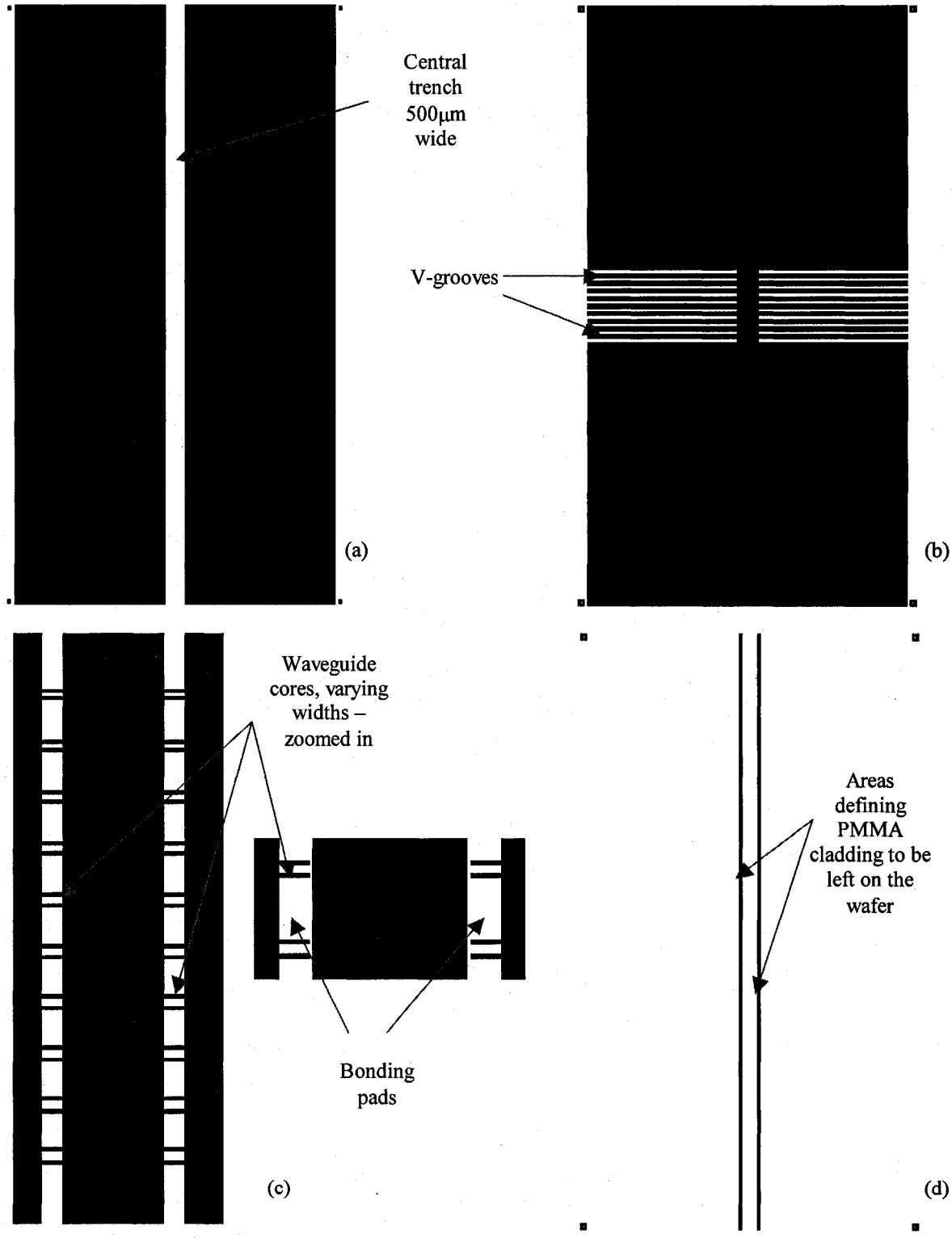

Figure D.3 Individual masks (a) Mask 1-DRIE of Si substrate; (b) Mask 2- V-grooves; (c) Waveguides; (d) Mask 4- PMMA RIE

D.2 Device 2

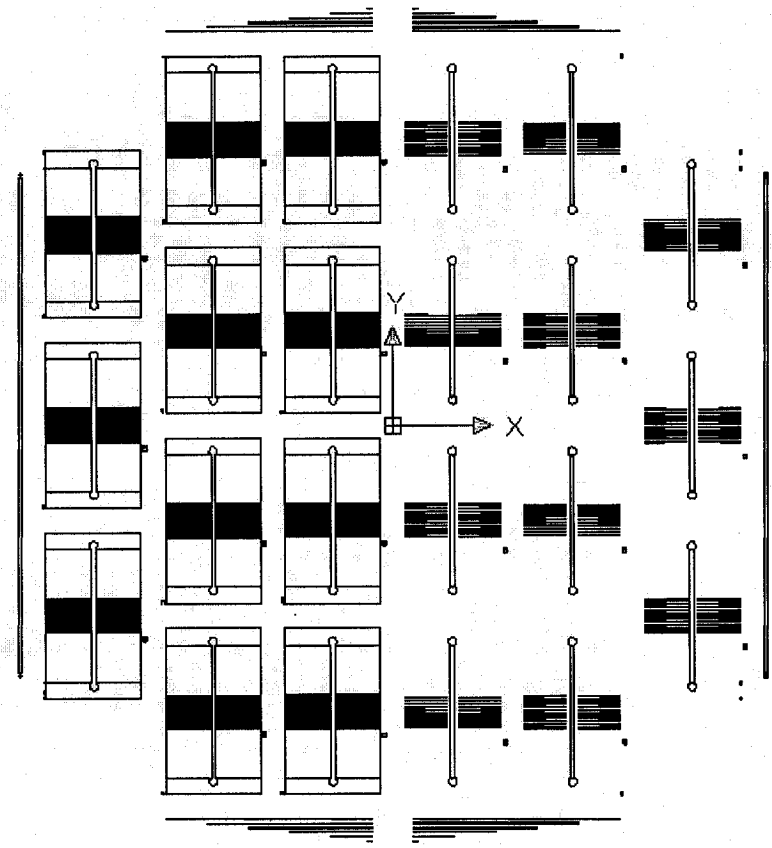

Figure D.4 Device 2 Mask Layout

Appendix E Device 2 BPM Simulations

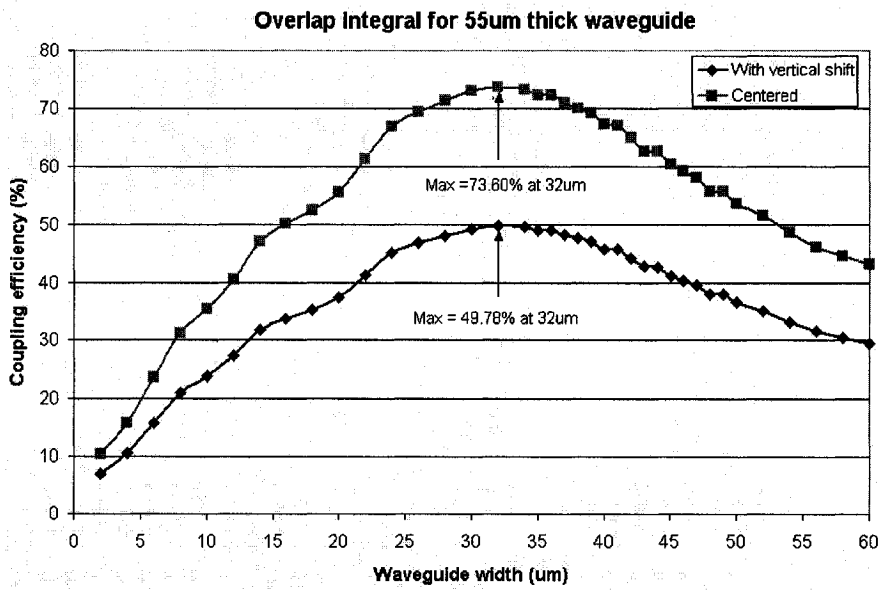

Figure E.1 Coupling efficiency vs. waveguide core width for 55μm core thickness

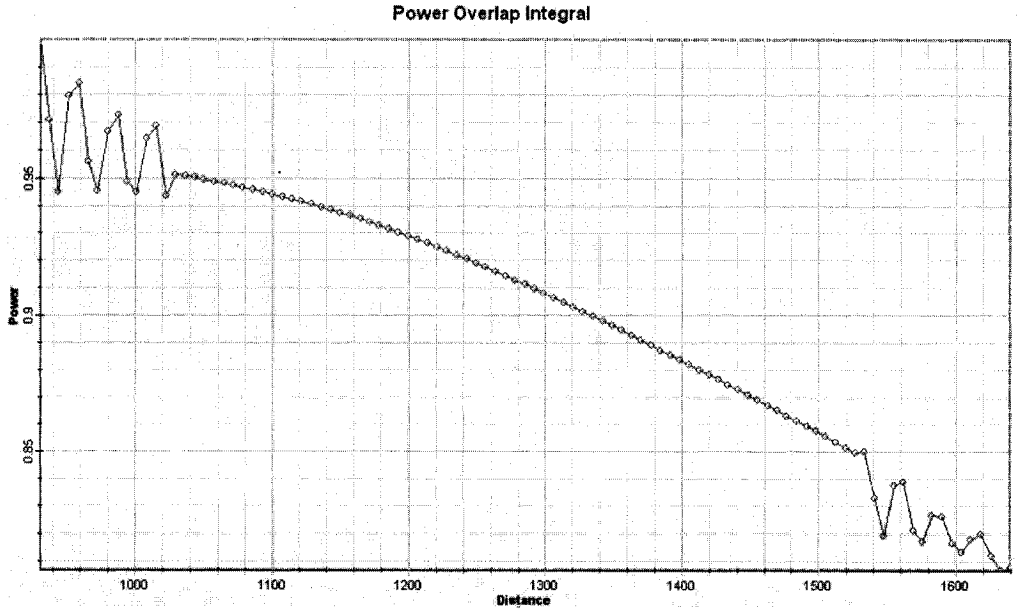

Figure E.2 Power overlap integral